CHALMERS

Ringhals Diagnostics and Monitoring, Annual Research Report 2018-19

I. PÁZSIT
L.A. TORRES
C. MONTALVO
Y. KITAMURA
L. NAGY
H. NYLÉN

Nuclear Engineering Group
Division of Subatomic and Plasma Physics
CHALMERS UNIVERSITY OF TECHNOLOGY
Gothenburg, Sweden, 2019
CTH-NT-339/RR-22 June 2019

CTH-NT-339/RR-22 June 2019

Ringhals Diagnostics and Monitoring, Annual Research Report 2018-2019

I. Pázsit, L. A. Torres, C. Montalvo, Y. Kitamura, L. Nagy and H. Nylén

Nuclear Engineering Group
Division of Subatomic and Plasma Physics
Chalmers University of Technology
SE-412 96 Göteborg, Sweden
ISSN 0281-9775

Ringhals Diagnostics and Monitoring, Annual Research Report 2018-2019

I. Pázsit, L. A. Torres, C. Montalvo, Y. Kitamura, L. Nagy and H. Nylén

Nuclear Engineering Group
Division of Subatomic and Plasma Physics
Chalmers University of Technology
SE-412 96 Göteborg, Sweden

Abstract

This report gives an account of the work performed by the Division of Subatomic and Plasma Physics (formerly, Division of Nuclear Engineering), Chalmers, in the frame of a research collaboration with Ringhals, Vattenfall AB, contract No. 677353-003. The contract constitutes a 1-year co-operative research work concerning diagnostics and monitoring of the BWR and PWR units. The work in the contract has been performed between 1 July 2018 – 30 June 2019. During this period, we have worked with five main items as follows:

1. Investigation of possible baffle jetting in R3 with noise analysis of in-core and ex-core detector signals;
2. Analysis of the vibrations of thimble tubes with axially dependent in-core measurements in various radial positions;
3. Evaluation of new ex-core measurements for beam mode and tilting mode vibrations in R3 or R4;
4. Development of a method to use the Eigenvalue Separation in noise analysis for characterising of regional power oscillations and understanding the role of loosely coupled cores in the development of regional instabilities;
5. Further investigations of the possibilities of using fission chamber signals for measurement of subcritical reactivity, such as elaboration of the equivalent of the Feynman-alpha method of pulse counting, and accounting for delayed neutrons.

The work was performed at the Division of Subatomic and Plasma Physics, Chalmers University of Technology by Imre Pázsit (project co-ordinator), Luis Alejandro Torres (visitor from UPM, Madrid, Spain), Cristina Montalvo (research collaborator from UPM), Yasunori Kitamura (research collaborator from KURNS, Kyoto, Japan), Lajos Nagy (double degree PhD student) and Henrik Nylén, the contact person at Ringhals.

CONTENTS

1. INTRODUCTION

This report gives an account of the work performed by the Nuclear Engineering Group of the Division of Subatomic and Plasma Physics (former Division of Nuclear Engineering), Chalmers, in the frame of a research collaboration with Ringhals, Vattenfall AB, contract No. 677353-003. The contract constitutes a 1-year co-operative research work concerning diagnostics and monitoring of the BWR and PWR units. The work in the contract has been performed between July 1st 2018, and June 30th, 2019. During this period, we have worked with five main items as follows:

1. Investigation of possible baffle jetting in R3 with noise analysis of in-core and ex-core detector signals;

2. Analysis of the vibrations of thimble tubes with axially dependent in-core measurements in various radial positions;

3. Evaluation of new ex-core measurements for beam mode and tilting mode vibrations in R3 or R4;

4. Development of a method to use the Eigenvalue Separation in noise analysis for characterising of regional power oscillations and understanding the role of loosely coupled cores in the development of regional instabilities;

5. Further investigations of the possibilities of using fission chamber signals for measurement of subcritical reactivity, such as elaboration of the equivalent of the Feynman-alpha method of pulse counting, and accounting for delayed neutrons.

This work was performed at the Division of Subatomic and Plasma Physics, Chalmers University of Technology by Imre Pázsit (project co-ordinator), Luis Alejandro Torres (visitor from U), Cristina Montalvo (research collaborator from UPM), Yasunori Kitamura (research collaborator from KURNS), Lajos Nagy (double degree PhD student) and Henrik Nylén, the contact person at Ringhals.

2. INVESTIGATION OF POSSIBLE BAFFLE JETTING IN R3 WITH NOISE ANALYSIS OF IN-CORE AND EX-CORE DETECTOR SIGNALS

This is a newly initiated item in the project, which has not been dealt with before. Its objective is to identify and elaborate suitable methods for detection of incipient baffle jetting, and its localisation inside the core, as well as to monitor its development once its presence is identified.

The background of the origin of this subject is that a so-called upflow conversion is planned on R3, in order to minimise the risk for fuel damage from baffle jetting. At present the coolant flow outside the baffle plates is oriented downwards in R3, whereas it is upwards in R2 and R4. The general problem is the pressure difference between the outer side of the baffle plates and the core, in particular at the higher axial elevations. The bolts fixing the baffle structure are exposed to wear during longer times (due to thermal fatigue and fast neutron irradiation), which process can degrade the bolts, such that a gap can open at the inside corners of the baffle. Due to the pressure difference, jet streams can arise towards the interior of the core, which can lead to very strong vibrations of the individual fuel pins or the assemblies. Such a phenomenon can appear quite suddenly during the cycle. If it goes undetected, it can lead to serious damage of the fuel pins, including breakdown of the cladding.

Experience at other plants suggests that baffle jetting can be detected by neutron noise measurements [1, 2, 3]. The primary means of detection is using in-core detectors. Since baffle jetting occurs only in peripheral fuel assemblies, the in-core measurements have to be made close to the core edge. Previous experience shows [2] that if in-core measurements are made in several peripheral positions, then a comparison of the power spectra (APSDs) between the detectors can reveal extra peaks in some of the spectra, which are a clear indicator of the presence of baffle jetting. A further indicator of baffle jetting is when several higher harmonics can be seen in the in-core spectra.

Ex-core detectors yield more implicit information on fuel pin vibrations induced by baffle jetting. One possibility is to use the correlations between in-core detectors and ex-core detectors nearby. Pure ex-core measurements are used for trend analysis and to identify quadrants of the core where baffle jetting occurs, after which dedicated in-core measurements can be performed to locate the actual area of the core exposed to baffle jetting. An indicator of baffle jetting could be when the characteristics of the shell-mode vibrations change, since these are an indication of the changes in the structural mechanics properties of the baffles.

No dedicated in-core measurements were performed in the current Stage to this end. Some in-core measurements were performed earlier, in Stages 12 and 13 [4, 5], but in those measurements, the five in-core detectors were aligned along a radius of the core (see Fig. 3.1 in the next Section). That is, only one in-core detector was placed at the core boundary, hence no possibility exists for comparing the APSDs

of in-core detectors in several peripheral positions. For this reason, it was decided that in this report, only the latest ex-core measurements (i.e. those taken in this Stage) will be analysed.

From the point of view of ex-core neutron noise, baffle jetting can possibly be identified from the deformations it incurs in the core-barrel structure, and therefore its effect on the ex-core neutron noise. From the mechanical nature of the problem, baffle jetting is expected to lead to shell-type vibration modes, but also to a uniform radial increase of the core size, i.e. core widening (zeroth asymuthal mode). Such a phenomenon is known from the Phenix Sodium Fast Reactor measurements [6]; and it was termed "core flowering". From the symmetry properties of the core widening, it is clear that its presence in the detector signals can be enhanced with the addition of all four detector signals at the same axial level, which is the same as the enhancement of the reactivity term. However, the frequency of the core widening effect is expected to be different from that of the reactivity effect, induced by the individual vibrations of the fuel assemblies at 8 Hz; rather, it should lie closer to the shell mode vibrations.

In addition, due to the thermal hydraulics conditions, such deformations are expected to lead to larger changes at the upper part of the core than at the lower part). Hence the effect of baffle jetting would be consistent with the amplitude of the peak corresponding to the core widening effect, as well as to that of the shell mode, was larger in the upper detectors than in the lower detectors.

To this end, the shell mode components and the reactivity components were compared between the upper and lower detectors for all three measurements. Figs. 2.1, 2.2 and 2.3 show the shell mode components for the three measurements. The shell mode is represented by the peak at 20 Hz. It is seen that in all three measurements the peak at 20 Hz is larger for the upper detectors than for the lower detectors. This is in clear contrast to the amplitudes of the beam-mode vibrations around 8 Hz, where, for obvious reasons, the amplitudes of the peaks are larger in the lower detectors than in the upper ones. The reversed relationship for the shell mode vibrations could be an implicit indication of baffle jetting.

Figs 2.4, 2.5 and 2.6. show the comparison for the reactivity component between the upper and lower detector for the three measurements. It is seen that, in addition to the peak at 8 Hz, there is also a peak at around 15.5 - 15.6 Hz. A similar peak was identified in the previous stage in the R4 ex-core spectra at 16 Hz, which was interpreted as the first harmonic of the 8 Hz fuel assembly vibrations. However, based on the discussions above, it is conceivable that this peak rather corresponds to the core widening. This assumption is corroborated by the fact that the amplitude of the peaks in all three measurements is higher in the upper detectors than in the lower detectors. This amplifies the assumption that this peak is related to the core widening effect, and it is in agreement with the observations for the shell mode vibrations.

In summary, by identifying the reactivity-like component at 15.5 Hz as the core widening component, it is found that both the shell mode component, as well as the

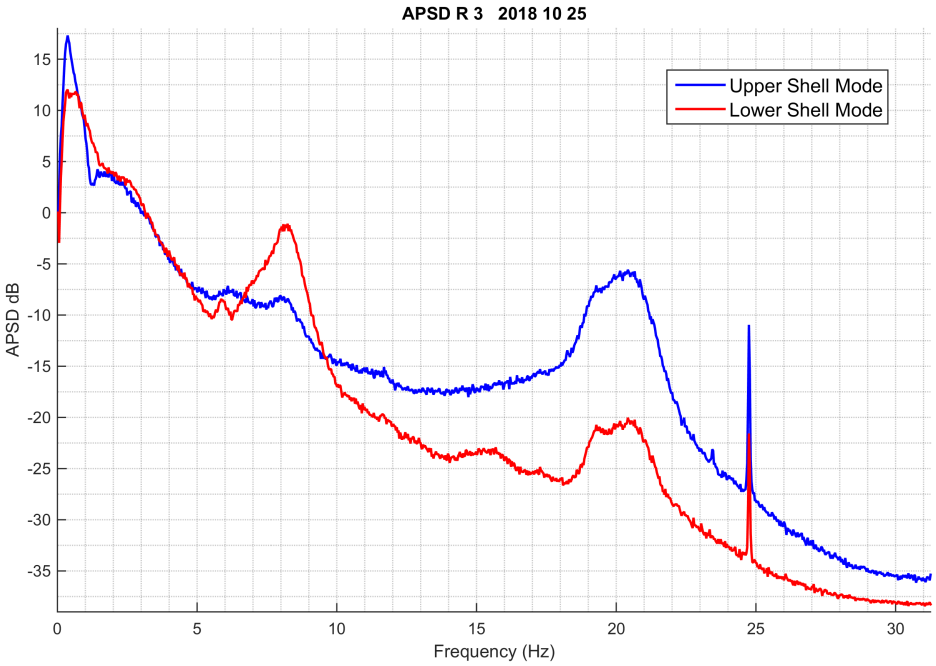

Figure 2.1: APSDs of the shell mode in Measurement 1.

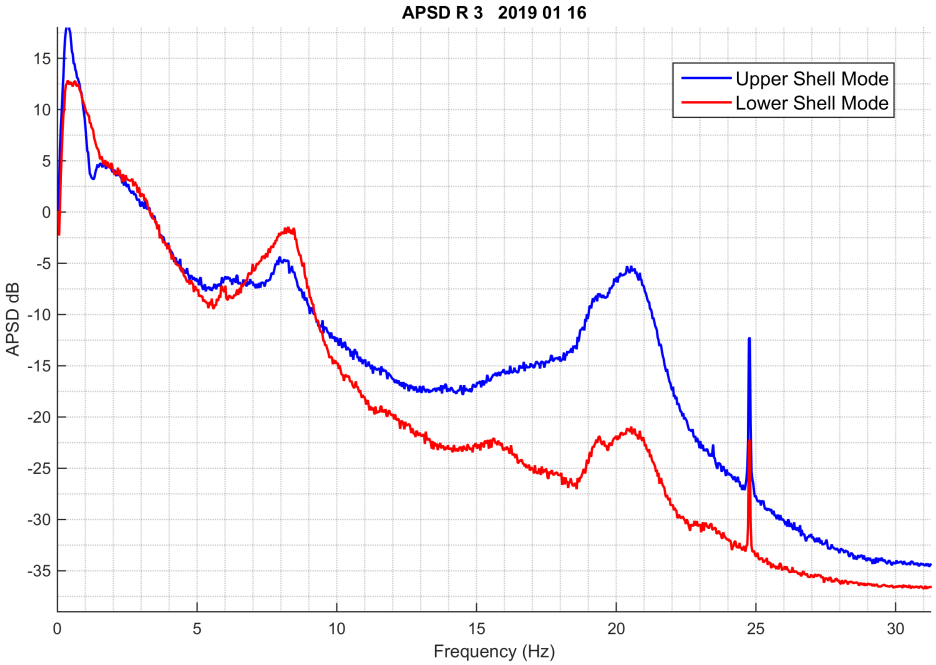

Figure 2.2: APSDs of the shell mode in Measurement 2.

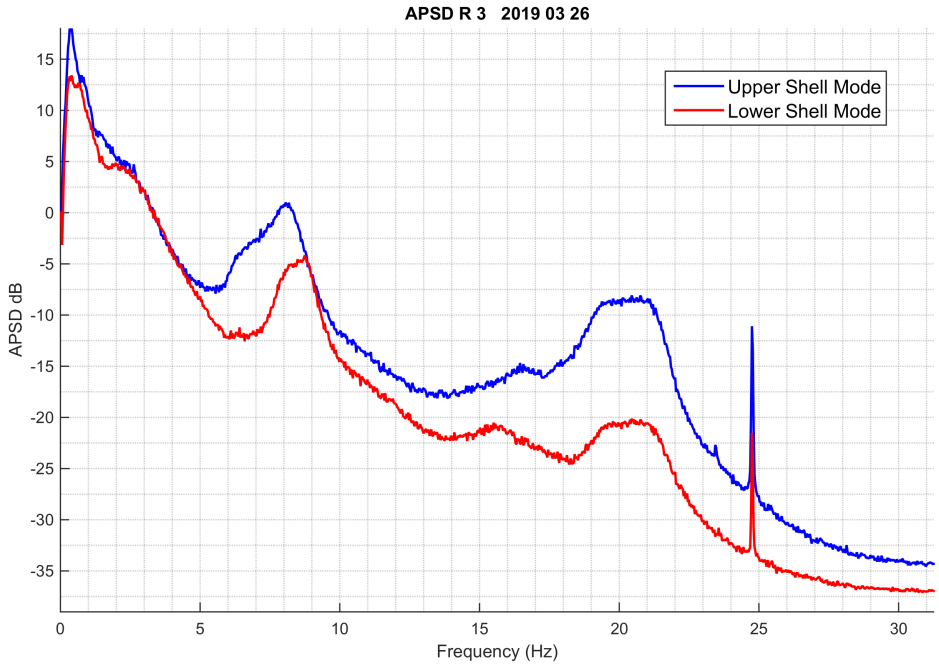

Figure 2.3: APSDs of the shell mode in Measurement 3.

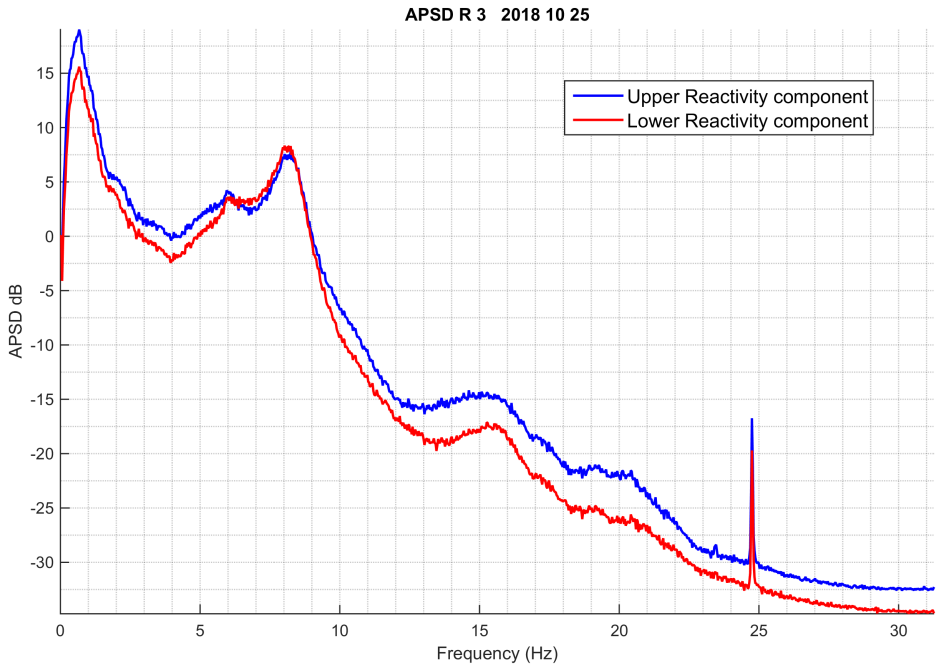

Figure 2.4: APSDs of the reactivity component in Measurement 1.

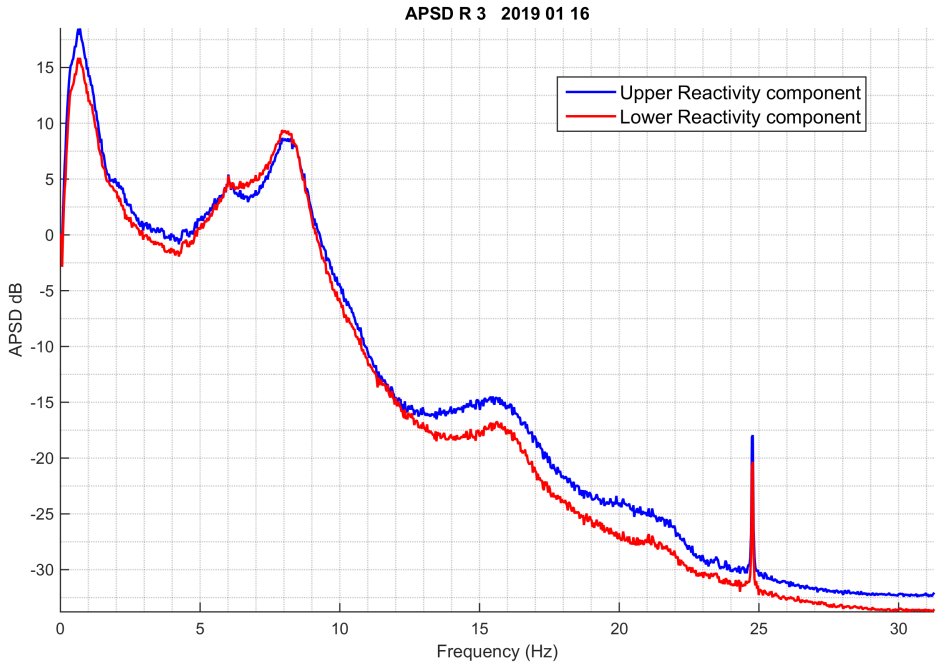

Figure 2.5: APSDs of the reactivity component in Measurement 2.

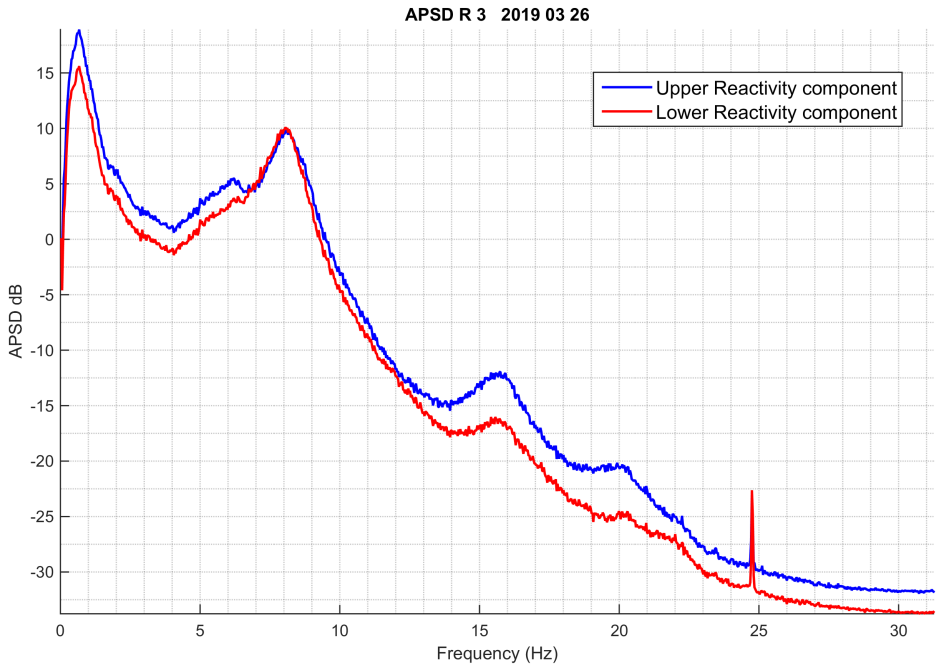

Figure 2.6: APSDs of the reactivity component in Measurement 3.

core widening component, exhibit a larger amplitude peak for the upper detectors than for the lower detectors. This might indicate the presence of baffle jetting. However, because of the sparse azimuthal placing of the ex-core detectors, as well as the global character of the ex-core signals, it is not possible to identify the position(s) of possible baffle jetting with a resolution with respect to the azimuthal position. Moreover, the statement on the possible presence of baffle jetting is based only on a qualitative comparison of the peaks, and similarly to the case of beam mode vibrations, it does not give an indication of the amplitude of the corresponding vibrations, and hence also it cannot be used for the indication of the severity of the vibrations. However, no indications of baffle jetting, such as wear marks on fuel rods at spacer grid positions, could be identified during aimed inspections of fuel assemblies at Ringhals 3 during the outages in 2018 and 2019. On the other hand, similarly to the beam mode vibrations, the relative component amplitude can be used for a trend analysis. To this end, the curve fitting procedure has to be applied to quantify the relative amplitude of the 15.5 and 20 Hz peaks, which requires some further development work. Also, to be able to detect the presence of fuel rod vibrations from baffle jetting, more elaborated methods for spectral examinations are probably needed. This will be done in the next Stages of the project.

3. ANALYSIS OF THE VIBRATIONS OF THIMBLE TUBES WITH AXIALLY DEPENDENT IN-CORE MEASUREMENTS IN VARIOUS RADIAL POSITIONS

It is known that the thimble tubes for in-core detectors, which are led into the instrument guide tubes of the fuel assemblies, are exposed to turbulent pressure fluctuations below and between the lower core plate and the bottom of the fuel assembly. These pressure fluctuations induce vibrations of the thimble tubes, and even in the in-core detectors themselves. Excessive vibrations can damage both the thimble tubes and the instruments guide tubes. The characteristics of these vibrations is very varied, as they are functions of a number of different factors, such as the fuel assembly type, the contact surface between the fuel assembly bottom nozzle and the thimble tubes, and not the least the radial position in the core. In adverse circumstances the vibrations can lead to a serious wear and damage of both the thimble tubes and the instrument guide tubes.

The analysis of the thimble tube vibrations is based on the in-core measurements. Similarly to the subject of baffle jetting, this area of investigations is new in this collaboration project, and there are no clear guidelines, or prior experience, on how the analysis should be performed. This area has to be developed partly with a trial and error method during several forthcoming Stages of the project, by also taking into account the very sparse reports on the phenomenon in the literature [7, 8].

In some of the earlier stages, such as Stages 12 and 13 [4, 5], in-core measurements were performed in five radial positions simultaneously, at six different axial positions. The purpose was to identify the vibrating modes of the individual fuel assemblies, and also to assist the analysis of the ex-core measurements for the diagnostics of shell mode vibrations. It was assumed that the individual peaks in the in-core detector signals were due to the vibrations corresponding to the various bending modes of the fuel assemblies. In the analysis of those measurements so far, only the APDSs of the individual detectors were investigated.

Our previous in-core measurements, made for the diagnostics of core-barrel and fuel assembly vibrations, showed that the in-core detector spectra exhibited a large number of peaks, more than that of the ex-core detectors. The characteristics of the peaks depended on the radial position, and also on the axial position of the detectors (measurements were made in six axial in-core positions in each radial position). These measurements were only analysed from the point of view of fuel assembly vibrations so far, but it is obvious that the information content in these measurements is much larger than what is relevant for core-barrel and fuel assembly vibrations. Most likely, the variety of the peaks and their dependence on the axial position of the detectors, could also have been affected by thimble tube vibrations.

From the diagnostic point of view, detection of thimble tube vibrations is a very difficult task, for several reasons. One is that if a thimble tube is vibrating, it should generate a noise analogue to that of the noise of a vibrating control rod or

fuel assembly. This could be detected by the fact that two detectors, at opposite sides of the vibrating thimble tube, would have opposite phase. However, due to its smaller size and small absorption cross section, the induced neutron noise would be rather small. In addition, one cannot be sure if it is indeed a thimble tube, or a fuel/control rod assembly which vibrates between the two detectors. Moreover, the above facts are only valid if only one thimble tube vibrates between the two detectors, which cannot be taken as granted.

The other reason is that since the effect of such vibrations can only be detected by movable in-core detectors, it may happen that one or several detectors are inserted in vibrating thimble tubes. For such detectors, the noise due to the vibration of the detector itself would dominate over the noise, induced by the possible vibrations of other thimble tubes (with or without a detector).

It is thus seen that the problem to be solved contains a number of unknowns parameters, with only a few measured data, hence it is substantiatlly underdetermined. The only way of having some insight is to progress in a heuristic trial-and-error manner. In the present Stage hence we only investigate one possible scenario, namely if no vibration of the detectors occur, only that of the thimble tubes without a detector.

In the case of the thimble tube vibrations, the task is to determine whether or not such vibrations occur, whereas the frequency of such possible vibrations is not known. The axial dependence of the amplitude of the possible thimble tube vibrations is not known either. Hence we decided to study the phase and coherence between detectors at different radial, but identical axial positions. The hypothesis was, based on our knowledge about the space dependence of the amplitude and the phase of vibration induced neutron noise, that opposite phase between two detectors at different radial positions might be an indication of the presence of a vibrating thimble tube between the two detectors. For such cases, the frequency where the out of phase behaviour occurs could indicate the frequency of the vibrations.

3.1 The layout of the measurements

Since no new in-core measurements were performed during the present Stage, measurements taken in 2008 in R4 were used for the analysis. The layout of the measurement, i.e. the radial and axial positions are shown in Fig. 3.1. The radial measurement positions are labeled from A to E. The measuremens for all five moveable detectors were made in one sequence for the six axial positions, without interrupting the data logging. The change of the axial position of the detectors, and hence the end of a measurement in a given axial position, is indicated by the spike in the signal time series, as is seen in the middle figure, and the different sections of the measurement had to be separated manually.

3.2 Results of the analysis

Since 5 detectors can be paired in 10 different ways, the results are shown below such that several configuations are grouped together, for a more condensed repre-

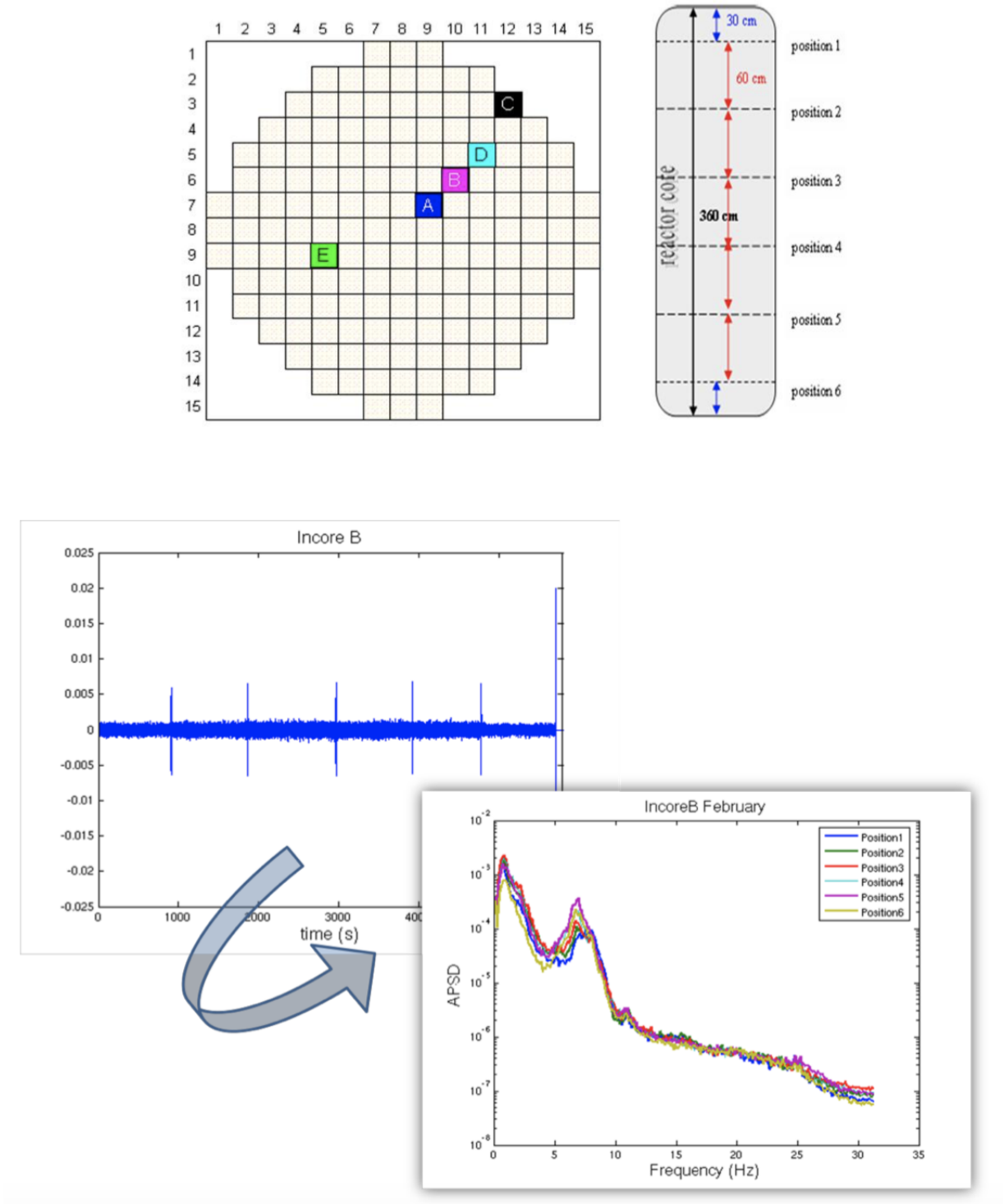

Figure 3.1: Layout of the measuremeent

sentation. In Figs 3.2 and 3.3 the coherence and phase between the pairs A-B, A-C and A-D are shown for all six positions; in Figs 3.4 and 3.5 the pairs B-D, B-C and C-D, are shown, and finally on Figs 3.6 and 3.7 the pairs A-E, B-E, C-E and D-E are shown.

It is seen in Figs. 3.2 - 3.5, that for the four detectors in the upper right hand side of the core horizontal cross-section, i.e. detectors A - D, there is no out of phase behaviour. The phase is zero practically everywhere, and the coherence is relatively high only in the low frequency region. On the other hand, there is an out-of-phase behaviour between detector E, lying on the lower left part of the core, and all other detectors, except A, in the low frequency region. At the same time, the coherence is rather low over the domain of out-of-phase behaviour. There is another, less pronounced frequency domain for the out-of-phase behaviour around 15 - 25 Hz, especially in the lower three axial positions.

3.3 Summary

From the above one could draw the conclusion that there might be a vibrating component somewhere in the core between detector E and the other detectors and in this case it could possibly be a thimble tube. The frequency of these hypothetical vibrations is between 2 - 6 Hz, which is the same range as the vibration frequency of detector tubes in BWRs. Another, significantly less pronounced possibility is that such vibrations occur and possibly around 20 Hz. On the other hand, the fact that detector A does not show the out-of-phase behaviour with E whereas all other detector do show it, could indicate that the thimble tube containing detector A itself is vibrating.

However, these are all rather indirect and highly uncertain conclusions. Further investigations are necessary to understand the possibility of using in-core noise measurements for the detection of such vibrations, and to use them to diagnose the vibrations. For the verification of the method and the conclusions drawn, feedback from the inspections is useful. However, since the measurements analysed here were made in 2008, no such feedback from inspections is possible at this time.

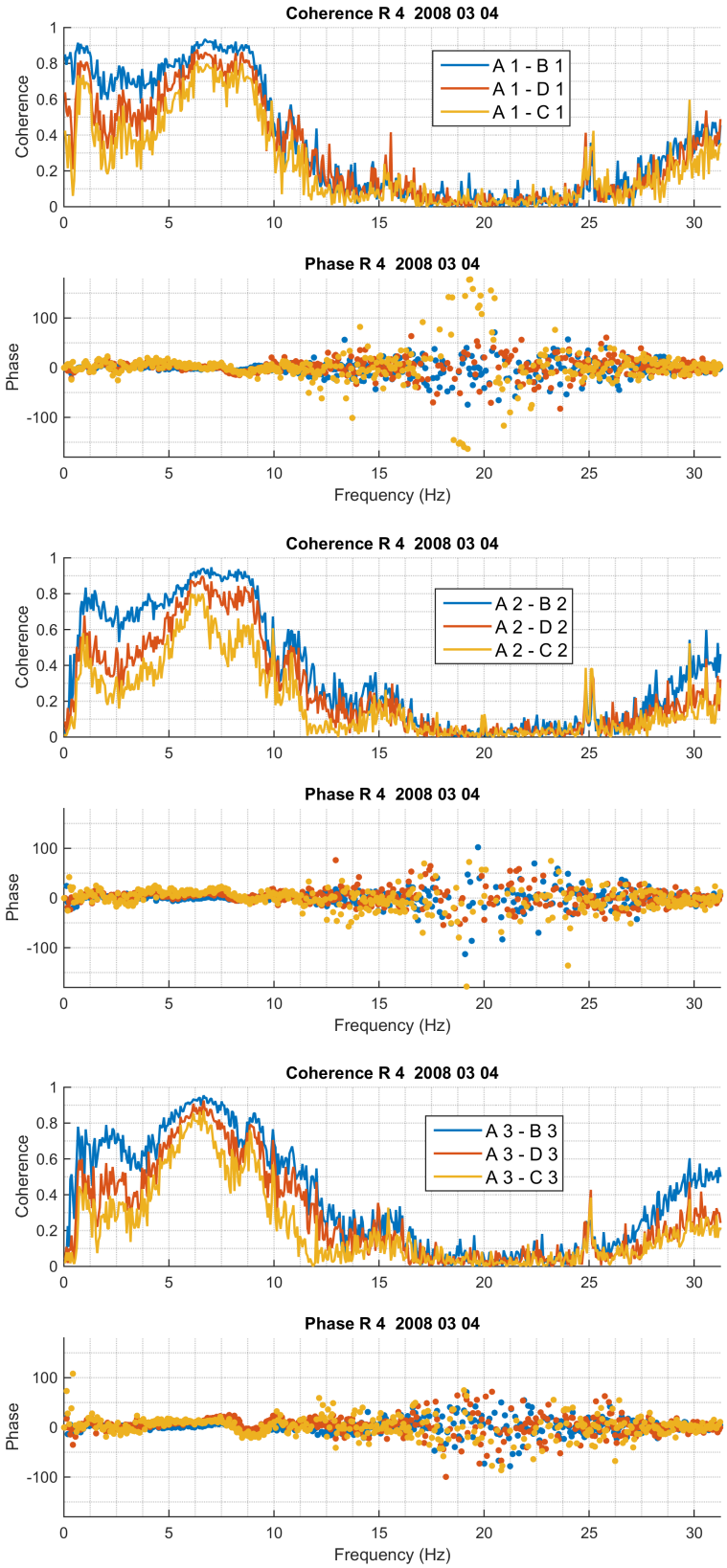

Figure 3.2: Coherence and phase between the pairs A-B, A-C and A-D for the three upper axial positions.

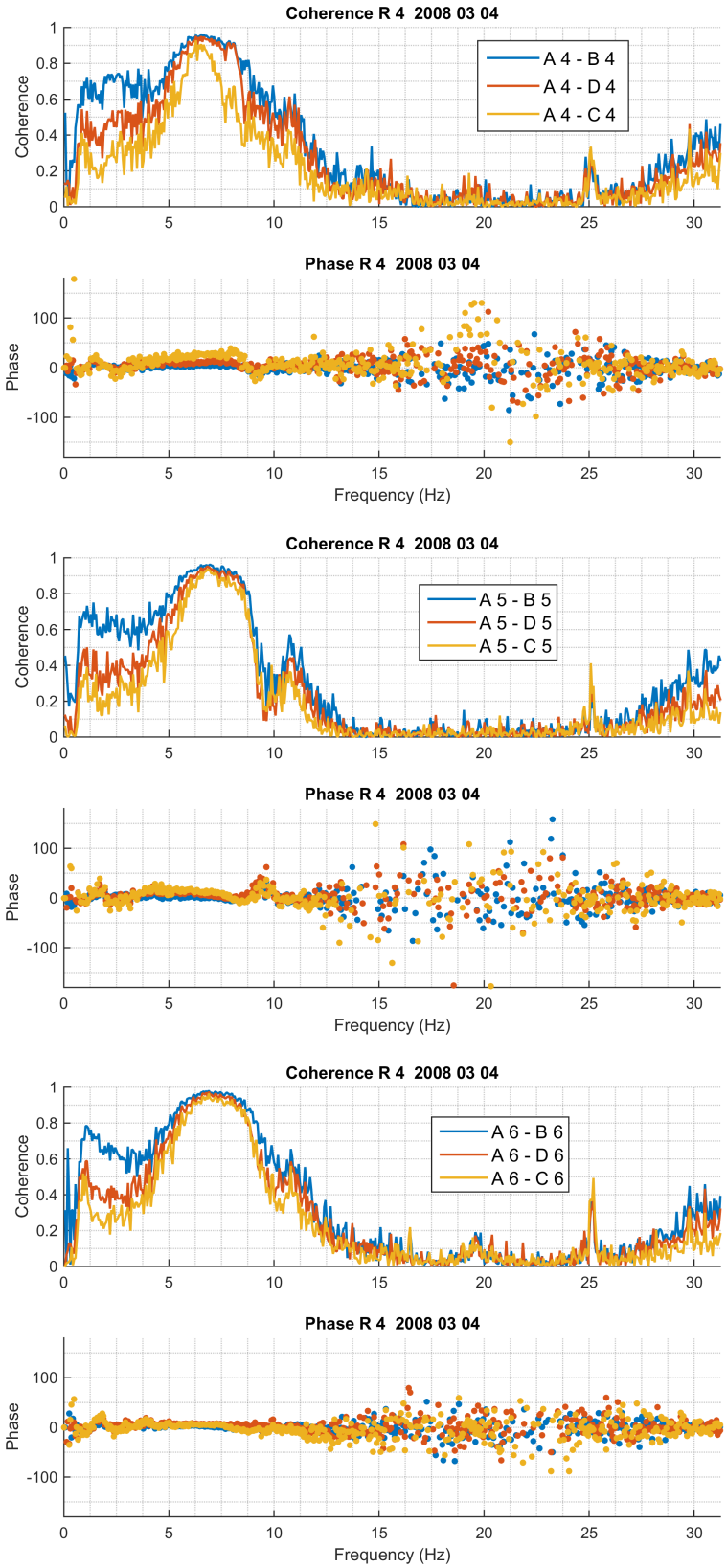

Figure 3.3: Coherence and phase between the pairs A-B, A-C and A-D for the three lower axial positions.

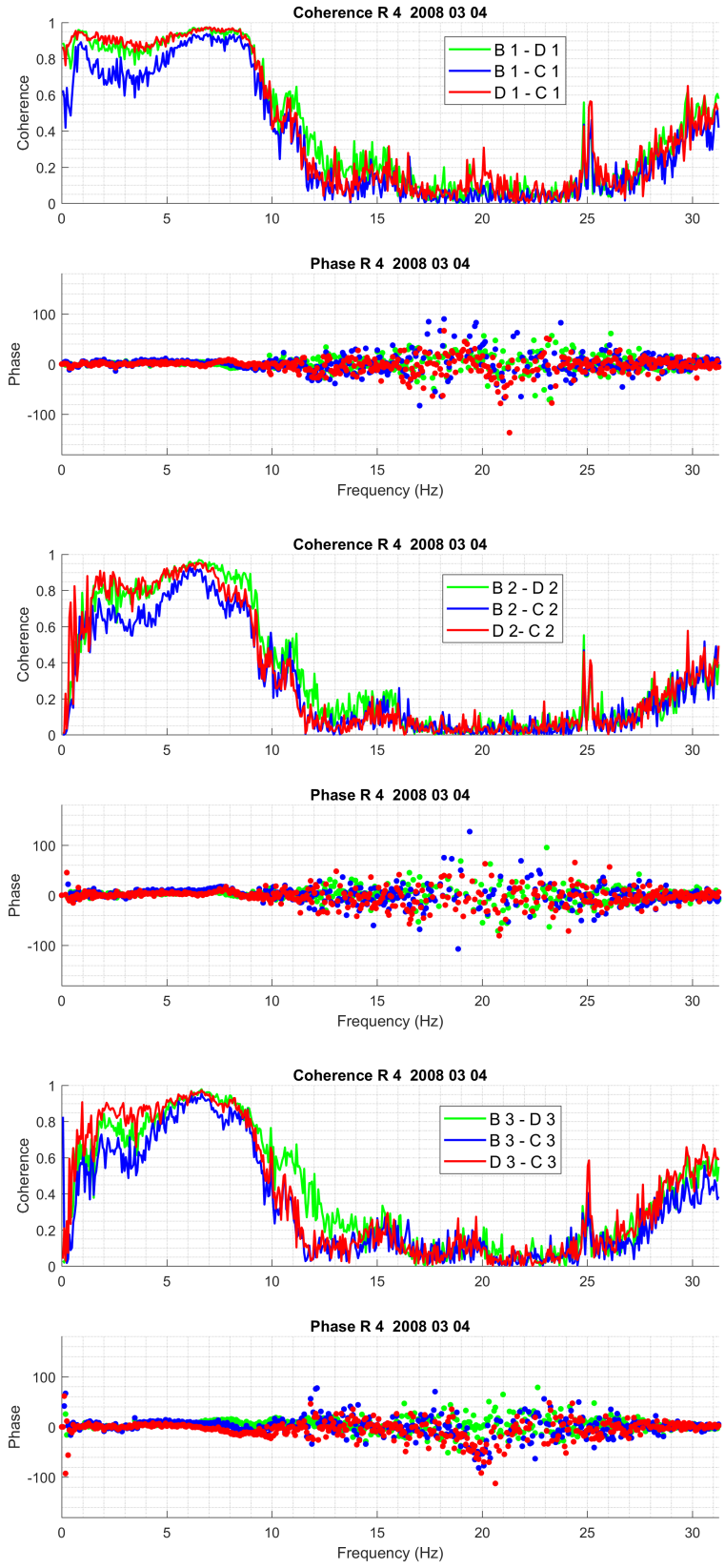

Figure 3.4: Coherence and phase between the pairs B-D, B-C and C-D for the three upper axial positions.

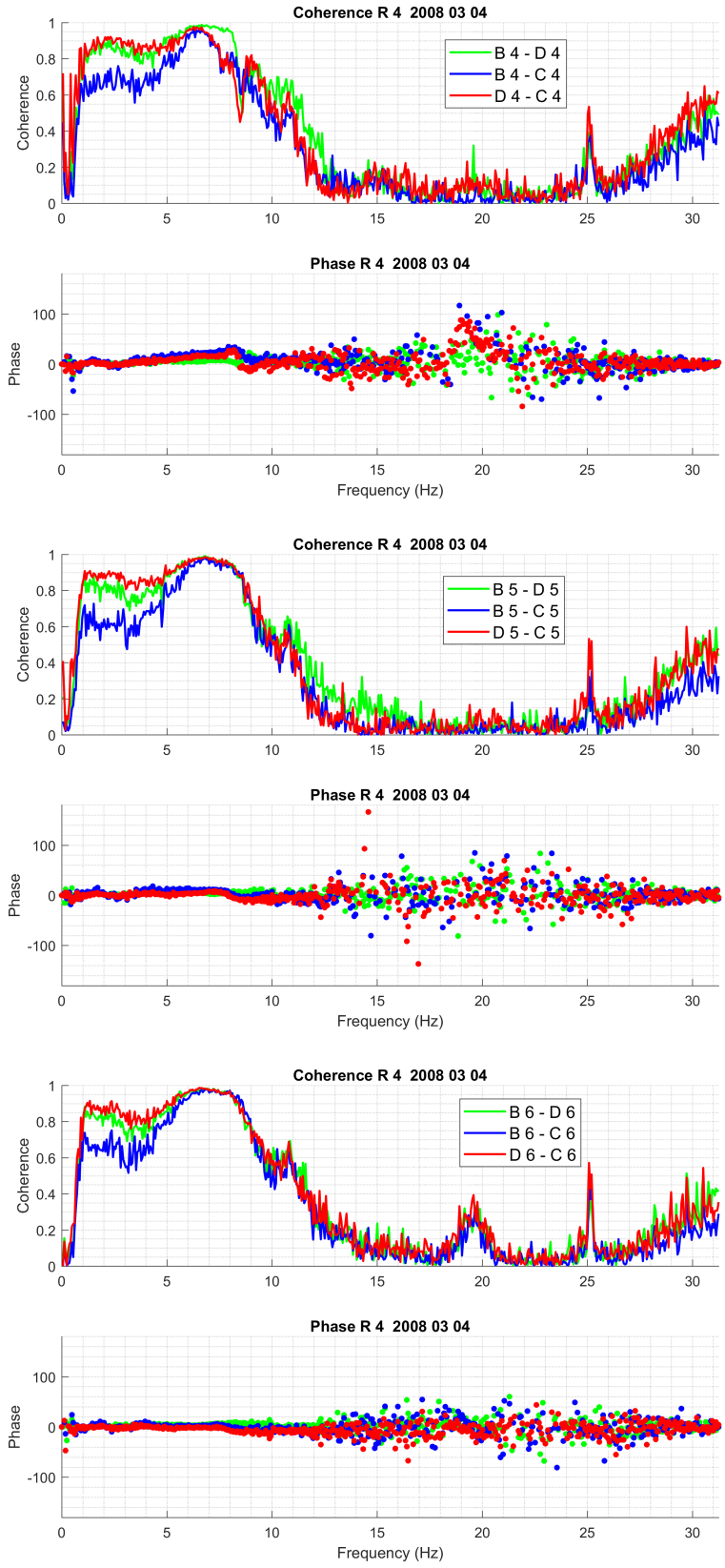

Figure 3.5: Coherence and phase between the pairs B-D, B-C and C-D for the three lower axial positions.

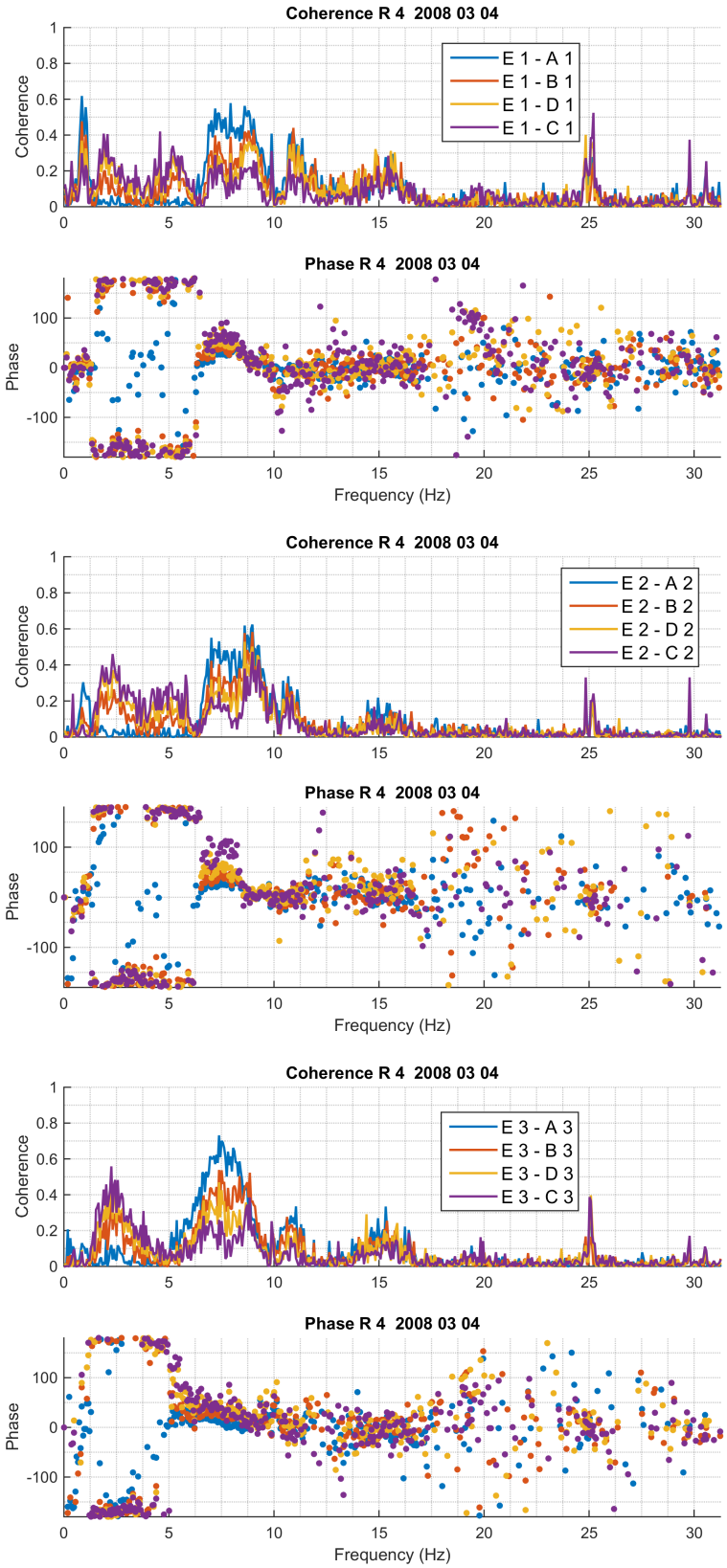

Figure 3.6: Coherence and phase between the pairs A-E, B-E, C-E and D-E for the three upper axial positions.

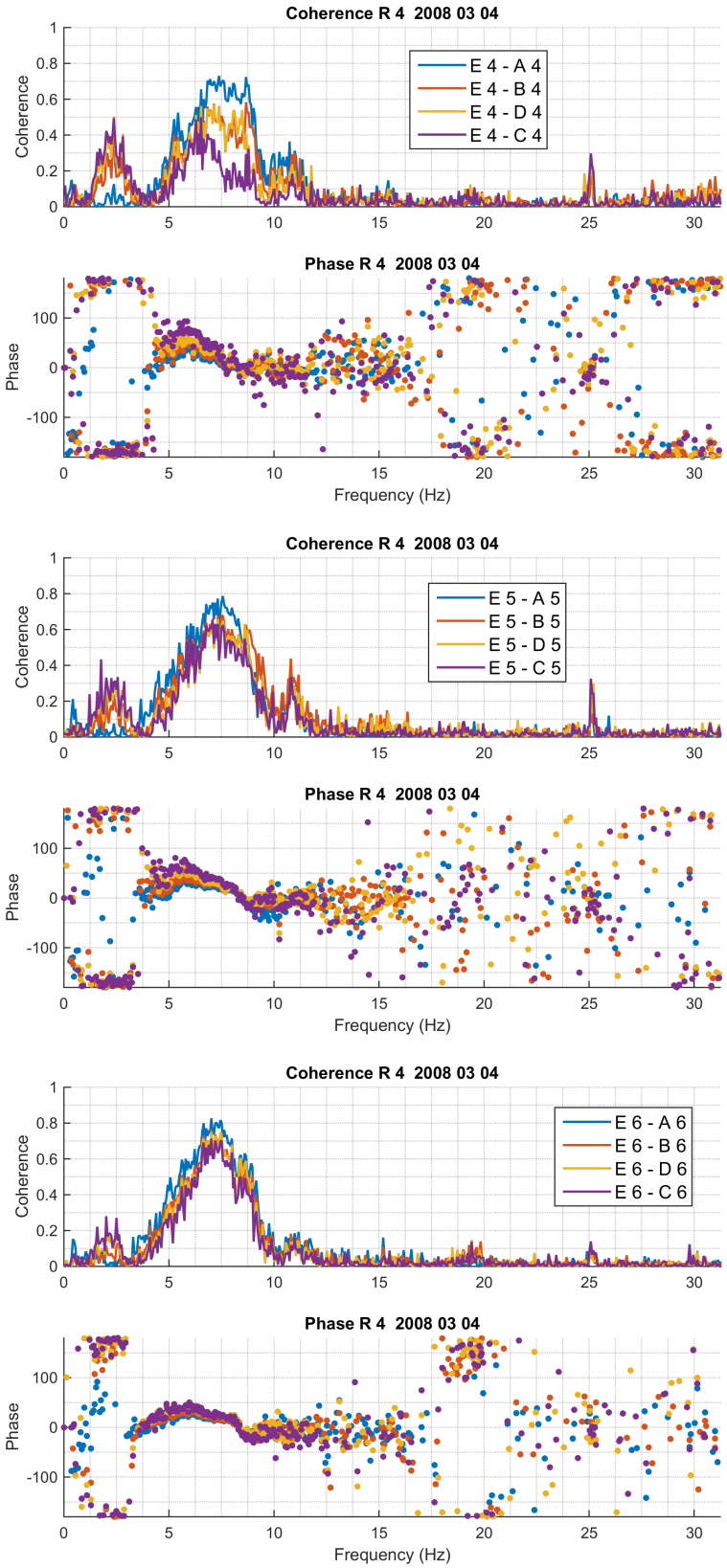

Figure 3.7: Coherence and phase between the pairs A-E, B-E, C-E and D-E for the three lower axial positions.

4. EVALUATION OF NEW EX-CORE MEASUREMENTS FOR BEAM MODE AND TILTING MODE VIBRATIONS IN R3

4.1 Introduction and background

The analysis of core-barrel vibration properties (often abbreviated to CBM, core barrel motion) have been the subject of study both in Sweden and internationally It has also been the subject of the collaboration between Chalmers and Ringhals from the beginning, as it was reported in several previous Stages in the Ringhals diagnostic project [9, 10, 11, 12, 13, 4, 5, 14, 15, 16, 17],

Within the last decade, a series of studies dedicated to core barrel vibrations have been performed in order to analyse and find a suitable explanation for the recent observations of wear at the lower and possibly of the upper core-barrel-support structures, i.e. the lower radial key and the reactor vessel alignment pins in the Ringhals PWRs. In the last few years the main focus in this area was put on the investigation of a double peak observed in the Auto Power Spectrum in the frequency region of the beam mode component, mostly in measurements made in R4. A hypothesis was formulated about the nature of this peak, where it was suggested that the lower frequency peak is due to the beam mode vibrations of the core barrel as a whole, and the higher frequency peak is due to individual fuel assembly vibrations. A test of this hypothesis was one of the main goals of the analysis. A key factor of the analysis was that since the lower frequency peak was assumed to be due to the (coherent) vibrations of the whole core barrel, the symmetry properties of the ex-core detector signals (in-phase and out-of-phase behaviour) could be used to enhance the effect, as well as to condense the quantification to one single parameter by taking combinations of the detector signals. However, as long as the higher frequency mode was assumed to be due to the effect of the independent (incoherent) vibrations of the individual fuel assemblies, no symmetry properties could be utilised, and the results could not be condensed into one single parameter.

In 2014 a further, new assumption was made, in that the main effect of the individual vibrations manifests itself through the combined reactivity effect of all the individually vibrating fuel assemblies. This assumption, through the associated symmetries of the reactivity component, allowed to condense the analysis of the different detector signals into one single parameter even for the higher frequency peak. This hypothesis was tested with a fruitful outcome on the measurements taken at Ringhals-4. In addition, although no double peak was visible in the APDS of the R3 measurements, with the peak separation and curve fitting technique, the two peaks could be separated even in the R3 measurements. Thus, finally, it became possible to distinguish between the beam mode component due to core barrel vibrations and reactivity component associated to the single fuel assembly vibrations. In addition, through numerical simulations, it was also possible to confirm the constant amplitude within one fuel cycle for the peak belonging to the beam mode component, and the varying (increasing) amplitude (within one cycle) of the reactivity component

(individual fuel assembly vibrations), which were in very good agreement with the original hypothesis.

The work in the continuation was therefore not concentrated any longer on the test and proof of the hypothesis, and the associated trend analysis of the evolution of the peak amplitudes during the cycle, rather on checking whether there is any major change in the amplitude and frequency of the beam mode peaks, as compared to the previous measurements, which could indicate an increased play in the lower radial key support. A special circumstance in this aspect is that in 2015, the total power of Ringhals-4 was increased by 18.6 %. Another aspect is that some structural changes took place in R4 relatively recently. The hold-down springs were replaced during the outage in 2013, and the interior parts were lifted out during the outage in 2014 for an inspection. As it was seen and reported in the previous Stage [17], this has changed the shape of the spectra around the beam mode frequency such that the visibility of former double peak has ceased and only one peak could be observed visually. These changes further made the continuation of the CBM analysis and surveillance relevant.

Last but not least, as it was described in the previous stages [16, 17], a new type of pivotal vibration mode, which we named as "tilting" or "wobbling" mode, was discovered. The separation of the tilting mode from the other components is made with methods similar to the other mode separation methods with adding and subtracting the signals in various combinations. The only difference is that for the separation of the tilting mode from the other components, all 8 detectors (the four ex-core detectors at two axial elevations) need to be used. Hence in the routine analysis, the separation of all four components (beam, shell, reactivity and tilting modes) were made, and this is included into this Section.

In the present Stage, the ex-core measurements were made in R3, in which only a smaller fraction of the measurements were made earlier. Hence it will be interesting to see how the results of the present measurements compare with the previous ones.

4.2 Details of the measurements in R3

Three sets of measurements were analysed. The measurements were performed in R3 in cycle 36, on 25 October 2018, as well as on 16 January and 26 March 2019. For simplicity, these will be referred to as Measurement 1, 2 and 3, respectively. The sampling frequency was 62.5 Hz for all three sets of measurements. The measurement points are shown in Table 2. More detailed data regarding settings and general parameters can be found in the measurement protocols from previous measurements, which were performed in an identical manner [18, 19, 20]. Some sample spectra, showing the APSD for each of the 8 individual ex-core detectors, calculated from the corresponding measurement will be presented in the next section.

Table 4.1: The measurement data of the three measurements in Ringhals 3 during 2018-19

Channel	**Measurement point**
0	Time
1	N41U DC
2	N42U DC
3	N43U DC
4	N44U DC
5	N41L DC
6	N42L DC
7	N43L DC
8	N44L DC
9	N41U AC
10	N42U AC
11	N43U AC
12	N44U AC
13	N41L AC
14	N42L AC
15	N43L AC
16	N44L AC

4.3 Analysis of the measurements made on 2018-10-25 (Measurement 1)

4.3.1 Individual spectra of all detectors

The APSDs of all eight individual detector signals are shown in Fig. 4.1. All signals show the two familiar peaks around 8 and 20 Hz for the beam and shell modes, respectively. Similarly to the previous measurements made in R3, as well as in the latest measurements in R4, no double peak is visible at 8 Hz. Rather, similarly to the latest measurements in R4, a small peak is visible around 6 Hz, i.e. it is much more separated from the 8 Hz peak in frequency. On the other hand, the two peaks that can be identified with the beam mode and the reactivity mode (corresponding to the noise induced by the individual fuel assembly vibrations) cannot be visibly separated. This will be reflected in the detailed analysis below. A general observation is that after the replacement of the hold-down springs in R4 during the outage in 2013, and lifting out the interior parts during the outage in 2014 for an inspection, the ex-core detector spectra in R4 and R3 look now rather similar.

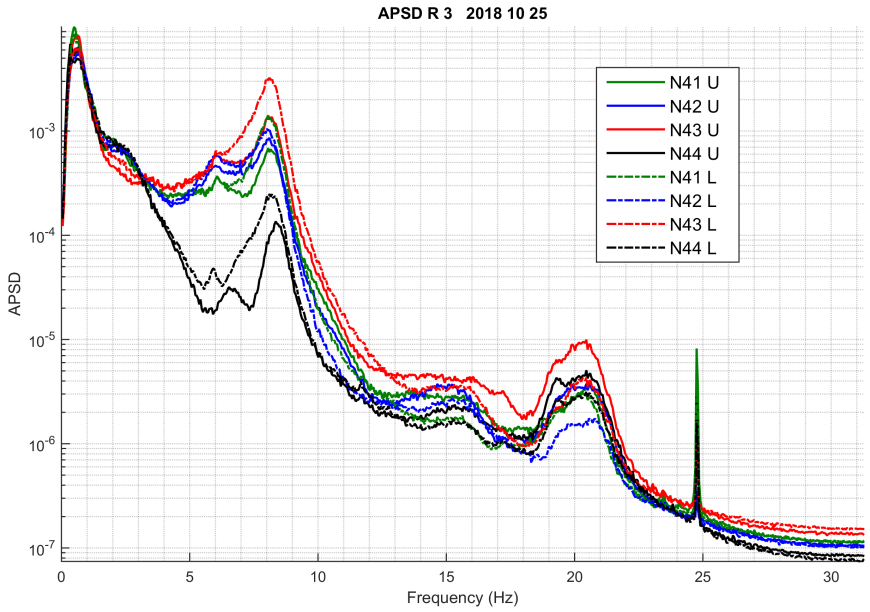

Figure 4.1: APSD of all 8 ex-core detector signals from Measurement 1

.

4.3.2 Results of the mode separation

The beam mode, shell mode, reactivity component and the tilting modes were separated according to the detector signal combination principles as in the previous work. The results are shown for the upper detectors in Fig. 4.2, and for the lower detectors Fig. 4.3. The result of the separation is rather similar for the two cases, as well as to that of the results for R4 in the previous Stage. It is seen that the amplitude of the beam mode is larger for the lower detectors, as expected, whereas the amplitude of the other components is very similar for the upper and lower

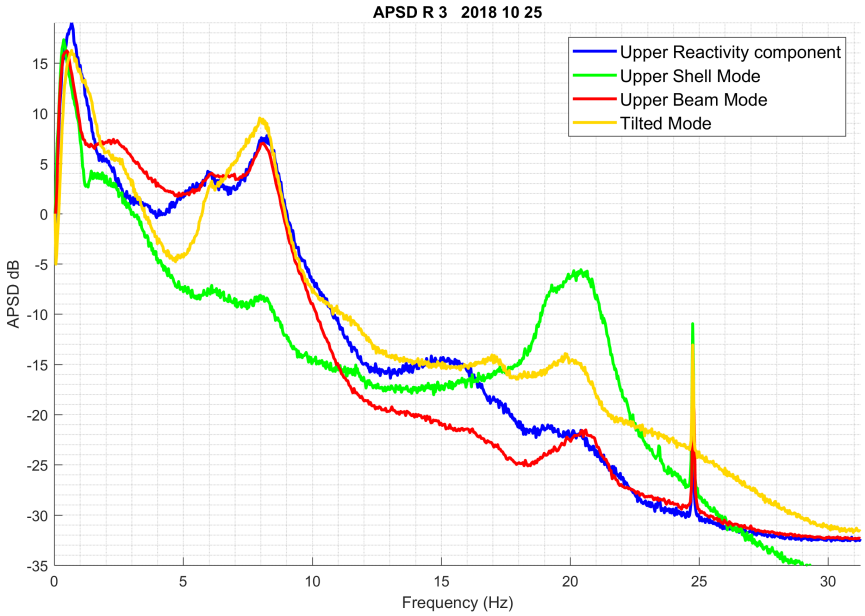

Figure 4.2: APSDs of the beam mode, shell mode, reactivity component and the tilting mode for the upper detectors, extracted from Measurement 1.

detectors. A detailed inspection by enlarging the figures shows that the frequency of the reactivity mode is somewhat higher than that of the beam mode, confirming that they can be identified as Mode 2 and Mode 1 in the previous terminology. Hence the results are in agreement with the results from the previous stages.

One peculiar fact is that the shell mode, which does not show a peak at 8 Hz in the upper detectors signals (which is expected) has a quite distinct peak at 8 Hz in the lower detector signals (not expected). This is somewhat surprising, and there is no direct explanation of it. This phenomenon did not appear in the previous R4 measurements, although in some of the spectra the shell component shows a small, but noticeable peak around 8 Hz [17].

As already mentioned in Section 2, similarly to the results of the previous Stage, reporting on measurements made in R4, one notes a small peak around 15.5 Hz in both the upper and the lower detector signals in the reactivity component. In the previous Stage our interpretation was that since this frequency is twice that of the pendular fuel vibration frequency at 8 Hz, which is also identified as a reactivity effect, the peak at 16 Hz can be attributed to the higher harmonics of the fuel assembly vibrations at the fundamental frequency 8 Hz. However, based on the analysis of the baffle jet effect, and the discussion given in Section 2, it is more likely that this peak is due to the "core flowering" effect, i.e. the zeroth azimuthal mode of the core barrel.

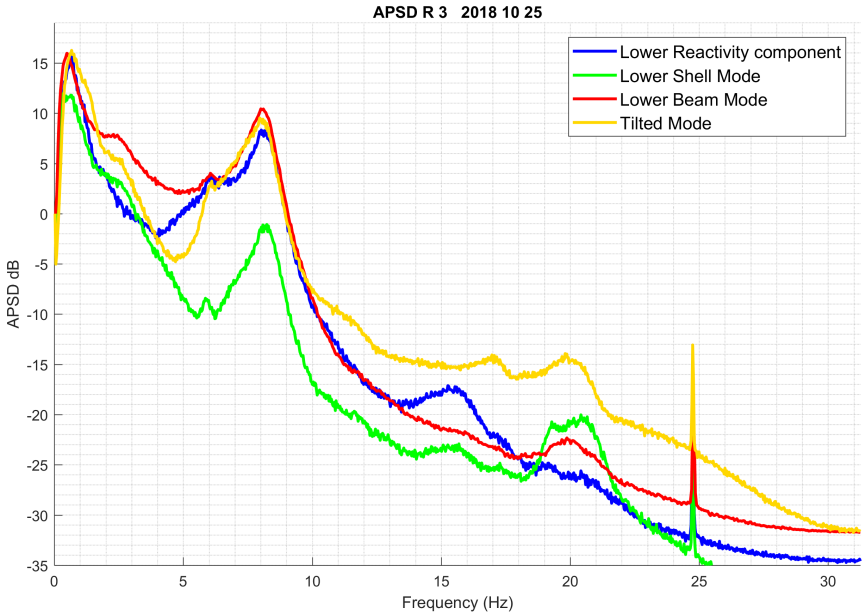

Figure 4.3: APSDs of the beam mode, shell mode, reactivity component and the tilting mode for the lower detectors, extracted from Measurement 1

4.3.3 Phase and coherence relationships between the upper and lower detectors

An analysis of the coherence and the phase relationships between detectors both at the same as well as different axial levels was performed, similarly to that in the previous two stages. The coherence and phase between the diagonally opposite detectors N41 and N42, for both the same and for different axial levels, is shown in Fig. 4.4, and the same for detectors N43 and N44 in Fig. 4.5. The coherence and phase between the upper and lower detectors at the same radial position, for all four detectors, is shown in Fig. 4.6.

The type of phase relationships shown in Figs. 4.4 - 4.6 were reported starting only from Stage 2015, which only concerned measurements in R4. Therefore a comparison with earlier similar plots from R3 is not possible. A comparison with the results from the R4 measurements shows that for the detector pair N41 - N42, Fig. 4.4, the phase behaviour is similar, but the coherence is rather different. Unlike in the R4 measurements, the coherence around 8 Hz is very low, which is rather surprising, given the fact that the APSD peaks are the highest in this fequency region, and the phase is rather solidly 180°, without much scatter, up to about 8 Hz, where it shifts to zero. The coherence has though a medium large peak at around 2 - 3 Hz, which is somewhat more resembling to the former measuremens in R4. One possible explanation of the low coherence at 8 Hz could be if the beam mode vibrations are highly anisotropic, and are perpendicular to the line connecting the detectors N41 - N42. Another possibility is an interference with the tilting mode, which is not investigated in detail in this report.

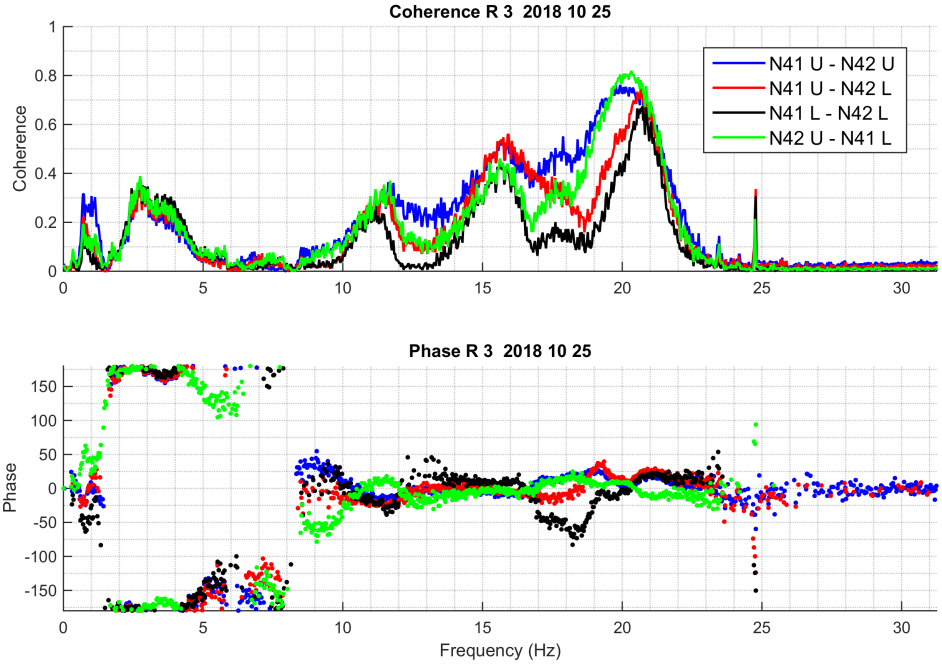

Figure 4.4: The coherence and the phase of the CPSD calculated for the N41U-N42U, N41U-N42L, N41L-N42L and N42U-N41L detector pairs in Measurement 1.

The phase behaviour is in line with the previous R4 measurements, and also with the hypothesis that just below 8 Hz the beam mode vibrations dominate, which is the cause of the out of phase behaviour, after which, at a slightly higher frequency, the reactivity effect of the fuel assembly vibrations take over, which is the cause of the zero phase above 8 Hz.

The picture is rather different for the detector pairs N43 - N44, Fig. 4.5. In a way, it is opposite to the detector pair N41 - N44 in that now the coherence resembles more to the former R4 measurements, but the phase behaviour is different. The coherence is now appreciably higher around 8 Hz, although it is really high (about 0.8) for the combinations N43U - N44U and N43U - N44L, whereas for the other two combinations there are only two smaller peaks with a coherence value about 0.4 each. On the other hand, the phase behaviour differs completely from the previous patterns. Like the coherence, it is different for the combinations N43U - N44U and N43U - N44L and for the other two. All of them start from $\pm 180°$, and then tend linearly to zero which they reach at around 6 Hz, after which they continue to rise linearly again, reaching 180° again at 7 Hz, after which they decrease again linearly, but with a much smaller slope. This also means that there is no zero phase region above 8 Hz.

This type of phase behaviour is unknown from previous measurements, and it is actually rather difficult to interpret. A linear phase between two detectors is an indicator of a (deterministic) time delay between the two signals, which is hardly conceivable for the ex-core detector signals induced by vibrations. One cannot ex-

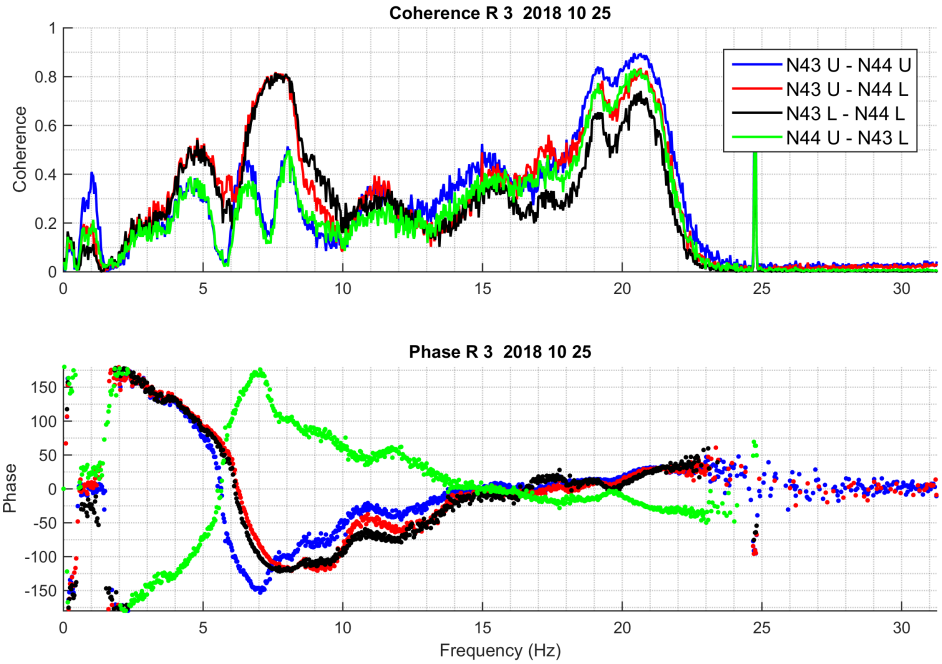

Figure 4.5: The coherence and the phase of the CPSD calculated for the N43U-N44U, N43U-N44L, N43L-N44L and N44U-N43L detector pairs in Measurement 1.

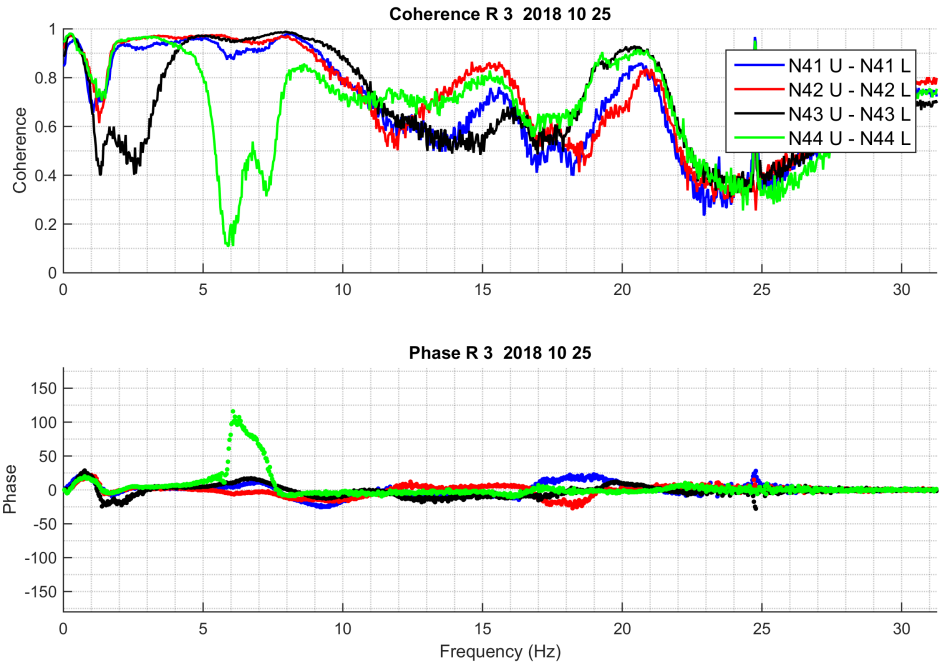

Figure 4.6: The coherence and the phase of the CPSD calculated for the N41U-N41L, N42U-N42L, N43U-N43L and N44U-N44L detector pairs in Measurement 1.

clude though the possibility that the vibrations are periodic and not random, in which case the conclusions drawn from the coherence and phase are not valid, since these are only defined for random processes. However, the large qualitative difference between the phase and coherence between the pairs N41 - N42 on the one hand and N43 - N44 on the other, further amplifies the assumption that the CBM is highly anisotropic. It would be therefore worth following up the CBM analysis in further measurements in R3.

Regarding the axial coherence and phase between detectors at the same radial position, Fig. 4.6, these are partially similar to the previous R4 measurements. There is a dip in the coherence and a deviation from zero phase at 6 Hz only for the detectors N44 upper and lower. All other three radial pairs have high coherence and zero phase throughout this region.

4.4 Analysis of the measurements made on 2019-01-16 (Measurement 2)

4.4.1 Individual spectra of all detectors

The APSDs of all eight individual detector signals are shown in Fig. 4.7. These look very similar to those in Measurement 1. A moderate increase of the amplitude of the 8Hz peak is seen, whereas the amplitude of the peak at 6 Hz has decreased significantly. These features are in line with the observations regarding the earlier R4 measurements.

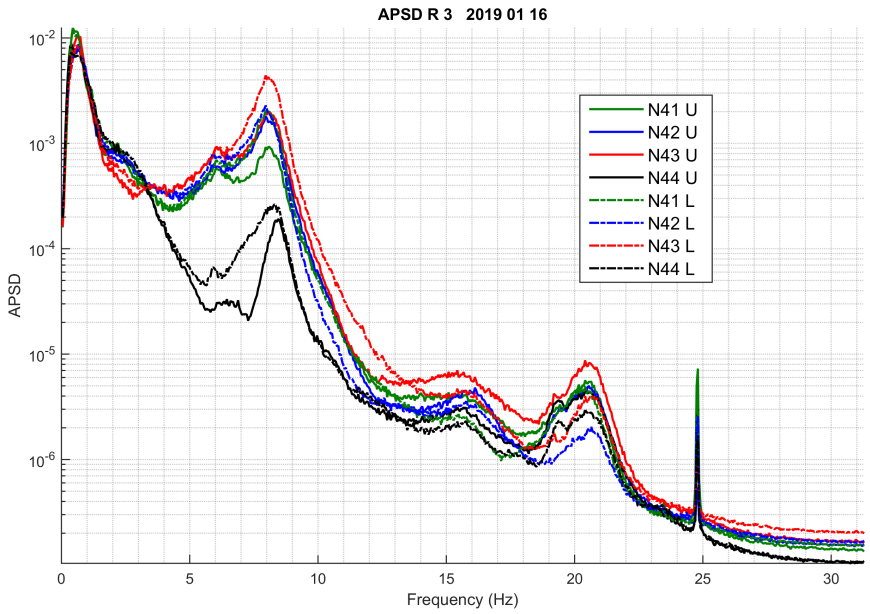

Figure 4.7: APSD of all 8 ex-core detector signals from Measurement 2

.

4.4.2 Results of the mode separation

The results for the separation of the beam mode, shell mode, reactivity component and the tilting modes are shown for the upper detectors in Fig. 4.8, and for the lower detectors in Fig. 4.9. These results are very similar to those of Measurement 1. That is, the amplitude of the beam mode is larger for the lower detectors, and the frequency of the reactivity mode is somewhat higher than that of the beam mode, as expected. Again the shell mode shows a peak at 8 Hz in the lower detectors.

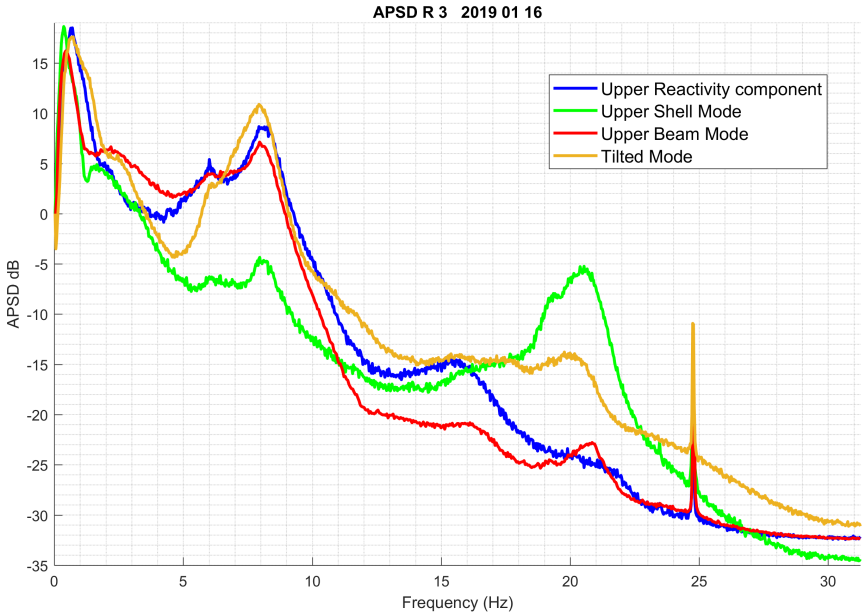

Figure 4.8: APSDs of the beam mode, shell mode, reactivity component and the tilting mode for the upper detectors, extracted from Measurement 2.

4.4.3 Phase and coherence relationships between the upper and lower detectors

The coherence and phase between the diagonally opposite detectors N41 and N42, for both the same and different axial levels, is shown in Fig. 4.10, and the same for detectors N43 and N44 in Fig. 4.11. The coherence and phase between the upper and lower detectors at the same radial position, for all four detectors, is shown in Fig. 4.12.

Similarly to the individual spectra and those from the results of the mode separation, these coherence and phase plots show a full resemblance to those in Measurement 1. Hence the interpretation and remarks remain the same as for the previous measurement.

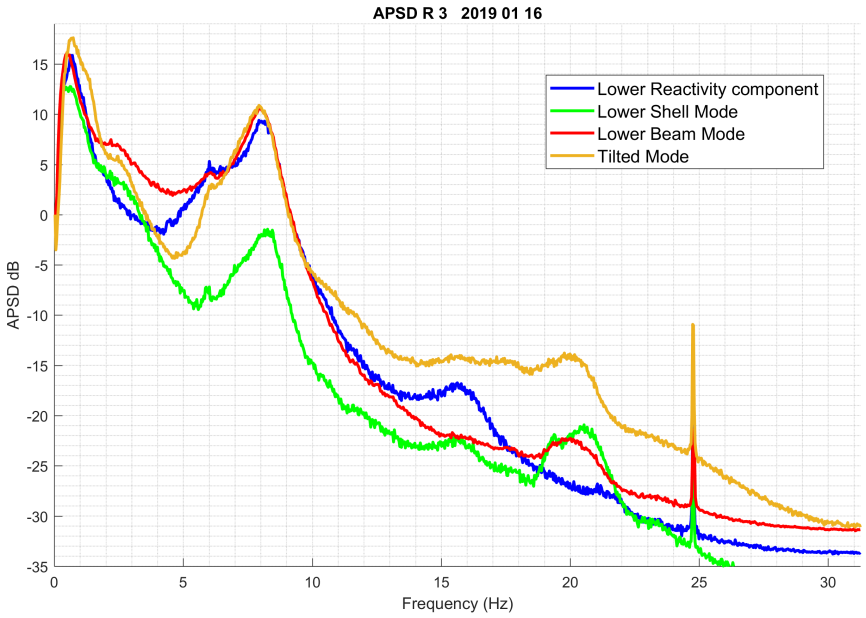

Figure 4.9: APSDs of the beam mode, shell mode, reactivity component and the tilting mode for the lower detectors, extracted from Measurement 2

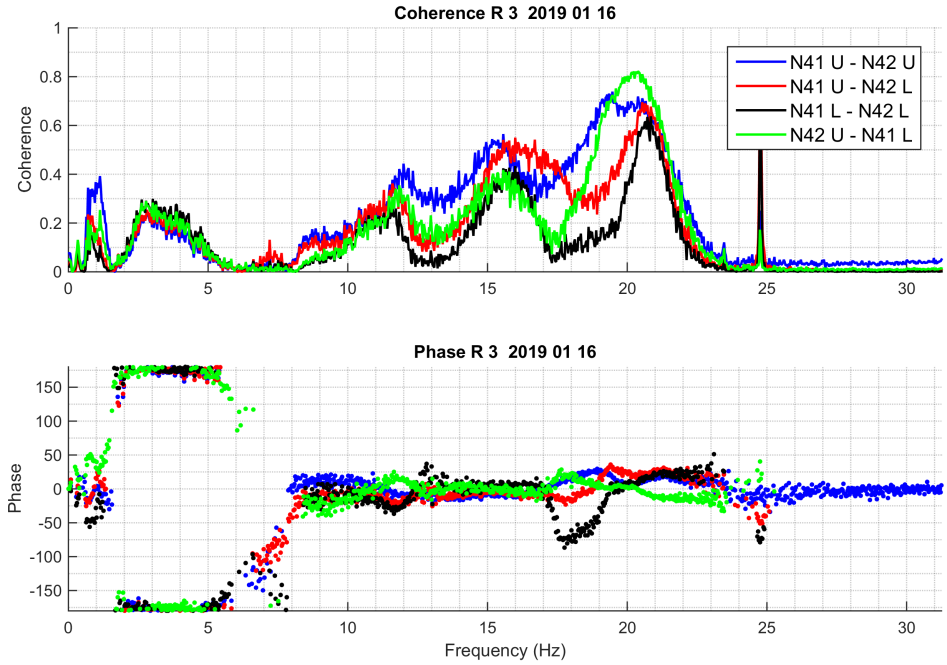

Figure 4.10: The coherence and the phase of the CPSD calculated for the N41U-N42U, N41U-N42L, N41L-N42L and N42U-N41L detector pairs in Measurement 2.

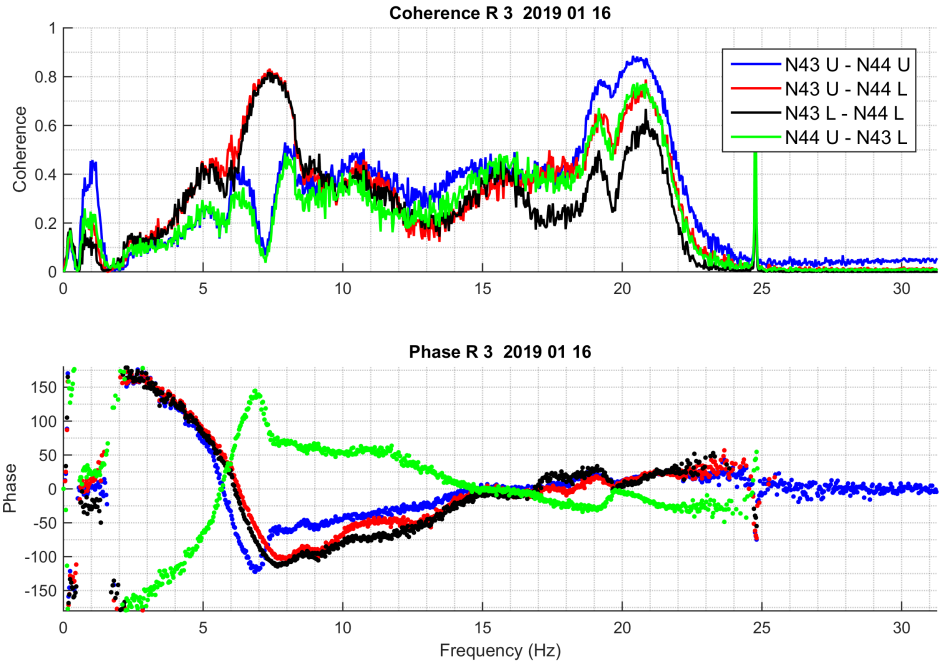

Figure 4.11: The coherence and the phase of the CPSD calculated for the N43U-N44U, N43U-N44L, N43L-N44L and N44U-N43L detector pairs in Measurement 2.

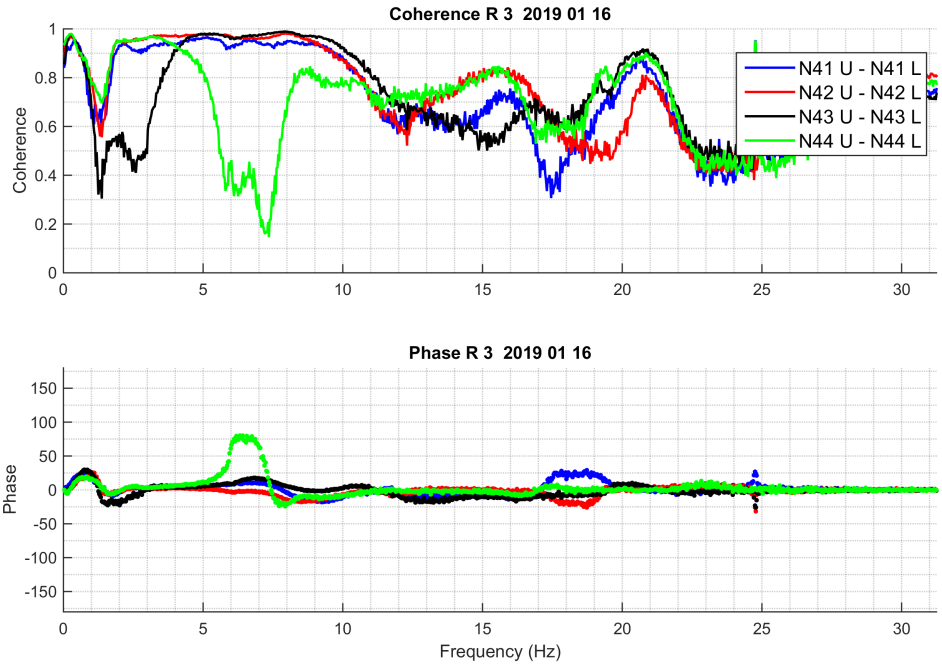

Figure 4.12: The coherence and the phase of the CPSD calculated for the N41U-N41L, N42U-N42L, N43U-N43L and N44U-N44L detector pairs in Measurement 2.

4.5 Analysis of the measurements made on 2019-03-26 (Measurement 3)

4.5.1 Individual spectra of all detectors

The APSDs of all eight individual detector signals are shown in Fig. 4.13. These look again similar to those the previous two measurements. The amplitude of the peak at 6 Hz is still low.

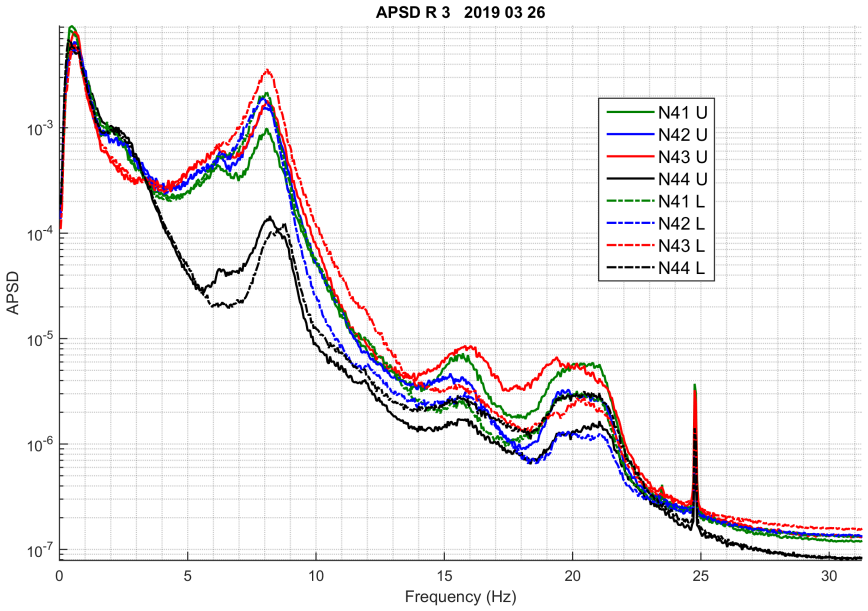

Figure 4.13: APSD of all 8 ex-core detector sigals from Measurement 3

.

4.5.2 Results of the mode separation

The results for the separation of the beam mode, shell mode, reactivity component and the tilting modes are shown for the upper detectors in Fig. 4.14, and for the lower detectors in Fig. 4.15. One difference as compared to the previous two measurements is that the peak in the shell mode at 8 Hz is now clearly visible even in the upper detector signals.

4.5.3 Phase and coherence relationships between the upper and lower detectors

The coherence and phase between the diagonally opposite detectors N41 and N42, for both the same and different axial levels, is shown in Fig. 4.16, and the same for detectors N43 and N44 in Fig. 4.17. The coherence and phase between the upper and lower detectors at the same radial position, for all four detectors, is shown in Fig. 4.18.

Again, apart from some minor differences, the structure of all these plots is similar to the previous two measurements. The deviation of the phase from zero around 7 Hz between the detectors N44U - N44L is now more pronounced.

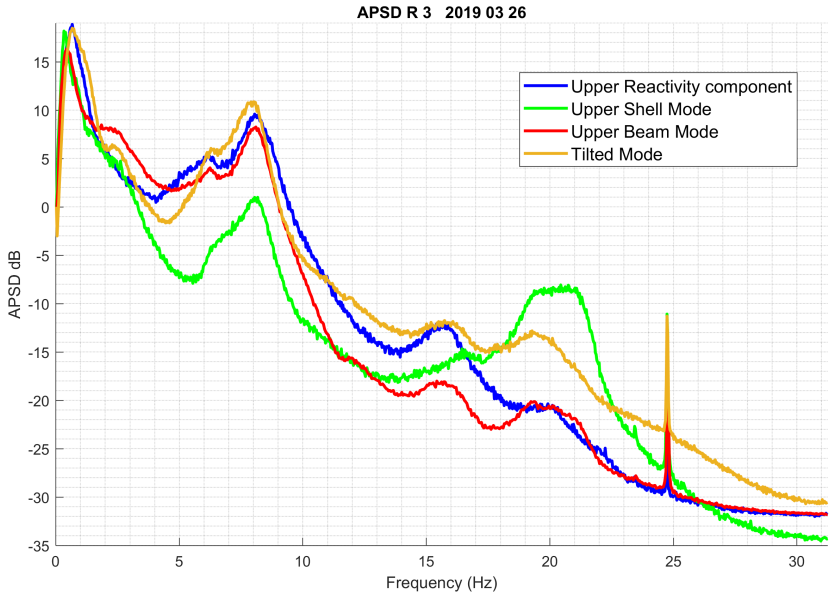

Figure 4.14: APSDs of the beam mode, shell mode, reactivity component and the tilting mode for the upper detectors, extracted from Measurement 3.

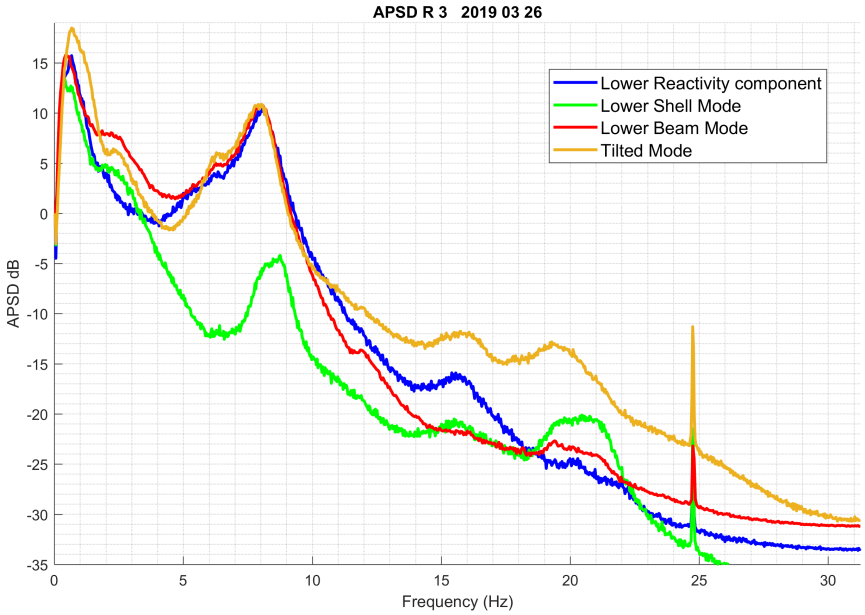

Figure 4.15: APSDs of the beam mode, shell mode, reactivity component and the tilting mode for the lower detectors, extracted from Measurement 3

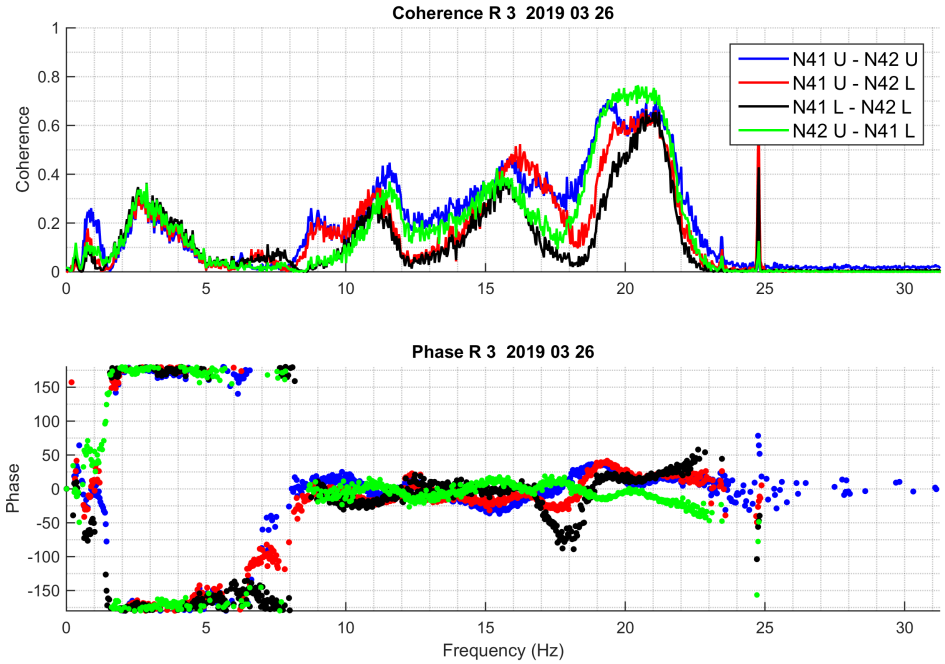

Figure 4.16: The coherence and the phase of the CPSD calculated for the N41U-N42U, N41U-N42L, N41L-N42L and N42U-N41L detector pairs in Measurement 3.

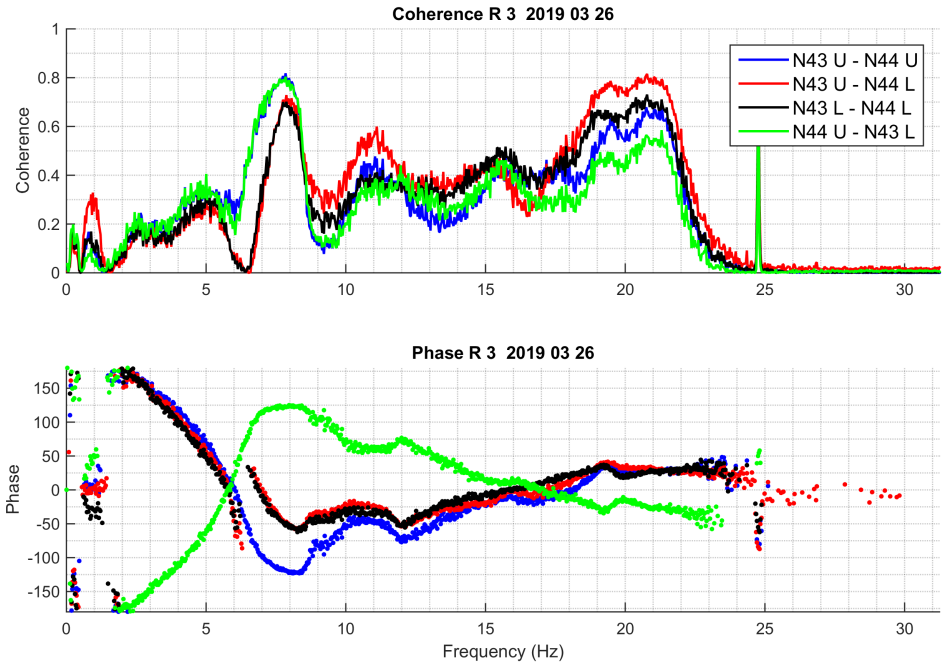

Figure 4.17: The coherence and the phase of the CPSD calculated for the N43U-N44U, N43U-N44L, N43L-N44L and N44U-N43L detector pairs in Measurement 3.

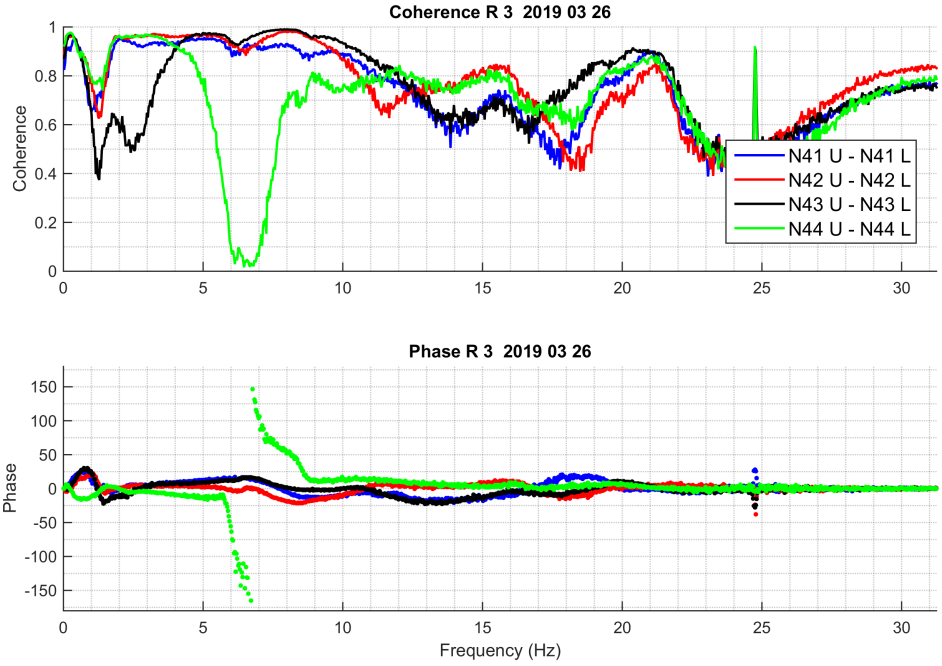

Figure 4.18: The coherence and the phase of the CPSD calculated for the N41U-N41L, N42U-N42L, N43U-N43L and N44U-N44L detector pairs in Measurement 3.

4.6 Trend analysis

As there were three measurements made during the cycle, it was meaningful to try to perform a trend analysis of the amplitudes of the beam and the reactivity peaks at 7 - 8 Hz. In the previous Stage, due to the fact that the two peaks lay so close to each other in frequency, the fitting procedure was incapable to produce useful results for the reactivity mode, hence only a trend analysis of the beam mode peak was made. The situation is somewhat similar in the present case, in that the two peaks lie very close to each other in frequency even in the present measurements. However, with some considerable further effort, in the end it was possible to perform the fitting even for the reactivity component. The results are illustrated in Fig. 4.19 for both the upper and the lower detectors from Measurement 1 and Measurement 3.

The result of the trend analysis for both components is shown in Fig. 4.20. What regards the beam mode, it is rather similar to the last measurements in R4 of the previous Stage, i.e. it is increasing monotonically, and appreciably, during the cycle. Therefore, like the last R4 measurement, it deviates from the previous results, and it is also in disagreement with our assumption that the beam mode amplitude does not increase during the cycle. Also the reactivity component, attributed to the individual fuel assembly vibrations, behaves slightly differently from the previous measurements. For the lower detectors, it shows the expected increase during the cycle, in a higher rate than that of the beam mode peak. However, for the upper detectors, the amplitude increases quite markedly between the first and the second

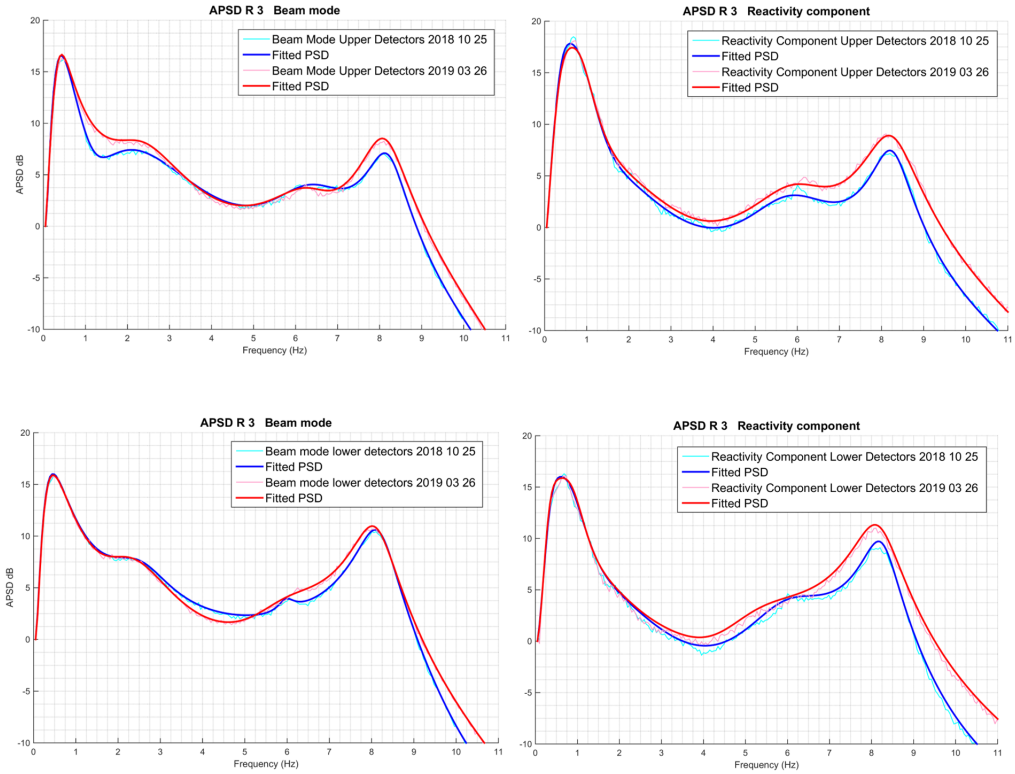

Figure 4.19: Results of the curve fitting for Measurement 1 and 3 to the peak at 8 Hz beam mode (right side) and reactivity component (left side), the upper detectors (upper side) and the lower detectors (lower side).

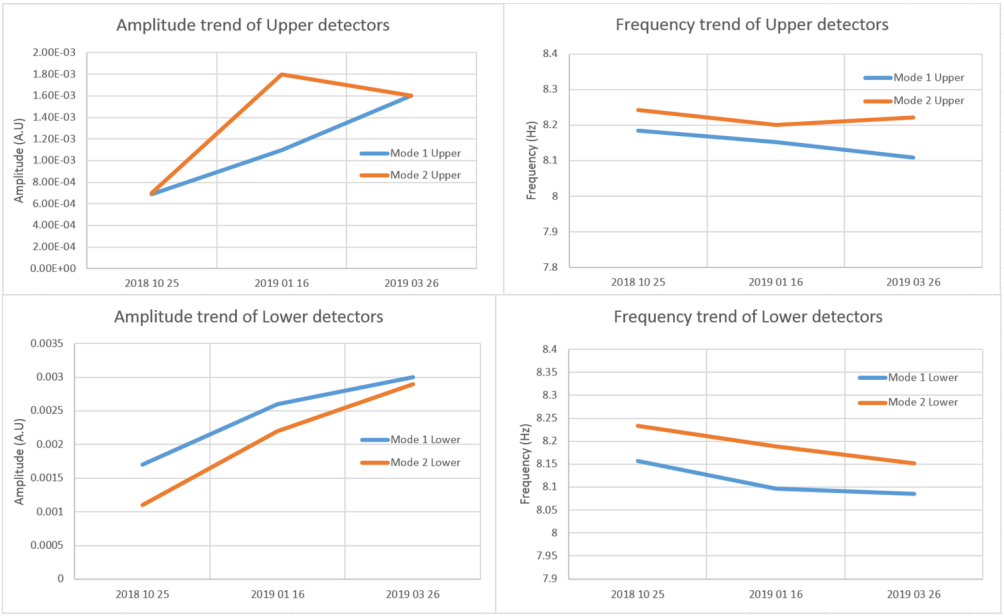

Figure 4.20: Trend analysis of the amplitude and frequency of the beam mode (Mode 1) and the Reactivity component (Mode 2) at 8 Hz for the three measurements made during the cycle.

measurement, but then decreases in the third measurement.

The explanation of this trend behaviour is most likely the same as what we made in the previous Stage, namely that the trend analysis is not reliable when the frequencies of the two peaks (beam mode and reactivity mode) lie too close to each other. Even if, formally, the curve fitting method yields quantitative data for the peak amplitudes, the accuracy of these quantitative data might be low, due to the fact that the mode separation is not sufficiently effective for the curve fitting, and the separated componenets might be "contaminated" with each other.

However, one can at least claim that the results of the CBM analysis of the R3 measurements, performed in the present Stage, are in a qualitative agreement with the last measurements made in R4. Further analysis of measurements in R3 would be advantageous to see the consistency of these results.

5. DEVELOPMENT OF A METHOD TO USE THE EIGENVALUE SEPARATION IN NOISE ANALYSIS FOR CHARACTERISING OF REGIONAL POWER OSCILLATIONS AND UNDERSTANDING THE ROLE OF LOOSELY COUPLED CORES IN THE DEVELOPMENT OF REGIONAL INSTABILITIES

The space-time properties of the response of reactor cores to various types of perturbations have been studied extensively in the past. One of these methods is based on the concept of "eigenvalue separation", introduced by Stacey [21] to characterise the space-time behaviour of reactor cores under transients, including space-dependent xenon oscillations. The expression is commonly abbreviated in text as ES, in some cases as EVS, and its quantitative value in expressions as (E.S.) or $(\text{E.S.})_n$.

The ES between the static eigenfunctions ϕ_n and ϕ_0, $n > 0$ is defined as

$$(E.S.)_n = \frac{1}{k_n} - \frac{1}{k_0} \geq 0 \tag{5.1}$$

where k_n and k_0 are the corresponding eigenvalues, k_0 being the effective multiplication factor. The case $n = 1$ has a special significance, hence it is often used without an index, and in many cases the term "eigenvalue separation" is used for this quantity:

$$(E.S.) \equiv (E.S.)_1 = \frac{1}{k_1} - \frac{1}{k_0} \geq 0. \tag{5.2}$$

The potential of the concept has been investigated in the past extensively both for describing space-time behaviour under perturbations, the coupling constant of coupled cores, as well as determination of the eigenvalue separation from flux tilt measurements and noise correlation measurements [22, 23, 24, 25, 26, 27, 28, 29, 30, 31, 32, 33, 34, 35, 36, 37]. These investigations confirmed that a small ES increases the proneness of the system to instabilities and enhances the space dependent behaviour of the system. Systems consisting of loosely coupled regions (such as early types of breeder reactors with highly enriched regions separated by blankets containing depleted uranium or other fertile material) have a small eigenvalue separation, hence they show strongly space dependent kinetic properties.

At the same time it has to be noted that the objective of these studies was mostly the determination of the ES by numerical or experimental methods, nearly exclusively performed by static methods, or by measurement of the inherent neutron noise in the unperturbed system. A great deal of work was spent on studying the dependence of the magnitude of the ES on static system parameters, including the comparison of non-perturbed and perturbed static systems, without explicitly solving the time- or frequency dependent problem. In other words, the dependence of the dynamic response of the core for a certain perturbation on the magnitude of the ES has not been a subject of study.

The main objective of the present study is to fill this gap. We shall here investigate the significance of the ES on the dynamic response of a system to small stationary perturbations, leading to what is called power reactor noise. The space dependent character of the dynamic response of a core to perturbations, in terms of point kinetic or space-dependent behaviour has traditionally been characterised in terms of system size and the frequency [38]. These conclusions are drawn directly from the form of the space- and frequency dependent Green's function of the system, without the need of calculating higher order eigenfunctions and eigenvalues. Expressing the neutron noise in form of an expansion in static eigenfunctions with frequency dependent coefficients lends the possibility of investigating these properties in terms of the eigenvalue separation, thus it gives an alternative way of description. This will also illuminate the role of the ES, and will, among others, give alternative insight into already known characteristics, such as the appearance of global and regional oscillations in boiling water reactors (BWRs) from a new angle of view.

In the following, first it will be shown that a general formal solution for the neutron noise in terms of the static eigenfunctions automatically leads to the appearance of the ES in the equations. The characteristics of the neutron noise will then be discussed in terms of the ES and that of the perturbation. After that the relationship between the ES and the coupling strength in a multi-region system will be illustrated in an extreme, in fact pathological, case, which is nevertheless useful to give deepened insight. Finally a quantitative investigation of the dependence of the properties of the neutron noise in a loosely coupled system on the ES will be performed and the results discussed.

5.1 General principles: neutron noise in terms of the ES

The ES will now be put into the context of neutron noise theory, which concerns the response of the system to small stationary perturbations. One of the basic questions in the theory of neutron noise is the spatial character of the response to a small perturbation, i.e. whether it is point kinetic or space dependent, and how the system behaves in the limit of low frequencies.

The theory of power reactor noise is described in Ref. [38], here only a condensed description will be given in one-group diffusion theory in a slab reactor model (1-D geometry) with one group of delayed neutron precursors. As usual in noise analysis problems, the discussion in the forthcoming refers to systems which are initially critical, i.e. $k_0 \equiv k = 1$. The corresponding static one-group diffusion equation reads as

$$\Delta\phi_0(\boldsymbol{r}) + B_0^2\phi_0(\boldsymbol{r}) = 0 \tag{5.3}$$

with the one-group theory expression of the static buckling as

$$B_0^2 = \frac{\nu\Sigma_f - \Sigma_a}{D} \tag{5.4}$$

The system will then be perturbed around the critical state by small stationary fluctuations of the cross sections, which will lead to a time (frequency) dependence

of the neutron flux. For simplicity it will be assumed that only the absorption cross section is fluctuating[1], i.e.

$$\Sigma_a(\boldsymbol{r}) \to \Sigma_a(\boldsymbol{r},t) = \Sigma_a(\boldsymbol{r}) + \delta\Sigma_a(\boldsymbol{r},t). \tag{5.5}$$

The resulting space- and time-dependent neutron flux will also be split into a mean value (the critical flux) and fluctuations around it, i.e.

$$\phi_0(\boldsymbol{r}) \to \phi(\boldsymbol{r},t) = \phi_0(\boldsymbol{r}) + \delta\phi(\boldsymbol{r},t). \tag{5.6}$$

After linearisation, a temporal Fourier transform and elimination of the delayed neutron precursors, the space- and frequency dependent neutron noise will be given as the solution of the equation [38]

$$\Delta\delta\phi(\boldsymbol{r},\omega) + B^2(\omega)\delta\phi(\boldsymbol{r},\omega) = S(\boldsymbol{r},\omega) \equiv \frac{\delta\Sigma_a(\boldsymbol{r},\omega)\phi_0(\boldsymbol{r})}{D} \tag{5.7}$$

where the temporal Fourier transform $\delta\phi(\boldsymbol{r},\omega)$ of $\delta\phi(\boldsymbol{r},t)$ is defined as

$$\delta\phi(\boldsymbol{r},\omega) = \int_{-\infty}^{\infty} e^{-i\,\omega t}\delta\phi(\boldsymbol{r},t)dt, \tag{5.8}$$

and similarly for $\delta\Sigma_a(\boldsymbol{r},\omega)$. The frequency dependent buckling $B^2(\omega)$ is given as

$$B^2(\omega) = B_0^2\left(1 - \frac{\nu\Sigma_f}{(\nu\Sigma_f - \Sigma_a)\,G_0(\omega)}\right) = B_0^2 - \frac{\nu\Sigma_f}{D\,G_0(\omega)} = B_0^2\left(1 - \frac{1}{\rho_\infty G_0(\omega)}\right) \tag{5.9}$$

with $G_0(\omega)$ being the zero power reactor transfer function

$$G_0(\omega) = \frac{1}{i\omega\left(\Lambda + \frac{\beta}{i\omega+\lambda}\right)}; \qquad \Lambda = \frac{1}{v\nu\Sigma_f} \tag{5.10}$$

and

$$\rho_\infty = 1 - \frac{1}{k_\infty} = \frac{\nu\Sigma_f - \Sigma_a}{\nu\Sigma_f} \tag{5.11}$$

being the infinite system reactivity.

The usual discussion on the properties of the system response is based on the solution for the Green's function of Eq. (5.7), obeying the equation

$$\Delta_{\boldsymbol{r}} G(\boldsymbol{r},\boldsymbol{r'},\omega) + B^2(\omega)G(\boldsymbol{r},\boldsymbol{r'},\omega) = \delta(\boldsymbol{r}-\boldsymbol{r'}). \tag{5.12}$$

For homogeneous systems, $B^2(\omega)$ is space-independent, and the Green's function can be given analytically. Its properties can then be analysed in terms of the dependence of $B^2(\omega)$ on the system size (related to ρ_∞) and the frequency (through $G_0(\omega)$). The analysis readily shows that for perturbations having a non-zero reactivity effect, in the limit of small frequency or small system size, the system behaves in a point kinetic manner, with the amplitude of the response diverging when $\omega \to 0$.

[1]Including fluctuations of the fission cross section is straightforward; they are neglected here only for the transparency and clarity of the description.

The discussion of the same properties in terms of the ES is based on the representation of the space and frequency dependent neutron noise in the form of a series expansion by the static spatial eigenfunctions multiplied by frequency dependent amplitudes. The first term in such a series is the point kinetic component of the noise, whereas the rest , i.e. the aggregate of all higher order eigenfunctions, represents the space dependent component. For this we define the higher order eigenfunctions as

$$\Delta\phi_n(\boldsymbol{r}) + B_n^2\phi_n(\boldsymbol{r}) = 0 \tag{5.13}$$

where now

$$B_n^2 = \frac{\frac{\nu\Sigma_f}{k_n} - \Sigma_a}{D} \tag{5.14}$$

Formally, Eq. (5.14) is valid also for the fundamental mode, i.e. for $n = 0$, with $k_0 = 1$, since the unperturbed system is critical.

The solution of Eq. (5.7) is now constructed by an expansion into the spatial eigenfunctions $\phi_n(\boldsymbol{r})$ with frequency dependent coefficients:

$$\delta\phi(\boldsymbol{r},\omega) = \sum_{n=0}^{\infty} a_n(\omega)\phi_n(\boldsymbol{r}) = a_0(\omega)\phi_0(\boldsymbol{r}) + \sum_{n=1}^{\infty} a_n(\omega)\phi_n(\boldsymbol{r}) \tag{5.15}$$

Here, the splitting of the sum by separating its first term is only made because it is equal to the point kinetic component of the noise. Similar expansions of the perturbed flux, although for static cases, were considered in connection with the eigenvalue separation in [22, 25, 30].

Substituting (5.15) into (5.7), and using Eq. (5.13) for $\phi_n(\boldsymbol{r})$ yields

$$\sum_{n=0}^{\infty} a_n(\omega)\left[-B_n^2 + B^2(\omega)\right]\phi_n(\boldsymbol{r}) = \frac{\delta\Sigma_a(\boldsymbol{r},\omega)\phi_0(\boldsymbol{r})}{D} \tag{5.16}$$

Using the definition of the eigenvalue separation (5.1) and the form of $B^2(\omega)$ and B_0^2 given by Eqs (5.4), (5.9) and (5.14), one finds readily that

$$D\left[-B_n^2 + B^2(\omega)\right] = -\nu\Sigma_f\left[(E.S.)_n + G_0^{-1}(\omega)\right], \tag{5.17}$$

where, obviously $(E.S.)_0 = 0$. Hence, Eq. (5.16) can be re-written in the form

$$-\sum_{n=0}^{\infty} a_n(\omega)\nu\Sigma_f\left[(E.S.)_n + G_0^{-1}(\omega)\right]\phi_n(\boldsymbol{r}) = \delta\Sigma_a(\boldsymbol{r},\omega)\phi_0(\boldsymbol{r}) \tag{5.18}$$

For a homogeneous system, i.e. when $B^2(\omega)$ is space-independent, the equations for the $a_n(\omega)$ for different values of n decouple, due to the orthogonality relations of the static eigenfunctions $\phi_n(\boldsymbol{r})$. Hence, multiplying (5.18) by $\phi_k(\boldsymbol{r})$, integrating over the reactor volume V_R, and also utilising (5.9) (5.13) and (5.14), one obtains

$$a_k(\omega) = -\frac{\int_{V_R}\delta\Sigma_a(\boldsymbol{r},\omega)\phi_0(\boldsymbol{r})\phi_k(\boldsymbol{r})d\boldsymbol{r}}{\nu\Sigma_f\left[(E.S.)_n + G_0^{-1}(\omega)\right]\int_{V_R}\phi_k^2(\boldsymbol{r})d\boldsymbol{r}}; \qquad k = 0, 1, 2\ldots \tag{5.19}$$

Using this in (5.15) and also by recalling the perturbation formula of calculating the reactivity in first order of the perturbation yields

$$\delta\phi(\boldsymbol{r},\omega) = \rho(\omega)G_0(\omega)\phi_0(\boldsymbol{r}) + \sum_{n=1}^{\infty} \frac{\delta\rho_n(\omega)}{\left[(E.S.)_n + G_0^{-1}(\omega)\right]}\phi_n(\boldsymbol{r}) \tag{5.20}$$

Here the definition

$$\delta\rho_n(\omega) = \frac{-\int_{V_R}\delta\Sigma_a(\boldsymbol{r},\omega)\phi_0(\boldsymbol{r})\phi_n(\boldsymbol{r})d\boldsymbol{r}}{\nu\Sigma_f\int_{V_R}\phi_n^2(\boldsymbol{r})d\boldsymbol{r}}; \qquad n = 0,1,2,\ldots \tag{5.21}$$

was introduced. It is to be stressed that $\delta\rho_n(\omega)$ has nothing to do with the static higher order reactivity $\rho_n = 1 - 1/k_n$, which is a property of the unperturbed system; rather, it stands for the higher order reactivity effect of the *perturbation* which excites the nth higher order mode in the response of the system[2] [22]. In other words, $\delta\rho_n(\omega)$ can be considered as the generalisation of the conventional perturbation theory formula for the reactivity. In analogy with the conventional reactivity $\rho(\omega) \equiv \delta\rho_0(\omega)$, which is the projection of the perturbation $S(\boldsymbol{r},\omega)$ to the fundamental mode $\phi_0(\boldsymbol{r})$ and which excites the fundamental mode (i.e. the point kinetic or "reactivity" component of the noise), for $n \geq 1$, the term $\delta\rho_n(\omega)$ can be interpreted as the projection of the perturbation to the n-th higher harmonic, and which thus excites the n-th higher order eigenfunction.

From Eqs (5.20) and (5.21) an analysis of the induced reactor noise, similar to the one based on the analytic solution for the Green's function mentioned above, can be made as follows.

1. For $\omega \to 0$, $G_0(\omega) \to \infty$. Since $(E.S.)_0 = 0$, whereas $(E.S.)_n > 0$ for $n \geq 1$, if $\rho(\omega) \neq 0$, the first term will dominate, and point kinetic behaviour will prevail.

2. If the perturbation is spatially homogeneous (space-independent), i.e. $\delta\Sigma_a(\boldsymbol{r},\omega) = \delta\Sigma_a(\omega)$, then, due to the orthogonality relationships between ϕ_0 and ϕ_n for $n > 0$ in Eq. (5.21), $\delta\rho_n(\omega) = 0$ and hence $a_n(\omega) = 0$ for $n \geq 1$. Thus point-reactor behaviour exists for any ω (i.e. even for arbitrarily high frequencies).

3. If $\delta\Sigma_a(\boldsymbol{r},\omega)$ is an odd (asymmetric) function of $\boldsymbol{r}$, or more generally, in any case when
$$\int_{V_R}\delta\Sigma_a(\boldsymbol{r},\omega)\,\phi_0^2(\boldsymbol{r})d\boldsymbol{r} = 0, \tag{5.22}$$
one has $\rho(\omega) = 0$, and hence the reactivity term (point-reactor term) equals zero. That is, in such cases, point-reactor behaviour never exists, not even for very low frequencies.

[2] Actually, for full consistency, $\rho(\omega)$ should also be denoted as $\delta\rho_0(\omega)$. However, the zero index and the prefix δ was dropped because the notation $\rho(\omega)$ has been widely used for the traditional reactivity effect of a stationary perturbation. Hopefully this will not lead to any confusion.

These remarks will now be complemented with further aspects which are related to the eigenvalue separation. Assume now that in Eq. (5.20), one has $(E.S.)_1 \equiv (E.S.) = \varepsilon << 1$, more concretely $\varepsilon << \beta$, which implies $k_1 \approx k_0$. We will also assume that $(E.S.)_n >> (E.S.)$, and for the sake of the argument also that $(E.S.)_n > \beta$ for $n \geq 2$. Then, separating out the first term of the sum in the r.h.s. of (5.20), one can write

$$\delta\phi(\boldsymbol{r},\omega) = \rho(\omega)G_0(\omega)\phi_0(\boldsymbol{r}) + \frac{\delta\rho_1(\omega)}{\varepsilon + G_0^{-1}(\omega)}\phi_1(\boldsymbol{r}) + \sum_{n=2}^{\infty}\frac{\delta\rho_n(\omega)}{\left[(E.S.)_n + G_0^{-1}(\omega)\right]}\phi_n(\boldsymbol{r}) \tag{5.23}$$

Since at the plateau frequencies $\lambda \leq \omega \leq \beta/\Lambda$, the amplitude of the zero power transfer function is $|G_0(\omega)| \approx 1/\beta$, with the above assumptions (and provided that all the ρ_n are larger than zero and of comparable order of amplitude), at the plateau frequencies, on the right hand sidek of Eq. (5.23) the first two terms will dominate over the rest. Thus, for plateau frequencies one can write

$$\delta\phi(\boldsymbol{r},\omega) \approx \rho(\omega)G_0(\omega)\phi_0(\boldsymbol{r}) + \delta\rho_1(\omega)G_0(\omega)\phi_1(\boldsymbol{r}) \tag{5.24}$$

This form is of course only valid at plateau frequencies and below, but only until $|G_0(\omega)| < 1/\varepsilon$. For any given value of $(E.S.) = \varepsilon$, in the limit $\omega \to 0$, if ω is sufficiently small, eventually the first term (the point kinetic term) on the right hand side of Eqs (5.23) or (5.24) will dominate. However, if ε is sufficiently small, this will happen only at very low frequencies. That is, the form (5.23) will remain valid, with its second term being comparable to the point kinetic term, and if $|\delta\rho_1(\omega)| > |\rho(\omega)|$, it will even dominate over it, even for frequencies far below the plateau region. This means that space-dependent behaviour, i.e. deviation from the point kinetic behaviour, will prevail for much lower frequencies than usual.

The above is of course a consequence of the fact that in this case even the first harmonic is "close to critical". A non-zero, but sufficiently small ES means, according to the above analysis, that space dependent behaviour will be sustained even for low frequencies, way below the plateau frequencies, and also the amplitude of the space dependent part of the response can be rather high. In the hypothetical case of $(E.S.) = 0$ (such a pathological case will be discussed below), a perturbation which can excite the first higher order mode will lead to a diverging amplitude for $\omega \to 0$, for exactly the same reasons as for the point kinetic term in the cases when $\rho(\omega) \neq 0$.

The influence of the ES on the stability of the system can thus be refined in view of the above analysis. Let us define a stable system as one characterised with a small amplitude response to a certain perturbation and an unstable system as one with a large amplitude response to the same perturbation. Then, one can say that systems with a large ES are unstable for perturbations with a reactivity effect at low frequencies, but are stable for perturbations without (or with a very small) reactivity effect. Systems with a very small ES are still unstable for perturbations with a reactivity effect at low frequencies, but they will be also unstable for perturbations without a reactivity effect, as long as $\delta\rho_1(\omega) \neq 0$. Since, in reality, many

perturbations are of local character (moving of an individual control rod, fuel or control rod vibrations in a PWR, local channel blockage in a BWR etc), for these cases it is valid that $|\delta\rho_1(\omega)| \approx |\rho(\omega)|$. For an asymmetric perturbation, for which Eq. (5.22) holds exactly or approximately, one has even $|\delta\rho_1(\omega)| >> |\rho(\omega)|$. For such perturbations, a systems will become unstable for low frequencies if it has a small ES, despite that there is no reactivity perturbation. This is for instance the case of regional (out-of-phase) BWR oscillations [39, 40, 41, 42].

One drawback of the discussion so far, which makes it somewhat trivial, is that the formulae are only valid for homogeneous systems. For homogeneous systems the only way of achieving a small $(E.S.)$ is to have a large system size. In that case not only the fundamental $(E.S.)$ but all the higher order $(E.S.)_n$ will be small, and the separation of the first higher eigenfunction as in (5.23) is not justified. Physically, this means that generally, many modes will be excited simultaneously. A localised perturbation will hence lead to a space-dependent response, in which a large number of higher order modes co-exist (such as in a localised response), and the first harmonic is not favoured over the others in general.

To have a small $(E.S.)$ but much larger $(E.S.)_n$ for $n > 1$, one needs a loosely coupled core, i.e. an inhomogeneous system. A typical, and for the practical applications most relevant case is a piecewise homogeneous system, in which high multiplication areas (the fissile regions) are separated by low multiplication regions (e.g. breeding blanket regions). For such systems, in which $\nu\Sigma_f$, and hence the prompt neutron generation time $1/(v\,\nu\Sigma_f)$ are different for the different regions, the corresponding frequency-dependent functions of the respective regions, which are analogous in frequency dependence to the traditional $G_0(\omega)$, will also be different for the different regions in (5.18) (c.f. Eq. (5.10)).

Because of this, the orthogonality relations separating the equations for the $a_n(\omega)$ are not valid any longer. Thus, the equations for the $a_i(\omega)$ for different i values will not decouple, and their determinaton becomes cumbersome. Although, then, the conclusions drawn in the previous derivations related to homogeneous systems on the asymptotic behaviour of the $a_i(\omega)$ are not directly transferable to inhomogeneous systems, on physical grounds it can be expected (and our quantitative studies in Section 5.3.2 will confirm it) that the solution can still be approximated by the first two terms as

$$\delta\phi(\boldsymbol{r},\omega) \approx a_0(\omega)\phi_0(\boldsymbol{r}) + a_1(\omega)\phi_1(\boldsymbol{r}), \tag{5.25}$$

although the quantities a_0 and a_1 will not be simply expressible with the reactivities $\delta\rho_n(\omega)$, and the zero power reactor transfer function $G_0(\omega)$ of the full system.

On the other hand, in a simple one-dimensional system of two homogeneous coupled cores separated with a homogeneous region of low or no multiplication, analytical solutions can be obtained for the full space-frequency dependent case by constructing closed form analytical solutions in each region, with coefficients that are determined from the interface and boundary conditions. From the full solution, the frequency dependent coefficients of the various modes can be extracted by projection of the full solution to the respective eigenfunctions, and their frequency dependence investigated quantitatively. Such a case will be considered in Section 5.3.2. Before

turning to such a realistic case, we will consider an extreme model case with exactly zero eigenvalue separation, because it will give insight into the properties of the ES and its influence on the system behaviour.

5.2 Illustration in a simple extreme case

The system to be considered is admittedly pathological, because it will consist of two cores completely separated from each other by e.g. a "black" absorbing material. This means that there is no neutronic coupling between the two cores. Of course, in practice there is no reason why one should treat two independent cores as one system. However, they can be considered as the limiting case of two loosely coupled systems, in which the coupling strength tends to zero, hence it is an extreme (unrealistic) limit of a realistic case.

We will use a one-dimensional one-group model, the two cores lying symmetrically around the origin with the extrapolated boundaries of the outer edges of the two cores lying at $x = \pm a$, with an extrapolated thickness H each, $H < a$. By having no coupling, both cores can be critical, supercritical or subcritical individually, and the compound system is critical, supercritical or subcritical if, asymptotically, the flux is constant at least in one of the systems and not diverging in the other, or diverging at least in one of the cores, or vanishes in both cores, respectively. For simplicity, we chose the same material for both cores, hence they will be critical, subcritical or supercritical simultaneously, and we will consider the initial system as critical. That means that one has

$$B_0 = \frac{\pi}{H} \tag{5.26}$$

and $k_0 = 1$. An important point is that the k_n eigenvalues refer to the aggregate system (for the two cores together as one system), i.e. no different k_n or B_n^2 values are permitted separately for the two cores. The corresponding fundamental mode flux, $\phi_0(x)$ is equal to

$$\begin{aligned} \phi_0(x) &= A_0 \sin[B_0(x+a)] && \text{for} \quad -a < x < -a + H; \\ \phi_0(x) &= A_0 \sin[B_0(x-a+H)] && \text{for} \quad a - H < x < a; \\ \phi_0(x) &= 0 && \text{otherwise.} \end{aligned} \tag{5.27}$$

with $A_0 > 0$. An illustration for the case $a = 200$, $H = 150$ and $A_0 = 1$ is given in Fig. 5.1.

Actually, the amplitudes in the left and right cores do not necessarily need to be equal; they were here chosen to be equal for convenience. However, if there exists a homogeneous absorbing material between the two cores, the two amplitudes will be equal. So if one treats a decoupled system as a limit of a previously loosely coupled system, the choice of the symmetric amplitudes is obvious.

The interesting aspect comes when we want to determine the first harmonic solution $\phi_1(x)$ in this system. We find that a solution which is orthogonal to $\phi_0(x)$,

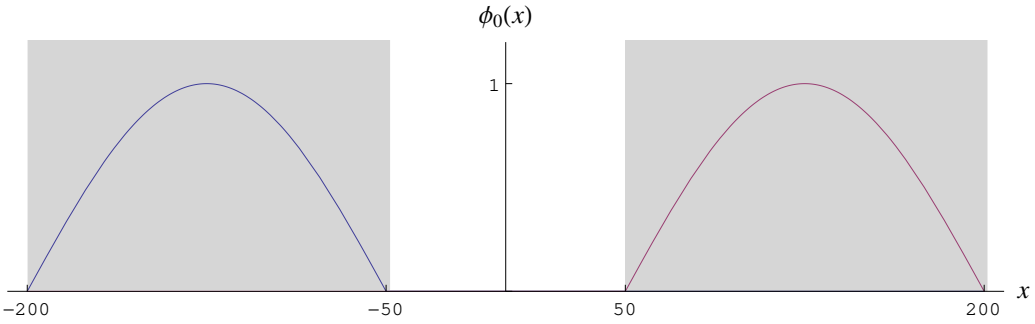

Figure 5.1: The fundamental mode $\phi_0(x)$ in the system of two decoupled cores

and hence is an independent solution, is given as

$$\begin{aligned} \phi_1(x) &= -A_1 \sin[B_0(x+a)] \quad \text{for} \quad -a < x < -a+H; \\ \phi_1(x) &= A_1 \sin[B_0(x-a+H)] \quad \text{for} \quad a-H < x < a; \\ \phi_1(x) &= 0 \quad \text{otherwise.} \end{aligned} \tag{5.28}$$

This case is illustrated in Fig. 5.2, with $A_1 = 1$.

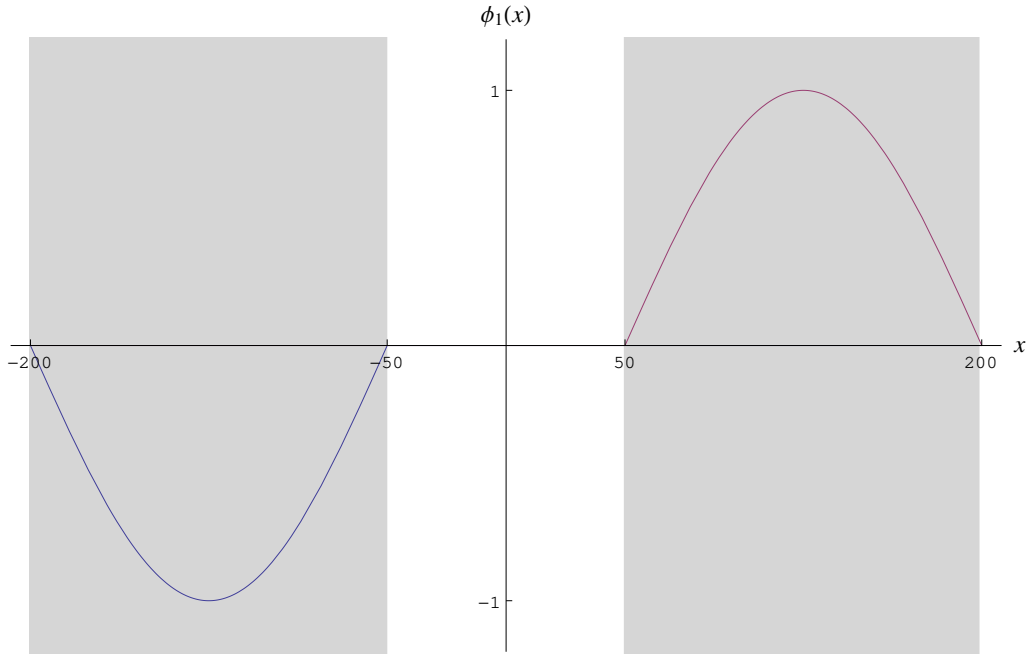

Figure 5.2: The first higher order eigenfunction $\phi_1(x)$ in the system of two decoupled cores

The fact that the buckling appearing in expression (5.28) is the same as the critical buckling B_0 yields that $k_1 = k_0 = 1$, and hence one has the case of $(E.S.) = 0$. It is also easy to confirm that for $n > 1$, one has $(E.S.)_n > 0$.

It is now straightforward to interpret how a divergent space-dependent noise arises (or the fact that point kinetic behaviour does not become dominating) in such a pathological system for $\omega \to 0$. Assume now a frequency-independent (white

noise) localised perturbation of the variable absorber type at the centre of the right hand side core[3]:

$$\delta\Sigma_a(x,\omega) = \gamma\delta(x - a + H/2) \tag{5.29}$$

The position of the perturbation is indicated with a red vertical line at $x = 125$ cm in Fig. 5.3, which shows both the fundamental mode $\phi_0(x)$ and the first harmonic $\phi_1(x)$ together. In the right hand side core, i.e. from $x = 50$ to $x = 200$ cm, $\phi_0(x)$ completely overlaps with $\phi_1(x)$. Assume now for simplicity of the reasoning equal

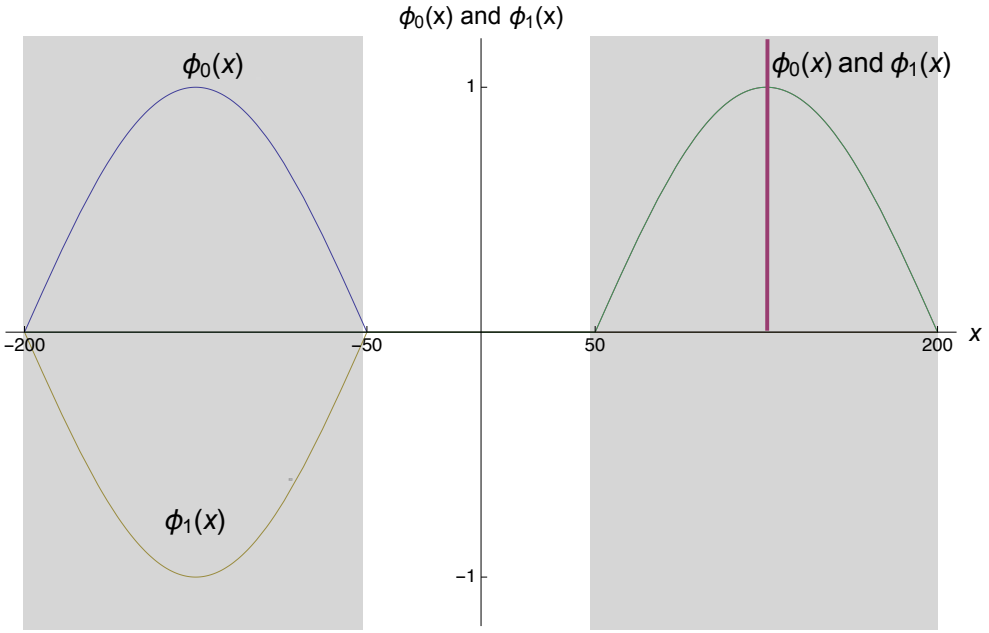

Figure 5.3: The first two lowest order eigenfunctions $\phi_0(x)$ and $\phi_1(x)$ of the decoupled system, together with the indication of a localised perturbation. In the right hand side core, $\phi_0(x)$ and $\phi_1(x)$ are identical.

amplitudes of the two eigenfunctions, i.e. $A_0 = A_1$, which corresponds to how the figure is plotted. (It can be shown that the final conclusion of the forthcoming discussion does not depend on the equality of the flux amplitudes). Then, from the perturbation formula one obtains that $\rho(\omega) = \delta\rho_1(\omega) = \text{const} \equiv \rho$. Letting now $\omega \to 0$, the last term on the right hand side (r.h.s.) of (5.23) can be neglected in comparison to the first and second terms, yielding

$$\delta\phi(x,\omega) \approx \rho\, G_0(\omega)\,[\phi_0(x) + \phi_1(x)] \tag{5.30}$$

As it is also seen in Fig. 5.3, the sum of the two eigenfunctions is zero in the left hand side slab, and is equal to $2\phi_0(x)$ in the right hand side slab. As is obvious, this behaviour is neither point kinetic, nor fully space dependent (i.e. without a point kinetic term); it has equal contributions from both the fundamental mode

[3]For a spatial Dirac-delta type perturbation, the induced noise has a discontinuous space derivative in the point of perturbation. Thus, in general, a series expansion in terms of the static unperturbed eigenfunctions is not effective, due to slow convergence. However, even for such a case, at low frequencies, all higher order modes will be negligible compared to the first two modes.

(point kinetic component) and the first higher order mode (a full space dependent component).

This is of course a somewhat artificial result which considers simultaneously two cores that are not connected. The same result could be obtained in a simpler way, by noting that if only one of two decoupled cores is perturbed, then only that core can have any response, so the fact that there will be no response in the other core, and which we derived in the foregoing as a result of the cancellation of two quantities of opposite sign, will be trivial if we treat the two cores separately. On the other hand the fact that we got the correct result, verifiable by other means, for the aggregate system, shows the correctness of the first harmonic $\phi_1(x)$, whose construction might have felt artificial. If we only consider the perturbed core, then of course the response in that core will be point kinetic at low frequencies. Even quantitatively, we obtain the same result; (5.30) will yield for the noise in "core II" (the right hand side slab) the result

$$\delta\phi(x,\omega) \approx \rho\, G_0(\omega)\, 2\sin[B_0(x-a+H)]. \tag{5.31}$$

This is the same result as what we obtain by only considering core II. For this case, one will have

$$\phi_0(x) = \sin[B_0(x-a+H)] \tag{5.32}$$

and

$$\phi_1(x) = \sin[2B_0(x-a+H)] \tag{5.33}$$

That is, $B_1 = 2B_0$, hence $k_1 \neq k_0$ and $(E.S.) \neq 0$. Therefore, the second term of Eqs (5.23) can be neglected, and (5.30) and (5.31) will hence take the form

$$\delta\phi(x,\omega) \approx \rho_{1core}\, G_0(\omega)\, \sin[B_0(x-a+H)] \tag{5.34}$$

where ρ_{1core} is the reactivity effect of the perturbation if only one core is considered. This is naturally larger than the reactivity effect in the two-core system. One has

$$\rho_{1core} = 2\,\rho \tag{5.35}$$

because

$$\int_{V_{2cores}} \phi_0^2(x)dx = 2\int_{V_{1core}} \phi_0^2(x)dx \tag{5.36}$$

(cf. also Eq. (5.21)). This shows that we get exactly the same result as when considering a system of two cores simultaneously, which shows that the results obtained from the latter are justified.

One can even go one step further and consider the aggregate effect of two perturbations, by adding another localised perturbation in the middle of core I, i.e. the left hand side one, to the previous one, Eq. (5.29) representing an absorber of variable strength, but fluctuating in opposite phase. The absorption cross section fluctuation will then have the form

$$\delta\Sigma_a(x,\omega) = -\gamma\delta(x+a-H/2) + \gamma\delta(x-a+H/2) \tag{5.37}$$

As it is also easy to see intuitively, the total reactivity effect of this perturbation is zero, i.e. $\rho(\omega) = 0$ whereas $\delta\rho_1(\omega) \neq 0$. Trivially, $\delta\rho_1(\omega)$ will be twice as big as in the previous case, when it was equal to ρ, i.e. it was equal to the reactivity effect of the perturbation when the two cores were considered as one system. So we write

$$\delta\rho_1(\omega) = 2\rho \tag{5.38}$$

where we shall remember that ρ stands for the reactivity effect of the previous perturbation. In view of the fact that the reactivity in the present case is zero, the noise can be approximated for low frequencies as

$$\delta\phi(x,\omega) \approx 2\rho\, G_0(\omega)\, \phi_1(x) \tag{5.39}$$

It is seen from (5.30) or (5.31) that the result is that in core II the response will be exactly the same as before, which is expected, since a perturbation in core I cannot influence what happens in core II. The response in core I will, on the other hand, have the same magnitude and space dependence as in core II, but oscillating in opposite phase. Considering the two cores separately, both show a point kinetic behaviour, which is expected, since as individual cores, their ES is not zero and the reactivity effect of the perturbation is not zero, hence their behaviour is point kinetic at low frequencies. Considering the two cores together, their ES is zero, the reactivity effect of the perturbation is zero, hence they show pure space dependent behaviour, with a noise amplitude which diverges for vanishing frequencies.

So far it was only demonstrated that in the case of considering two completely decoupled cores, the ES will become zero and the noise component proportional to the first higher eigenfunction will have the same asymptotic properties with vanishing frequencies as the point kinetic component in strongly coupled systems, i.e. it will diverge for $\omega \to 0$. This example may appear as artificial and only interesting conceptually. However, one can consider a case when the two cores are not completely decoupled, only very loosely coupled. This case is by no means pathological, rather it can occur in realistic cases. One such case is the old design of breeder reactors, where highly enriched concentric regions in the core were separated by fertile material. Examples are the breeder experiments ZPPR in Idaho Nat Lab [43]. Another case is the core loadings, usually in a BWR, with a control rod pattern which separates the core into loosely coupled quadrants. It is usually claimed in the literature that such a core is more prone to BWR instabilities; and in particular for regional (out-of-phase) or local instabilities [44, 45, 46].

For loosely coupled, but not completely disconnected cores, the ES will not be zero, but will be small, and hence much of the reasoning and interpretation of the previous artificial case will still hold qualitatively. For instance, the shape of the fundamental mode and the first harmonic will look like the one in Fig. 1 of Ref. [35]. Obviously, the space dependent component will not diverge for low frequencies, but can increase parallel with the point kinetic component down to quite low frequencies, preventing point kinetic behaviour even long below plateau frequencies. Another consequence of a small ES is that the amplitude of the system response to a localised perturbation with small reactivity effect can be still high

at low frequencies. If the space dependence of the perturbation is orthogonal to the fundamental mode, the first higher order harmonics will be driven with a high amplitude, which is the case in regional BWR oscillations with control rod patterns which separate the two halves of the core.

5.3 Eigenvalue separation and dynamic behaviour in a coupled core system

5.3.1 General derivation

We will now turn to the more realistic case of a one-dimensional system consisting of two multiplying cores separated with a depleted region (blanket). By changing the properties of the blanket region, one can change the system properties from strongly coupled to loosely coupled and investigate the system behaviour quantitatively. As mentioned before, in such a system both the static and the dynamic equations can be solved analytically. The static eigenfunctions and the eigenvalue separation were investigated in such systems in several works in the past [30, 31, 35, 36].

The system extrapolated boundaries will lie at x_1 and x_4, with the fuel-blanket interfaces being situated at x_2 and x_3. Hence the fuel regions are situated in (x_1, x_2) and (x_3, x_4), whereas the blanket region lies between (x_2, x_3). The two fuel regions have the same material properties. The strength of the coupling will be controlled by the absorption properties of the blanket region. The static eigenvalue equation reads as

$$D^{(i)}\frac{d^2}{dx^2}\phi_j^{(i)}(x) + \left(\frac{\nu\Sigma_f^{(i)}(x)}{k_j} - \Sigma_a^{(i)}(x)\right)\phi_j^{(i)}(x) = 0, \tag{5.40}$$

where (i) denotes the region number, i = 1,2,3, j stands for the mode number, and the coefficients are piecewise constant functions, i.e. $D^{(i)}$, $\nu\Sigma_f^{(i)}$ and $\Sigma_a^{(i)}$ are constant in each region. Vacuum boundary conditions are assumed with vanishing of the flux at the extrapolated boundaries, and continuity of the flux and the current at the interfaces between the three regions. In each region the general solution can be given in an analytical form with unknown coefficients for each eigenfunction, and the coefficients are determined from the boundary and interface conditions. The procedure is standard [47], and no details are necessary to give here.

The dynamic case will be solved in a similar manner for the Green's function of the system. The equation for the Green's function (by neglecting the notation on the region number) reads as

$$\frac{\partial^2}{\partial x^2}G(x, x', \omega) + B^2(\omega)G(x, x', \omega) = \frac{\delta(x - x')}{D}, \tag{5.41}$$

Here again, $B^2(\omega)$ and D are piecewise constant functions of space. The position x' will lie in one of the fuel regions, and we shall assume that $x_1 < x' < x_2$. An analytical solution can be obtained by designating x' as an interface point, and specifying the continuity of the Green's function and the discontinuity of its derivative, arising from the delta function r.h.s. of (5.41). General solutions in closed analytical form can be obtained for the Green's function in each region, and

the coefficients of the basic solutions can be determined from the boundary and interface solutions by a numerical inversion of the matrix equation for the frequency dependent coefficients. This procedure was employed e.g. in Ref. [47].

As is known, the Green's function $G(x, x_p, \omega)$ is proportional to the neutron noise induced by an absorber of variable strength located at the position x_p at frequency ω, hence in the continuation the Green's function will be interpreted as the neutron noise with regards to its space and frequency dependence:

$$\delta\phi(x,\omega) = c \cdot G(x, x_p, \omega) \tag{5.42}$$

with $c = \gamma\,\phi_0(x_p)$, where γ stands for the (frequency independent) amplitude of the strength variations of the absorber (assumed to have white noise character in time, i.e. having a constant frequency spectrum).

Our goal now is to derive expressions for $a_0(\omega)$ and $a_1(\omega)$, for which the obvious procedure would be to apply the expansion of the noise (Green's function) into the spatial eigenfunctions. However, this would constitute a considerably complicated task. Partly, because the determination of each individual eigenfunction is quite involved, and the solution is semi-analytical due to the numerical step in the determination of the frequency dependent coefficients of the spatial solutions in each region. Partly, because unlike for a homogeneous system, where direct (decoupled) equations for the $a_i(\omega)$ could be obtained, here an infinite system of complicated coupled equations should be solved. This could be achieved only by applying a closure condition at a high order of the eigenfunctions, i.e. replacing the infinite sum with a finite one, and solving the resulting finite set of equations, again numerically. In other words, one needs to determine all $a_i(\omega)$ up to a large value of i, even if one is only interested in the first two of these.

A more straightforward way of determining the quantities $a_0(\omega)$ and $a_1(\omega)$ is to utilise the relative ease with which the full solution can be obtained, as follows. From the full solution $\delta\phi(x,\omega)$ obtained as described above, the frequency dependent mode amplitudes $a_k(\omega)$ from the expansion (5.15), which is reproduced here for convenience as

$$\delta\phi(x,\omega) = \sum_{k=0}^{\infty} a_k(\omega)\phi_k(x), \tag{5.43}$$

can be obtained by using the orthogonality properties of the various eigenfunctions. These are readily obtained from Eq. (5.40) as

$$\int_{x_1}^{x_4} \phi_k(x)\nu\Sigma_f(x)\phi_j(x)dx = \delta_{kj}\int_{x_1}^{x_4} \phi_j^2(x)\nu\Sigma_f(x)dx. \tag{5.44}$$

Accounting for the orthogonality property, from Eq. (5.43) the fundamental and first higher order mode frequency dependent coefficients are obtained as

$$a_0(\omega) = \frac{\int_{x_1}^{x_4} \delta\phi(x,\omega)\nu\Sigma_f(x)\phi_0(x)dx}{\int_{x_1}^{x_4} \phi_0^2(x)\nu\Sigma_f(x)dx}, \tag{5.45}$$

$$a_1(\omega) = \frac{\int_{x_1}^{x_4} \delta\phi(x,\omega)\nu\Sigma_f(x)\phi_1(x)dx}{\int_{x_1}^{x_4} \phi_1^2(x)\nu\Sigma_f(x)dx}. \tag{5.46}$$

.

The behaviour of the coefficients $a_0(\omega)$ and $a_1(\omega)$ will be investigated quantitatively in the next Section.

5.3.2 Quantitative analysis

Quantitative studies were performed on three different systems with different coupling properties of the blanket region with the parameters given in Tables 5.1 and 5.2. Table 5.2 shows the parameters for the different blanket regions and also the corresponding values of the eigenvalue separation. In the loosely coupled system the $(E.S.)$ is significantly lower than in the other two systems.

Table 5.1: Parameters for the reference system (given for each spatial reactor region separately).

Parameter	Value used
$a\ [cm]$	180
$H = 2a\ [cm]$	360
$x_1 = -a\ [cm]$	-180
$x_2\ [cm]$	-60
$x_3\ [cm]$	60
$x_4 = a\ [cm]$	180
$\Sigma^0_{tr1}\ [cm^{-1}]$	0.15
$\Sigma^0_{tr2}\ [cm^{-1}]$	0.15
$\Sigma^0_{tr3}\ [cm^{-1}]$	0.15
$D^0_1\ [cm]$	$\frac{1}{3\Sigma^0_{tr1}}$
$D^0_2\ [cm]$	$\frac{1}{3\Sigma^0_{tr2}}$
$D^0_3\ [cm]$	$\frac{1}{3\Sigma^0_{tr3}}$
$\Sigma^0_{a,1}\ [cm^{-1}]$	0.01
$\Sigma^0_{a,2}\ [cm^{-1}]$	0.0005
$\Sigma^0_{a,3}\ [cm^{-1}]$	0.01
k_∞	1.01
$\nu\Sigma^0_{f,1}\ [cm^{-1}]$	$\Sigma_{a,1} \cdot k_\infty$
$\nu\Sigma^0_{f,2}\ [cm^{-1}]$	0
$\nu\Sigma^0_{f,3}\ [cm^{-1}]$	$\Sigma_{a,3} \cdot k_\infty$
$\lambda_1\ [s^{-1}]$	0.1
$\lambda_3\ [s^{-1}]$	0.1
β_1	0.0065
β_3	0.0065
$v_1\ [cm/s]$	$1.755 \cdot 10^7$
$v_2\ [cm/s]$	$1.755 \cdot 10^7$
$v_3\ [cm/s]$	$1.755 \cdot 10^7$

The space dependence of the static fluxes, showing the fundamental mode and the first higher order mode is shown in Fig. 5.4 for the three systems, starting with the loosely coupled system on to the strongly coupled system. These figures are in

correspondence with similar results such as those in [30, 31, 35, 36].

Table 5.2: Parameters for the systems with different coupling properties.

Parameter	Loosely-coupled system	Reference system	Strongly-coupled system
$\Sigma^0_{a,2}$ $[cm^{-1}]$	$6 \cdot 10^{-3}$	$5 \cdot 10^{-4}$	$5 \cdot 10^{-5}$
$k_0 = k_{eff}$	0.90597	0.945	0.969
k_1	0.90580	0.928	0.934
$[E.S.]_0$	0	0	0
$[E.S.]_1$	0.00021	0.0193	0.0387

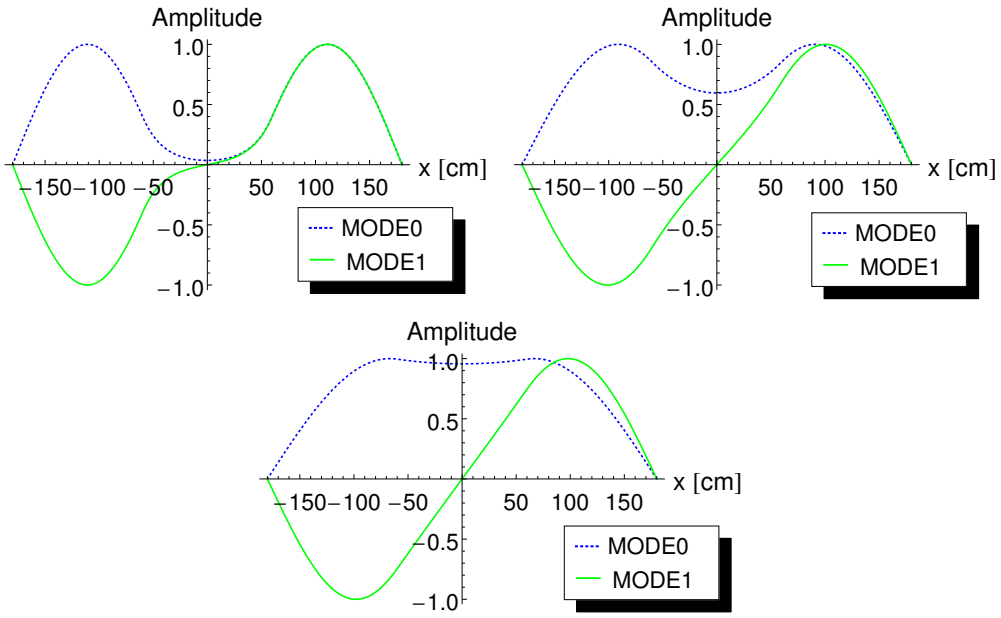

Figure 5.4: Space dependence of the fundamental and first modes for the systems with various coupling properties (obtained by modifying $\Sigma_{a,2}$ in the second reactor region): loosely-coupled (upper left figure), reference (upper right figure) and strongly coupled (bottom figure).

The frequency dependence of the corresponding modes is shown in Fig. 5.5. The figure shows that, as expected, the amplitude of the fundamental mode, which is equal to the point kinetic component, diverges with decreasing frequencies. The behaviour of this mode is the same for all three systems. This is the generic behaviour in all critical systems subjected to a perturbation with a non-zero reactivity effect.

The behaviour of the first higher mode, on the other hand, is quite different in the loosely coupled system from that in the other two systems. In the reference and the strongly coupled systems, its amplitude is basically constant below the plateau frequency, having essentially the same value as at the plateau frequencies. In these systems, therefore, point kinetic behaviour is established quickly below the plateau frequency (in the strongly coupled system, actually the point kinetic component dominates even at plateau frequencies). For the loosely coupled system, on the

other hand, the amplitude of the first mode shows the same increasing trend with decreasing frequency as the point reactor component over two orders of magnitude of the frequency below the plateau. In other words, such a system remains deeply space dependent, with the first mode having comparable amplitude to that of the fundamental mode. Choosing an asymmetric perturbation with much smaller reactivity effect would even lead to the dominance of the first mode in such a system down to rather low frequencies.

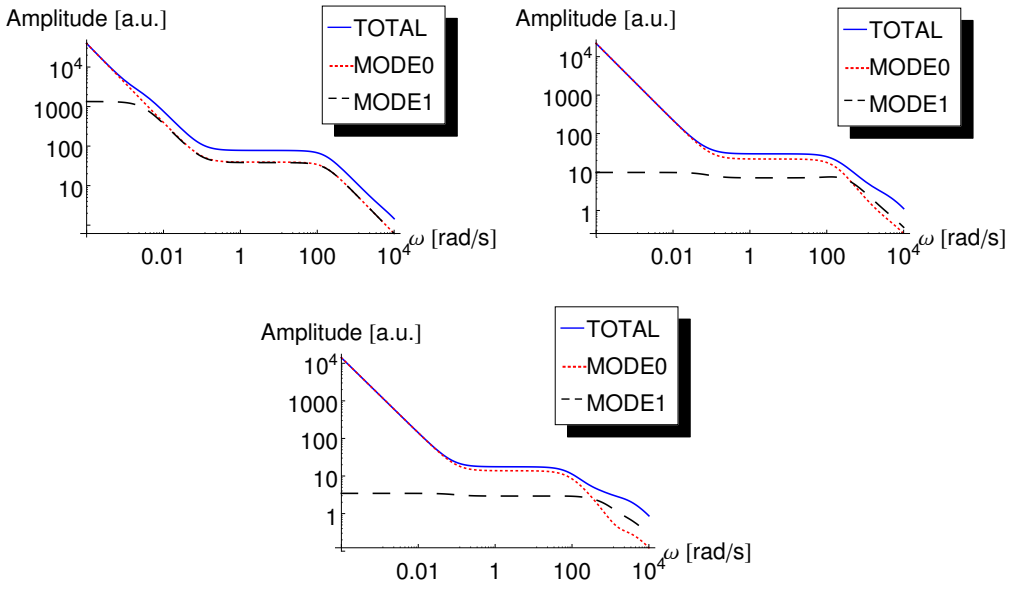

Figure 5.5: Frequency dependence of the amplitude of the fundamental and first mode components of the neutron noise for the systems with different coupling properties: loosely-coupled (upper left figure), reference (upper right figure) and strongly coupled (bottom figure) ($x = -120$ cm, $x_p = -150$ cm).

It is also seen from the figures that the fundamental and first mode together make up for the total noise, hence the contribution from the higher order modes is negligible. Thus it is seen that in a system with two loosely coupled cores, the response essentially consists of the first two modes, and the contribution of the first higher order mode to the system response is significant down to very low frequencies.

5.4 Conclusions

The simple considerations offered in this study serve to illuminate the role of the eigenvalue separation in reactor dynamics and neutron noise theory. Through a simple example, it was shown how in a system of loosely coupled cores the smallness of the eigenvalue separation enhances the weight of the first higher order mode in the system response which prevents the dominance of point kinetic behaviour down to very low frequencies. These considerations are in agreement with, and hence serve as confirmation of the origin and the characteristics of regional oscillations in a BWR.

6. FURTHER INVESTIGATIONS OF THE POSSIBILITIES OF USING FISSION CHAMBER SIGNALS FOR MEASUREMENT OF SUBCRITICAL REACTIVITY, SUCH AS ELABORATION OF THE EQUIVALENT OF THE FEYNMAN-ALPHA METHOD OF PULSE COUNTING, AND ACCOUNTING FOR DELAYED NEUTRONS

In zero power noise experiments, such as the determination of subcritical reactivity under start-up, the subcritical reactivity is determined from the statistics of the number of individual counts. Two methods utilising this technique are the Rossi-alpha method (temporal correlations) and the Feynman-alpha method (the relative variance of the number of detection as a function of the measurement time). From the temporal correlations, or the dependence of the variance to mean on the measurement time, the prompt neutron decay constant, and from that the subcritical reactivity, can be determined.

These methods encounter difficulties at high count rates, due to dead-time problems. This could be circumvented by the use of fission chambers in the current mode. However, this requires the elaboration and test of a method for extracting the same information from the statistics of the continuous detector current of fission chambers as from the pulse counting methods.

In the previous Stage, we managed to generalise the theory of fission chamber currents to make it possible to extract the time correlations from the detector current. It was shown that the prompt neutron decay constant can be extracted from the auto-covariance of the detector current, although the procedure is more complicated than in the case of pulse counting, since the decay constant of the detector pulse also appears in the formulae. These calculations were made in a model with only prompt neutrons. In the present Stage, the theory was extended to include also the current mode equivalent of the Feynman-alpha method (variance to mean). The work was performed in two steps. First, the results were derived by neglecting the delayed neutrons. This work will be presented in some detail in this Chapter. The conditions, under which the prompt neutron decay constant can be distinguished from the detector pulse decay constant, were also identified. Hence the possibilities of performing some experimental study, or verification of the method, can also be investigated in the continuation. These results are based on Ref. [48]. Details of the calculations are found there. Here, only the main results are summarised.

In the next step, the calculations were extended to the case when delayed neutrons are also accounted for. This work was performed by our visiting scientist, Yasunori Kitamura. The calculations are very involved, and they confirm the fact, known from the traditional Feynman-alpha theory, that the results obtained by neglecting the delayed neutrons can be applied with some modifications to the prompt part of the signal, to evaluate measurements where obviously delayed neutrons are involved. Hence these calculations will not be included here, we only refer to the

journal paper in which the results are published [49].

6.1 Reformulation of the previous results for the covariance

Derivation of the current-based theory of the Feynman-alpha method will require the use of the covariance of the detector signal, hence we start with a re-capitulation of the previous results. In the previous Stage, based on the results of [50], an expression for the autocovariance of the detector signal was derived (Eq. 7.64) for the case when the detector pulse distibution $\varphi(\boldsymbol{x}, t)$ had the form

$$\varphi(\boldsymbol{x}, t) = Q\boldsymbol{x}^2 t \mathrm{e}^{-\boldsymbol{x}t}, \quad 0 \leq t < +\infty, \tag{6.1}$$

$$w(x) = \delta(x - \alpha_\mathrm{e}), \quad \alpha_\mathrm{e} \neq \alpha. \tag{6.2}$$

Here, α_e is the time constant of the neutron detector system, and Q the amplitude factor, which is related to the collected charge.

In this report, following the notations of [48], we first re-write this formula. Introducing the notations

$$\Phi = \frac{\lambda_\mathrm{d}\lambda_\mathrm{f} Q \langle \nu(\nu - 1) \rangle \alpha_\mathrm{e}^4}{\alpha^2 \left(\alpha_\mathrm{e}^2 - \alpha^2\right)^2}, \tag{6.3}$$

$$\Psi_1 = -\frac{\alpha^2 \left(3\alpha_\mathrm{e}^2 - \alpha^2\right)}{2\alpha_\mathrm{e}^4}\Phi + \frac{Q}{2}, \tag{6.4}$$

$$\Psi_2 = -\frac{\alpha^2 \left(\alpha_\mathrm{e}^2 - \alpha^2\right)}{2\alpha_\mathrm{e}^4}\Phi + \frac{Q}{2}, \tag{6.5}$$

the auto-covariance function $\mathrm{cov}(\tau)$ can be written in the form

$$\begin{aligned} \mathrm{cov}(\tau) &= \mathrm{acf}(\tau) - \langle \eta_1 \rangle^2 \\ &= \frac{1}{2}\alpha \langle \eta_1 \rangle \Phi \mathrm{e}^{-\alpha|\tau|} + \frac{1}{2}\alpha_\mathrm{e} \langle \eta_1 \rangle \Psi_1 \mathrm{e}^{-\alpha_\mathrm{e}|\tau|} + \frac{1}{2}\alpha_\mathrm{e} \langle \eta_1 \rangle \Psi_2 \alpha_\mathrm{e} |\tau| \mathrm{e}^{-\alpha_\mathrm{e}|\tau|}. \end{aligned} \tag{6.6}$$

where $\langle \eta_1 \rangle$ stands for the expectation (first moment) of the detector current. It is this form which we will use for the application of the variance to mean technique with the continuous detector signals.

6.2 Variance to mean function technique

In this technique, one uses the mean and the variance of the integral value of continuous neutron detection current signal, in the hope that it will contain the prompt neutron decay constant in a form that makes it possible to unfold it from the expression, similarly to the case of the traditional discrete pulse counting. Hence, one defines the random variable

$$A(T) = \int_0^T \mathrm{d}t \; y(t), \tag{6.7}$$

where $y\,(t)$ is the neutron detector current signal at time t, and T is the integration time interval. Then, the variance to mean method is given by the formula

$$\frac{\sigma_A^2(T)}{\langle A\,(T)\rangle} = \frac{\langle A^2\,(T)\rangle - \langle A\,(T)\rangle^2}{\langle A\,(T)\rangle}, \tag{6.8}$$

The practical determination of the variance to mean is made similarly to the traditional pulse counting method, i.e. the random variable $A(T)$ is repeatedly measured for a given value of T, and the mean and the variance are estimated from these measured values. Repeating the procedure by varying the measurement time T, the variance to mean ratio as a function of the integration time interval is obtained. Hence, hereafter this technique is referred to as the variance-to-mean function technique.

One would recognize a similarity of the variance-to-mean function technique to the traditional Feynman-alpha one [51, 52], as well as to that of the auto-covariance function one to the traditional Rossi-alpha one [53]. At the same time, this recognition recalls an expectation that the variance-to-mean function technique would have the same type of advantage over the auto-covariance function technique with regard to the statistics.

As is known [54], the expectation and the variance of the integral $A\,(T)$ are expressed as follows:

$$\langle A\,(T)\rangle = E\left[A\,(T)\right] = \int_0^T \mathrm{d}t\ E\left[y\,(t)\right], \tag{6.9}$$

and

$$\sigma_A^2\,(T) = E\left[A^2\,(T)\right] - E\left(\left[A\,(T)\right]\right)^2 = \int_0^T \mathrm{d}t_1 \int_0^T \mathrm{d}t_2\ \mathrm{cov}(t_1, t_2). \tag{6.10}$$

Since

$$E\left[y\,(t)\right] = \langle \eta_1 \rangle, \tag{6.11}$$

the mean and the variance are derived as

$$\langle A\,(T)\rangle = \int_0^T \mathrm{d}t\ \langle \eta_1 \rangle = \langle \eta_1 \rangle\, T, \tag{6.12}$$

$$
\begin{aligned}
\sigma_A^2(T) &= \int_0^T \mathrm{d}t_1 \int_0^T \mathrm{d}t_2 \ \mathrm{cov}\,(t_2 - t_1) \\
&= \frac{1}{2}\alpha \langle \eta_1 \rangle \Phi \left\{ \int_0^T \mathrm{d}t_1 \int_{t_1}^T \mathrm{d}t_2 \ \mathrm{e}^{-\alpha(t_2-t_1)} + \int_0^T \mathrm{d}t_2 \int_{t_2}^T \mathrm{d}t_1 \ \mathrm{e}^{-\alpha(t_1-t_2)} \right\} \\
&\quad + \frac{1}{2}\alpha_\mathrm{e} \langle \eta_1 \rangle \Psi_1 \left\{ \int_0^T \mathrm{d}t_1 \int_{t_1}^T \mathrm{d}t_2 \ \mathrm{e}^{-\alpha_\mathrm{e}(t_2-t_1)} + \int_0^T \mathrm{d}t_2 \int_{t_2}^T \mathrm{d}t_1 \ \mathrm{e}^{-\alpha_\mathrm{e}(t_1-t_2)} \right\} \\
&\quad + \frac{1}{2}\alpha_\mathrm{e} \langle \eta_1 \rangle \Psi_2 \left\{ \begin{array}{l} \displaystyle\int_0^T \mathrm{d}t_1 \int_{t_1}^T \mathrm{d}t_2 \ \alpha_\mathrm{e}\,(t_2 - t_1)\,\mathrm{e}^{-\alpha_\mathrm{e}(t_2-t_1)} \\ \qquad \displaystyle + \int_0^T \mathrm{d}t_2 \int_{t_2}^T \mathrm{d}t_1 \ \alpha_\mathrm{e}\,(t_1 - t_2)\,\mathrm{e}^{-\alpha_\mathrm{e}(t_1-t_2)} \end{array} \right\} \\
&= \langle A(T) \rangle \left\{ \Phi f_1(\alpha T) + \Psi_1 f_1(\alpha_\mathrm{e} T) + \Psi_2 f_2(\alpha_\mathrm{e} T) \right\}.
\end{aligned}
\tag{6.13}
$$

Here the functions appearing in the final form of $\sigma_A^2(T)$ are defined as

$$
f_1(\chi) = 1 - \frac{1 - \mathrm{e}^{-\chi}}{\chi} \tag{6.14}
$$

and

$$
f_2(\chi) = 1 + \mathrm{e}^{-\chi} - 2\frac{1 - \mathrm{e}^{-\chi}}{\chi}. \tag{6.15}
$$

Finally, by substituting Eqs. (6.12) and (6.13) into Eq. (6.8), the theoretical formula for the variance to mean is derived as follows:

$$
\frac{\sigma_A^2(T)}{\langle A(T) \rangle} \equiv \mathrm{vtm}(T) = \Phi f_1(\alpha T) + \Psi_1 f_1(\alpha_\mathrm{e} T) + \Psi_2 f_2(\alpha_\mathrm{e} T). \tag{6.16}
$$

where the abbreviation $\mathrm{vtm}(T)$ was introduced for the variance to mean, which will be used in the next subsection, to simplify notations.

In the variance to mean function technique, the integral value of continuous neutron detection current signals is to be measured. Such measurement can be made by a special analogue circuit that integrates continuous current signals. A commercially available fast ADC equipment that acquires digital waveforms would also be useful with the trapezoid rule procedure shown in Appendix A of Ref. [48].

One also notices that the functional form of the first two terms of the variance to mean in Eq. (6.16) are identical with the $Y(T)$ function of the traditional pulse counting method, where (accounting only for prompt neutrons, like in the present work), the variance to mean of the discrete detector counts Z during a measurement interval is given as

$$
\frac{\sigma_Z^2(T)}{\langle Z(T) \rangle} = 1 + Y(T) \tag{6.17}
$$

with $Y(T) = f_1(\alpha\, T)$. At the same time, one notes that the variance to mean of the discrete pulse counting method starts from unity for small values of T, whereas the variance to mean of Eq. (6.16) starts from zero.

The reason for this difference is that $A(T)$ is the integral of a *continuous* random variable, whereas $Z(T)$ is the sum of a continuous parametric *discrete* process. For the former, the variance is expressed by (6.10), whereas for the latter one has

$$\sigma_Z^2\left(T\right) = \left\langle Z\left(T\right)\right\rangle + \int_0^T \mathrm{d}t_1 \int_0^T \mathrm{d}t_2 \ \mathrm{cov}(t_1, t_2). \tag{6.18}$$

A derivation of (6.18), where the continuous parametric discrete random variable is the neutron number as a function of the phase space variables, is found e.g. in [55] and [56].

From the comparison of (6.10) and (6.18), it is now easy to interpret the differences between the variance to mean of the detector current, Eq. (6.16), and that of the pulse counting method, Eq. (6.17). The appearance of the expectation $\langle Z\rangle$ on the r.h.s. of (6.18), which is the reason of the appearance of the unity on the r.h.s. of (6.17), is due to the fact that for infinitesimally small times $\Delta(T)$, for $Z \geq 1$, one has

$$P_Z(\Delta T) \propto \ \delta_{Z,1}\, \Delta T + o((\Delta T)^2). \tag{6.19}$$

Hence, in first order of ΔT, one has $\langle Z\rangle = \langle Z^2\rangle$, whereas $\langle Z\rangle^2$ is second order of ΔT, and thus $\sigma_Z^2(\Delta T) = \langle Z(\Delta T)\rangle$. In other words, the variance and the mean both tend to zero linearly, and with the same linearity coefficient, when ΔT goes to zero. In contrast, the variance of the integral of the continuous random variable tends to zero faster than the mean when the integration interval ΔT goes to zero. This explains the difference what regards the expressions for small measurement intervals.

On the other hand, the similarity between (6.16) and the second term of (6.17) is due to the similarities of the corresponding covariance functions. The covariance function of the discrete detector counts, as given by the Rossi-alpha formula, has the same $e^{-\alpha|\tau|}$ form as the first two terms on the r.h.s. of (6.6), hence the integrals of the covariance functions will also be of the same functional form. The third term on the r.h.s. of (6.6) is of a different form, this is the reason of the appearance of the term proportional to $f_2(\alpha_e T)$ in Eq. (6.17).

It is also seen, that in the traditional Feymnan-alpha formula of pulse counting, the information about the prompt neutron decay constant is in the function $Y(T)$, i.e. in the deviation of the variance to mean from unity, which can be much smaller than unity if the detector efficiency is small; whereas in the present method, based on the continuous current of the detector, the whole variance to mean function is the information career. At least in principle, this might lend some advantage in the practical applications.

6.3 Experimental conditions for the time-domain techniques

In this subsection, with regard to the auto-covariance and the variance to mean function techniques, the experimental conditions under which they can be successfully applied to subcriticality measurements will be discussed.

For convenience, the respective terms in the right hand side of Eq. (6.6) are

separately defined as follows:

$$\mathrm{cov}_1(\tau) = \frac{1}{2}\alpha \langle \eta_1 \rangle \Phi \mathrm{e}^{-\alpha|\tau|}, \tag{6.20}$$

$$\mathrm{cov}_2(\tau) = \frac{1}{2}\alpha_\mathrm{e} \langle \eta_1 \rangle \Psi_1 \mathrm{e}^{-\alpha_\mathrm{e}|\tau|}, \tag{6.21}$$

$$\mathrm{cov}_3(\tau) = \frac{1}{2}\alpha_\mathrm{e} \langle \eta_1 \rangle \Psi_2 \alpha_\mathrm{e} |\tau| \, \mathrm{e}^{-\alpha_\mathrm{e}|\tau|}. \tag{6.22}$$

Similarly, the respective terms on the right hand side of Eq. (6.16) are defined as follows:

$$\mathrm{vtm}_1(T) = \Phi f_1(\alpha T), \tag{6.23}$$

$$\mathrm{vtm}_2(T) = \Psi_1 f_1(\alpha_\mathrm{e} T), \tag{6.24}$$

$$\mathrm{vtm}_3(T) = \Psi_2 f_2(\alpha_\mathrm{e} T). \tag{6.25}$$

In Figs. 9 and 10, comparisons of the time dependences of the respective terms of the auto-covariance and the variance-to-mean functions are plotted with respect to various ratios ε of the detector pulse decay constant α_e and the prompt neutron decay constant α, i.e.

$$\varepsilon = \frac{\alpha_e}{\alpha}. \tag{6.26}$$

The coloured lines in Fig. 9 are defined as follows:

$$\begin{cases} \dfrac{|\mathrm{cov}_1(\tau)|}{\max\{|\mathrm{cov}_1(\tau)|\}} = \left|\dfrac{\mathrm{cov}_1(\tau)}{\mathrm{cov}_1(0)}\right| = \mathrm{e}^{-\alpha|\tau|}, & \text{Red line,} \\ \dfrac{|\mathrm{cov}_2(\tau)|}{\max\{|\mathrm{cov}_2(\tau)|\}} = \left|\dfrac{\mathrm{cov}_2(\tau)}{\mathrm{cov}_2(0)}\right| = \mathrm{e}^{-\alpha_\mathrm{e}|\tau|}, & \text{Blue line,} \\ \dfrac{|\mathrm{cov}_3(\tau)|}{\max\{|\mathrm{cov}_3(\tau)|\}} = \left|\dfrac{\mathrm{cov}_3(\tau)}{\mathrm{cov}_3(\alpha_\mathrm{e}^{-1})}\right| = \alpha_\mathrm{e}|\tau| \, \mathrm{e}^{1-\alpha_\mathrm{e}|\tau|}, & \text{Green line.} \end{cases} \tag{6.27}$$

With regard to Fig. 10, these are defined as follows:

$$\begin{cases} \dfrac{|\mathrm{vtm}_1(T)|}{\max\{|\mathrm{vtm}_1(T)|\}} = \left|\dfrac{\mathrm{vtm}_1(T)}{\mathrm{vtm}_1(+\infty)}\right| = f_1(\alpha T), & \text{Red line,} \\ \dfrac{|\mathrm{vtm}_2(T)|}{\max\{|\mathrm{vtm}_2(T)|\}} = \left|\dfrac{\mathrm{vtm}_2(T)}{\mathrm{vtm}_2(+\infty)}\right| = f_1(\alpha_\mathrm{e} T), & \text{Blue line,} \\ \dfrac{|\mathrm{vtm}_3(T)|}{\max\{|\mathrm{vtm}_3(T)|\}} = \left|\dfrac{\mathrm{vtm}_3(T)}{\mathrm{vtm}_3(+\infty)}\right| = f_2(\alpha_\mathrm{e} T), & \text{Green line.} \end{cases} \tag{6.28}$$

On the other hand, comparisons of the absolute amplitudes of the respective terms of the auto-covariance and the variance-to-mean functions are plotted in Figs. 11 and 12, respectively. The coloured lines in Fig. 11 are defined as follows:

$$\begin{cases} \dfrac{\max\{|\mathrm{cov}_1(\tau)|\}}{\max\{|\mathrm{cov}_1(\tau)|\}} = \left|\dfrac{\mathrm{cov}_1(0)}{\mathrm{cov}_1(0)}\right| = 1, & \text{Red line,} \\ \dfrac{\max\{|\mathrm{cov}_2(\tau)|\}}{\max\{|\mathrm{cov}_1(\tau)|\}} = \left|\dfrac{\mathrm{cov}_2(0)}{\mathrm{cov}_1(0)}\right|, & \text{Blue line,} \\ \dfrac{\max\{|\mathrm{cov}_3(\tau)|\}}{\max\{|\mathrm{cov}_1(\tau)|\}} = \left|\dfrac{\mathrm{cov}_3(\alpha_\mathrm{e}^{-1})}{\mathrm{cov}_1(0)}\right|, & \text{Green line.} \end{cases} \tag{6.29}$$

With regard to Fig. 12, these are defined as follows:

$$\begin{cases} \dfrac{\max\{|\mathrm{vtm}_1(T)|\}}{\max\{|\mathrm{vtm}_1(T)|\}} = \left|\dfrac{\mathrm{vtm}_1(+\infty)}{\mathrm{vtm}_1(+\infty)}\right| = 1, & \text{Red line,} \\ \dfrac{\max\{|\mathrm{vtm}_2(T)|\}}{\max\{|\mathrm{vtm}_1(T)|\}} = \left|\dfrac{\mathrm{vtm}_2(+\infty)}{\mathrm{vtm}_1(+\infty)}\right|, & \text{Blue line,} \\ \dfrac{\max\{|\mathrm{vtm}_3(T)|\}}{\max\{|\mathrm{vtm}_1(T)|\}} = \left|\dfrac{\mathrm{vtm}_3(+\infty)}{\mathrm{vtm}_1(+\infty)}\right|, & \text{Green line.} \end{cases} \tag{6.30}$$

The parameters that were used in calculating the quantitative values plotted in Figs. 9 – 12 are listed in Table 1.

When one determines the prompt neutron decay constant α by the auto-covariance function technique, one has to extract $\mathrm{cov}_1(\tau)$ from the total auto-covariance function $\mathrm{cov}(\tau)$. When α_e is close to α, one immediately recognizes from Fig. 9 that the range of τ on which $\mathrm{cov}_1(\tau)$ shows a strong dependence on τ coincides with the range in which the remaining terms also have their strong dependence.

Therefore, it is hard to extract $\mathrm{cov}_1(\tau)$ from total $\mathrm{cov}(\tau)$ when α_e is close to α. When α_e is much smaller than α, one sees from Fig. 9 that $\mathrm{cov}_2(\tau)$ and $\mathrm{cov}_3(\tau)$ do not show a marked dependence on τ. It hence seems that $\mathrm{cov}_1(\tau)$ could be easily distinguished from the remaining terms under such conditions. However, according to Fig. 11, the amplitudes of $\mathrm{cov}_2(\tau)$ and $\mathrm{cov}_3(\tau)$ are much larger than that of $\mathrm{cov}_1(\tau)$ when α_e is much smaller than α. Therefore, as a result, it is hard to extract $\mathrm{cov}_1(\tau)$ because $\mathrm{cov}_1(\tau)$ is buried to the remaining terms. On the other hand, when α_e is much larger than α, one understands from Fig. 11 that the amplitudes of $\mathrm{cov}_2(\tau)$ and $\mathrm{cov}_3(\tau)$ are not much larger than that of $\mathrm{cov}_1(\tau)$. Furthermore, from Fig. 9, one finds that $\mathrm{cov}_2(\tau)$ and $\mathrm{cov}_3(\tau)$ disappear much faster than $\mathrm{cov}_1(\tau)$. Therefore, it is expected that the neutron decay constant can be determined by the following simplified formula of the auto-covariance function under such a condition:

$$\mathrm{cov}(\tau) \simeq \frac{1}{2}\alpha\langle\eta_1\rangle\Phi\mathrm{e}^{-\alpha|\tau|}, \quad \alpha_\mathrm{e} \gg \alpha, \quad \text{excluding } \tau \simeq 0. \tag{6.31}$$

When one determines the neutron decay constant α by the variance-to-mean function technique, one has to extract $\mathrm{vtm}_1(T)$ from the total variance-to-mean

function $\mathrm{vtm}\,(T)$. When α_e is close to α, one immediately recognizes from Fig. 10 that the range of T on which $\mathrm{vtm}_1\,(T)$ shows a strong dependence on T is overlapped with those on which the remaining terms show their strong dependence. Therefore, it is hard to extract $\mathrm{vtm}_1\,(T)$ from the total variance to mean when α_e is close to α. When α_e is much smaller than α, one sees from Fig. 10 that $\mathrm{vtm}_2\,(T)$ and $\mathrm{vtm}_3\,(T)$ do not show a strong dependence on τ. It hence seems that $\mathrm{vtm}_1\,(T)$ could be easily distinguished from the remaining terms. However, according to Fig. 12, the amplitudes of $\mathrm{vtm}_2\,(T)$ and $\mathrm{vtm}_3\,(T)$ are much larger than that of $\mathrm{vtm}_1\,(T)$ when α_e is much smaller than α. Therefore, again, it is hard to extract $\mathrm{vtm}_1\,(T)$ because $\mathrm{vtm}_1\,(T)$ is buried to the remaining terms. On the other hand, when α_e is much larger than α, one understands from Fig. 12 that the amplitudes of $\mathrm{vtm}_2\,(T)$ and $\mathrm{vtm}_3\,(T)$ are smaller than that of $\mathrm{vtm}_1\,(T)$. Furthermore, from Fig. 10, one finds that $\mathrm{vtm}_2\,(T)$ and $\mathrm{vtm}_3\,(T)$ saturate much faster than $\mathrm{vtm}_1\,(T)$. Therefore, it is expected that the neutron decay constant can be determined by the following simplified formula of the variance-to-mean function under such a condition:

$$\mathrm{vtm}\,(T) \simeq \Phi f_1\,(\alpha T) + \Psi_0, \quad \alpha_\mathrm{e} \gg \alpha, \quad \text{excluding } T \simeq 0, \tag{6.32}$$

where

$$\Psi_0 = \Psi_1 + \Psi_2. \tag{6.33}$$

6.4 Accounting for delayed neutrons

The calculations were extended to the case when delayed neutrons are also accounted for. Although the extension is rather straightforward conceptually, the actual calculations get even more involved than before, and exceedingly lengthy. The work was performed by our visiting scientist, Yasunori Kitamura, by using the symbolic computation code Mathematica. The final results of the extensive and complicated calculations confirm the fact that, similarly to the traditional Feynman-alpha theory, the results obtained by neglecting the delayed neutrons can be applied with some modifications to the prompt part of the signal, to evaluate measurements where obviously delayed neutrons are involved. In particular, the result for the variance to mean can be written in a form similar to Eq. (6.16), with the only difference that the former $\alpha = \rho/\Lambda$ has to be replaced with $(\rho - \beta)/\Lambda$, and the definition of the coefficients Φ and Ψ_i, $i = 1, 2$, changes. However, this latter fact does not have any effect on how the prompt neutron decay constant α is evaluated from the measurements by curve fitting. Hence these calculations will not be included here, we only refer to the journal paper in which the results are published [49].

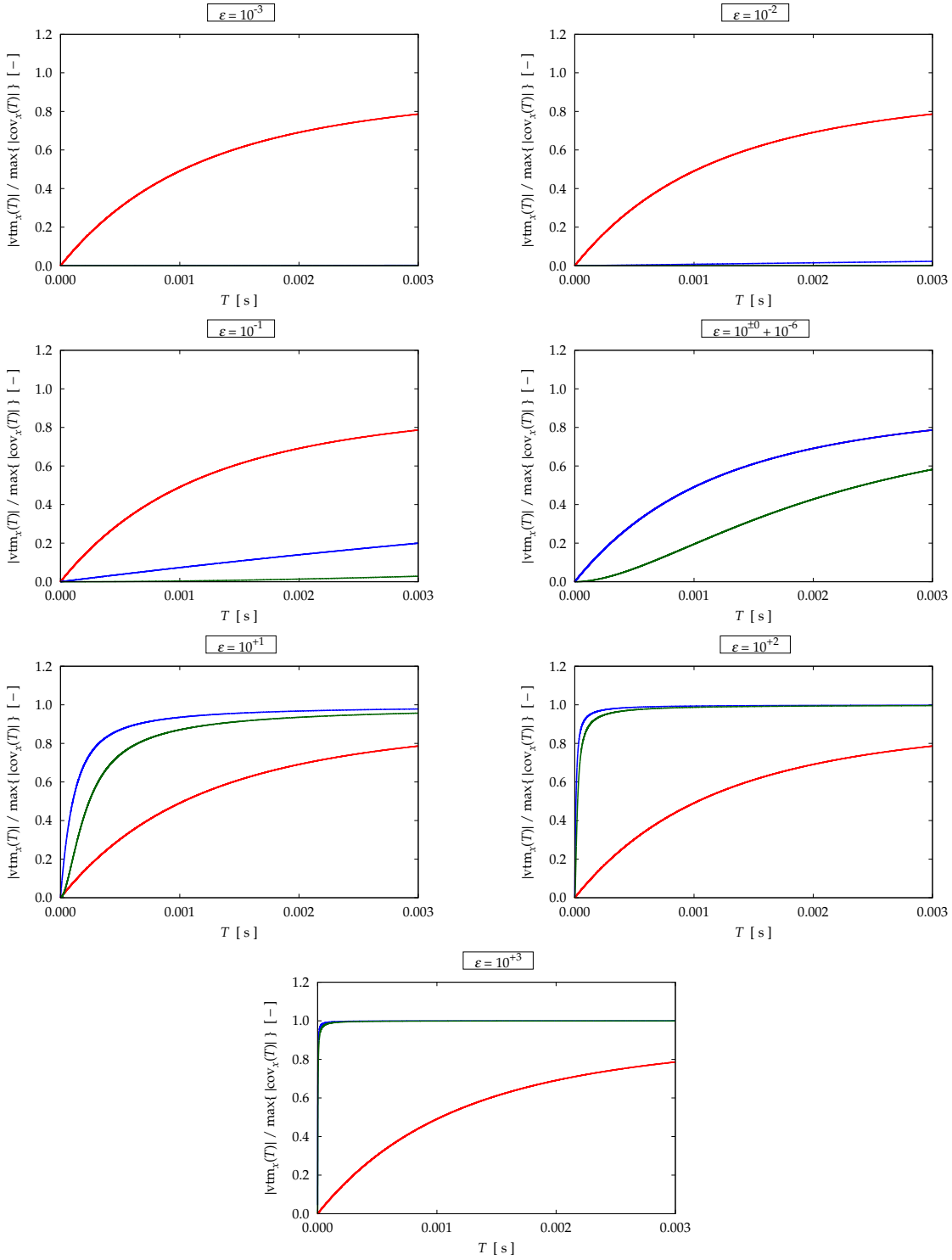

Figure 6.2: Comparisons of time dependences of respective terms in variance to mean — the red, the blue, and the green lines stand for the 1st, the 2nd, and the 3rd terms, respectively.

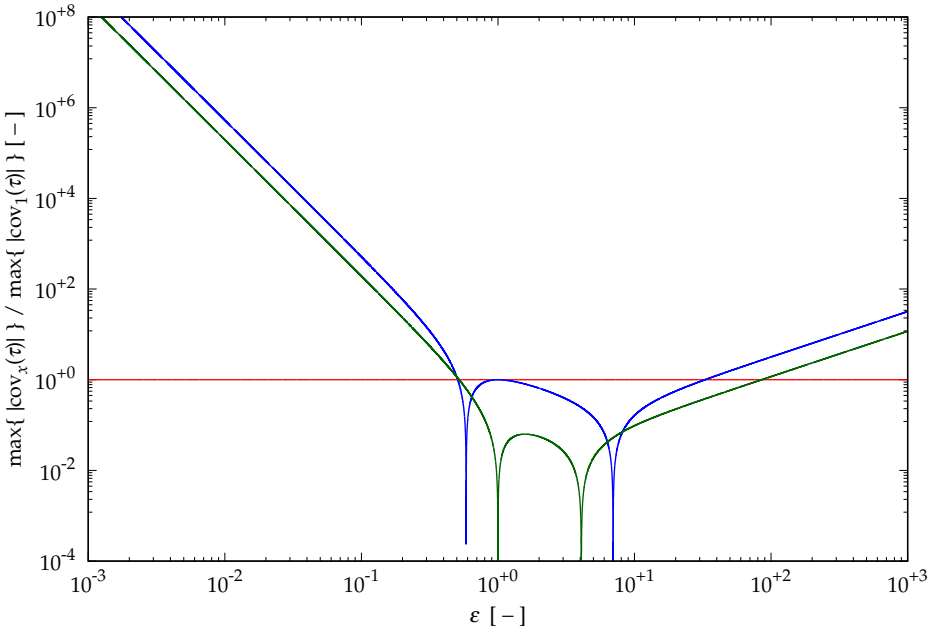

Figure 6.3: Comparison of absolute amplitudes of respective terms in cov (τ) — the red, the blue, and the green lines stand for the 1st, the 2nd, and the 3rd terms, respectively.

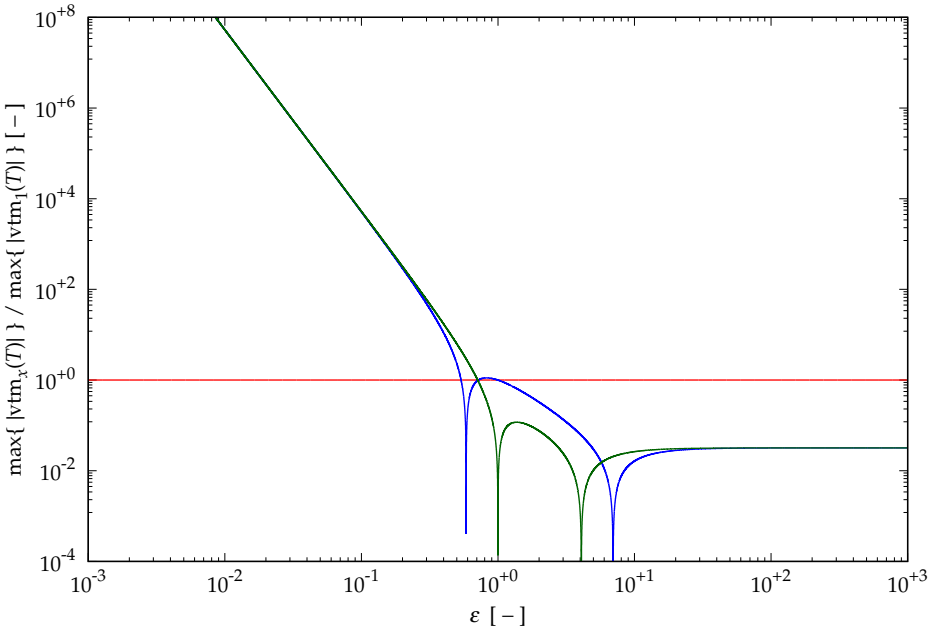

Figure 6.4: Comparison of absolute amplitudes of respective terms in variance to mean — the red, the blue, and the green lines stand for the 1st, the 2nd, and the 3rd terms, respectively.

6.5 Conclusions

A novel time-domain reactor noise technique that analyses the variance-to-mean function of integral values of continuous neutron detector current signals of ionization chambers such as the fission chamber was derived. This technique and the one described in the previous Stage, which uses the auto-covariance function of current signals, were elaborated as an alternative to pulse counting methods, to avoid the count-loss effect due to the dead time of pulse couting neutron detector systems. With regard to these two techniques, the experimental conditions under which they successfully work were discussed to apply them to subcriticality measurement through determination of the prompt neutron decay constant.

It was concluded that the prompt neutron decay constant could be determined by using simplified formulae of these two techniques when the time constant of neutron detector systems is much larger than the prompt neutron decay constant (the detector pulse width is much smaller than the lifetime of the subcritical prompt chain). With the currently used fission chambers and corresponding electronics, at least in thermal systems close to critical, this condition is likely to be fulfilled. Measurements, as well as numerical simulations (with Monte-Carlo methods) could bring further light into the question, not the least because measurement errors and back- ground noise cannot be modelled in the analytical investigations. Such experimental and simulation work is underway, and the results will be reported in the next Stage of the project.

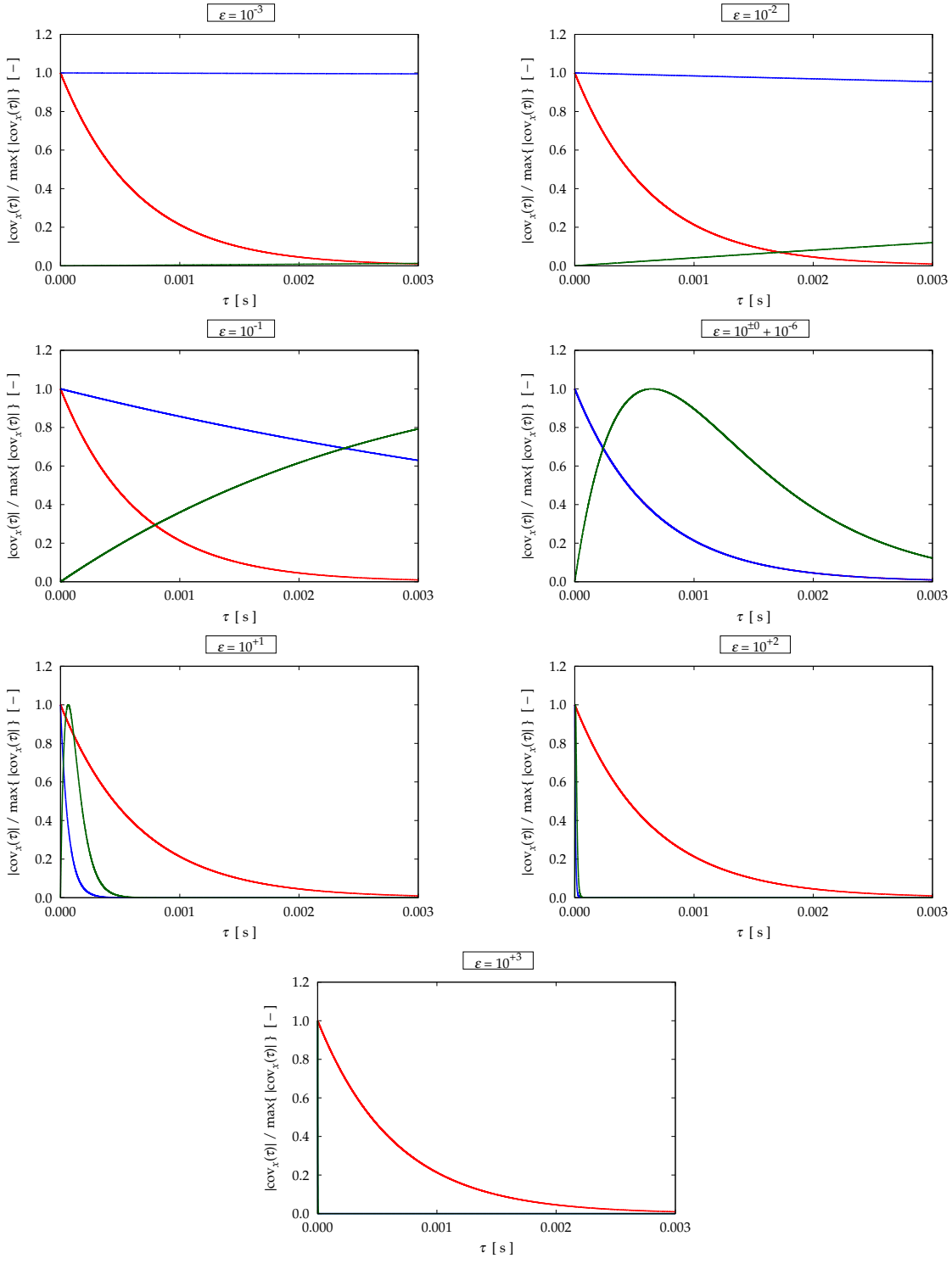

Figure 6.1: Comparisons of time dependences of respective terms in $\mathrm{cov}\,(\tau)$ — the red, the blue, and the green lines stand for the 1st, the 2nd, and the 3rd terms, respectively.

7. PROPOSAL FOR 2019

1. Further investigation of possible baffle jetting in R3 with noise analysis of in-core and ex-core detector signals.
2. Further nalysis of vibrations of thimble tubes with axially dependent in-core measurements in various radial positions.
3. Evaluation of new ex-core measurements for beam mode and tilting mode vibrations in R3 or R4.
4. Experimental work and simulations in support of the use of fission chambers in the current mode for reactor diagnostics, as an alternative of pulse counting methods.
5. Development of a new method to determine the axial velocity profile of the void in the core of a BWR by using four permanent in-core LPRMs and a TIP detector.

8. ACKNOWLEDGEMENT

This one-year contract was performed by funding from Ringhals Vattenfall AB, contract No. 677353-003. Contact person from Ringhals was Dr. Henrik Nylén.

REFERENCES

[1] P. Bernard, J. Cloue, C. Messainguiral, R. Baeyens, P. Mathot, J. Satinet, and C. Puyal, "PWR core monitoring by incore noise analysis," *Progress in Nuclear Energy*, vol. 9, pp. 541–556, 1982.

[2] D. J. Dailey and R. W. Albrecht, "In-core/ex-core neutron noise measurements to examine core internal vibrations in an operating PWR," *Progress in Nuclear Energy*, vol. 15, pp. 251–260, 1985.

[3] D. N. Fry, G. P. Horne, and C. W. Mayo, "Report of the first United States conference on utility experience with neutron noise analysis," *Progress in Nuclear Energy*, vol. 15, pp. 503–511, 1985.

[4] I. Pázsit, C. Demazière, C. Sunde, P. Bernitt, and A. Hernández-Solís, "*Final Report on the Research Project Ringhals Diagnostics and Monitoring, Stage 12*," CTH-NT-220/RR-14, Chalmers University of Technology, Göteborg, Sweden, August 2008.

[5] I. Pázsit, C. Montalvo Martín, V. Dykin, and T. Tambouratzis, "*Final Report on the Research Project Ringhals Diagnostics and Monitoring, Stage 13*," CTH-NT-230/RR-15, Chalmers University of Technology, Göteborg, Sweden, March 2010.

[6] F. Zylbersztejn, H. N. Tran, I. Pázsit, P. Filliatre, and C. Jammes, "Calculation of the neutron noise induced by periodic deformations of a large sodium-cooled fast reactor core," *Nucl. Sci. Engng*, vol. 177, pp. 203 – 218, 2014.

[7] J. Guitton and C. Puyal, "New trends in vibration and acoustic monitoring in nuclear components in EDF," *Progress in Nuclear Energy*, vol. 21, pp. 807–811, 1988.

[8] B. Michel and C. Puyal, "Operational and economical experience with vibration and loose parts monitoring systems on primary circuits of PWRs," *Progress in Nuclear Energy*, vol. 21, pp. 469–473, 1988.

[9] I. Pázsit (Ed.), "*Final Report on the Research Project Ringhals Diagnostics and Monitoring, Stage 1*," CTH-RF-122/RR-3, Chalmers University of Technology, Göteborg, Sweden, September 1996.

[10] I. Pázsit, J. Karlsson, and N. Garis, "*Final Report on the Research Project Ringhals Diagnostics and Monitoring, Stage 2*," CTH-RF-132/RR-4, Chalmers University of Technology, Göteborg, Sweden, October 1997.

[11] J. K.-H. Karlsson and I. Pázsit, "*Final Report on the Research Project Ring-hals Diagnostics and Monitoring, Stage 3: Analysis of core barrel vibrations in Ringhals 2, 3 and 4 for several fuel cycles*," CTH-RF-135/RR-5, Chalmers University of Technology, Göteborg, Sweden, October 1998.

[12] M. Pázsit and I. Pázsit, "*Final Report on the Analysis of Core Barrel Vibrations in Ringhals PWRs R2, R3 and R4 from Measurements Made in 2005*," Internal report, Chalmers University of Technology, Göteborg, Sweden, 2006.

[13] C. Sunde, C. Demazière, and I. Pázsit, "*Final Report on the Research Project Ringhals Diagnostics and Monitoring, Stage 11*," CTH-NT-206/RR-13, Chalmers University of Technology, Göteborg, Sweden, February 2007.

[14] I. Pázsit, C. Montalvo Martín, V. Dykin, and H. Nylén, "*Final Report on the Research Project Ringhals Diagnostics and Monitoring, Stage 14*," CTH-NT-253/RR-16, Chalmers University of Technology, Göteborg, Sweden, December 2011.

[15] V. Dykin, C. Montalvo Martín, H. Nylén, and I. Pázsit, "*Ringhals Diagnostics and Monitoring, Final Research Report 2012 - 2014*," CTH-NT-304/RR-19, Chalmers University of Technology, Göteborg, Sweden, December 2014.

[16] V. Dykin, C. Montalvo, N. Tran, H. Nylén, and I. Pázsit, "*Ringhals Diagnostics and Monitoring, Annual Research Report 2015*," CTH-NT-319/RR-20, Chalmers University of Technology, Göteborg, Sweden, December 2015.

[17] I. Pázsit, C. Montalvo, N. Tran, H. Nylén, and O. Olvera Guerrero, "*Ringhals Diagnostics and Monitoring, Annual Research Report 2016-17*," CTH-NT-333/RR-21, Chalmers University of Technology, Göteborg, Sweden, December 2017.

[18] M. Nilsson, "*Brusmätning för att söka lågfrekventa störningar i R3, Annual Research Report 2015*," Ringhals internal report UH-rapport 2099930 / 2.0, Ringhals AB, Göteborg, Sweden, October 2010.

[19] B. Severinsson, "*"Brusmätningar för analys av härdhöljesvibrationer på Ringhals 3. Utförda mellan 2013-02-26 och 2013-07-05*," Ringhals internal report UH-rapport 2245846 / 2.0, Ringhals AB, Göteborg, Sweden, July 2013.

[20] B. Severinsson, "*Brusmätning för analys av Härdhöljesvibrationer på utförda under 2013*," Ringhals internal report UH-rapport 2233461 / 2.0, Ringhals AB, Göteborg, Sweden, July 2013.

[21] J. W. M. Stacey, *Space-time Nuclear Reactor Kinetics*. New York: Academic Press, Inc., 1969.

[22] R. A. Rydin, A. Burke, W. E. Moore, and K. W. Seemann, "Noise and transient kinetics experiments and calculations for loosely coupled cores," *Nuclear Science and Engineering*, vol. **46**, pp. 179–196, 1971.

[23] D. D. Ebert, J. Clement, and J. W. M. Stacey, "Investigation of the space- and energy-dependent coherence function in zero-power coupled-core reactors," *Nuclear Science and Engineering*, vol. 55, pp. 368 – 379, 1974.

[24] D. D. Ebert, J. D. Clement, and J. W. M. Stacey, "Interpretation of coherence function measurements in zero-power coupled-core reactors," *Nuclear Science and Engineering*, vol. 55, pp. 380 – 386, 1974.

[25] W. D. Beckner and R. A. Rydin, "Higher-order relationship between static power tilts and eigenvalue separation in nuclear-reactors," *Nuclear Science and Engineering*, vol. **56**, pp. 131–141, 1975.

[26] S. B. Brumbach, R. W. Goin, and S. G. Carpenter, "Spatial kinetics studies in liquid-metal fast breeder reactor critical assemblies," *Nuclear Science and Engineering*, vol. 98, pp. 103 – 117, 1988.

[27] T. Sanda, "Interpretation of noise coherence function measurements in liquid-metal fast breeder reactor critical assemblies," *Nuclear Science and Engineering*, vol. 104, pp. 135–144, 1990.

[28] K. Hashimoto, T. Ohsawa, R. Miki, and T. Shibata, "A practical formula for inferring eigenvalue separation from flux tilt measurements in nuclear-reactors," *Annals of Nuclear Energy*, vol. 18, no. 3, pp. 131–140, 1991.

[29] K. Hashimoto, T. Ohsawa, R. Miki, and T. Shibata, "Derivation of consistent reactivity worth and eigenvalue separation from space-dependent rod worths on the basis of modal approach," *Annals of Nuclear Energy*, vol. 18, no. 6, pp. 317–325, 1991.

[30] K. Hashimoto, *Decoupling-phenomena, analyses of large nuclear reactor cores by the method of spatial higher harmonics (in Japanese)*. PhD thesis, Graduate School of Nuclear Engineering, Nagoya University, 1995.

[31] K. Nishina and M. Tokashiki, "Verification of more general correspondence between eigenvalue separation and coupling coefficient," *Progress in Nuclear Energy*, vol. **30**, pp. 277–286, 1996.

[32] M. Andoh, T. Misawa, K. Nishina, and S. Shiroya, "Measurement of flux tilt and eigenvalue separation in axially decoupled core," *Journal of Nuclear Science and Technology*, vol. **34**, pp. 445–453, 1997.

[33] Y. Kato, T. Yamamoto, T. Kitada, T. Takeda, K. Hashimoto, S. Shiroya, H. Unesaki, and O. Aizawa, "Analysis of first-harmonic eigenvalue separation experiments on kuca coupled-core," *Journal of Nuclear Science and Technology*, vol. 35, no. 3, pp. 216–225, 1998.

[34] K. Ishitani, Y. Yamane, A. Uritani, T. Iguchi, and S. Shiroya, "Measurement of eigenvalue separation by using position sensitive proportional counter," *Annals of Nuclear Energy*, vol. 25, no. 10, pp. 721–732, 1998.

[35] K. Kobayashi, "A relation of the coupling coefficient to the eigenvalue separation in the coupled reactors theory," *Annals of Nuclear Energy*, vol. **25**, pp. 189–201, 1998.

[36] C. H. Pyeon, S. Misawa, S. Shiroya, and Y. Yamane, "Relationship between flux tilt in two-energy-group and eigenvalue separation," *Annals of Nuclear Energy*, vol. **28**, pp. 1625–1641, 2001.

[37] H. Taninaka, K. Hashimoto, C. H. Pyeon, T. Sano, T. Misawa, and T. Ohsawa, "Determination of lambda-mode eigenvalue separation of a thermal accelerator-driven system from pulsed neutron experiment," *Journal of Nuclear Science and Technology*, vol. 47, no. 4, pp. 376–383, 2010.

[38] I. Pázsit and C. Demazière, *Handbook of Nuclear Engineering: Noise Techniques in Nuclear Systems*, vol. **2**. Springer, 2010.

[39] K. Hashimoto, "Linear modal analysis of out-of-phase instability in boiling water reactor cores," *Annals of Nuclear Energy*, vol. 20, pp. 789–797, 1993.

[40] K. Hashimoto, A. Hotta, and T. Takeda, "Neutronic model for modal multichannel analysis of out-of-phase instability in boiling water reactor core," *Annals of Nuclear Energy*, vol. 24, pp. 99–111, 1997.

[41] A. Hotta, H. Ninokata, H. Takeuchi, and Y. Suzawa, "Regional instability evaluation of Ringhals unit 1 based on extended frequency domain model," *Nucl. Engng Design*, vol. 200, pp. 201–220, 2000.

[42] H. Ikeda, T. Ama, K. Hashimoto, and T. Takeda, "Nonlinear behavior under regional neutron flux oscillations in bwr cores," *Journal of Nuclear Science and Technology*, vol. 38, pp. 312–323, 2001.

[43] H. F. McFarlane, S. G. Carpenter, P. J. Collins, D. N. Olsen, and S. B. Brumbach, "Experimental studies of radially heterogeneous liquid-metal fast breeder reactor critical assemblies at the zero-power plutonium reactor," *Nucl. Sci. Engng*, vol. **87**, pp. 204–232, 1984.

[44] E. Gialdi, S. Grifoni, C. Parmeggiani, and C. Tricoli, "Core stability in operating BWR: operational experience," *Prog. Nucl. Energy*, vol. **15**, pp. 447–459, 1985.

[45] T. H. J. J. van der Hagen, I. Pázsit, O. Thomson, and B. Melkersson, "Methods for the determination of the in-phase and out-of-phase stability characteristics of a boiling water reactor," *Nuclear Technology*, vol. **107**, pp. 193–214, 1994.

[46] J. K. H. Karlsson and I. Pázsit, "Localisation of a channel instability in the Forsmark-1 boiling water reactor," *Annals of Nuclear Energy*, vol. **26**, no. 13, pp. 1183–1204, 1999.

[47] I. Pázsit, "2-group theory of noise in reflected reactors with application to vibrating absorbers," *Annals of Nuclear Energy*, vol. **5**, pp. 185–196, 1978.

[48] Y. Kitamura, I. Pázsit, and T. Misawa, "Determination of neutron decay constant by time-domain fluctuation analyses of neutron detector current signals," *Annals of Nuclear Energy*, vol. 120, pp. 691 – 706, 2018.

[49] Y. Kitamura and T. Misawa, "Delayed neutron effect in time-domain fluctuation analyses of neutron detector current signals," *Annals of Nuclear Energy*, vol. 123, pp. 119–134, 2019.

[50] L. Pál and I. Pázsit, "Campbelling-type theory of fission chamber signals generated by neutron chains in a multiplying medium," *Nuclear Instruments and Methods in Physics Research Section A: Accelerators, Spectrometers, Detectors and Associated Equipment*, vol. **794**, no. 1, pp. 90–101, 2015.

[51] F. de Hoffmann, *The Science and Engineering of Nuclear Power*, vol. 2, ch. 9, Statistical aspects of pile theory. Cambridge: Addison Wesley, 1949.

[52] R. P. Feynman, F. De Hoffmann, and R. Serber, "Dispersion of the neutron emission in u-235 fission," *Journal of Nuclear Energy (1954)*, vol. 3, no. 1, pp. 64–69, 1956.

[53] J. Orndoff, "Prompt neutron periods of metal critical assemblies," *Nucl. Sci. Engng*, vol. 2, pp. 450 – 460, 1957.

[54] A. Papoulis, *Probability, Random Variables and Stochastic Processes.* New York: McGraw-Hill, Inc, third ed., 1991.

[55] I. Pázsit, "Duality in transport theory," *Annals of Nuclear Energy*, vol. 14, no. 1, pp. 25–41, 1987.

[56] I. Pázsit and R. Chakarova, "Variance and correlations in sputtering and defect distributions," *Transp. Th. Stat. Phys.*, vol. 26, pp. 1 – 25, 1997.

CHALMERS UNIVERSITY OF TECHNOLOGY
SE 412 96 Gothenburg, Sweden
Phone: + 46 - (0)31 772 10 00
Web: www.chalmers.se